Technische Universität München

Fakultät für Chemie

Max-Planck-Institut für Biochemie

Abteilung für Molekulare Strukturbiologie

“Presynaptic Tethers and Connectors: Molecular Composition and Functional Role”

Christos Papantoniou

Vollständiger Abdruck der von der Fakultät für Chemie der Technischen Universität München zur Erlangung des akademischen Grades eines Doktors der Naturwissenschaften genehmigten Dissertation.

Vorsitzender:	Prof. Dr. Bernd Reif
Prüfer der Dissertation:	1. Hon.-Prof. Dr. Wolfgang Baumeister
	2. Prof. Dr. Johannes Buchner

Die Dissertation wurde am 24.02.2021 bei der Technischen Universität München eingereicht und durch die Fakultät für Chemie am 05.05.2021 angenommen.

Table of contents

Summary

Neuronal synapses are intercellular junctions formed between neurons. Neuronal communication is mediated by the neurotransmitters, packed in Synaptic Vesicles (SVs) at the presynaptic terminal. They are released from the presynaptic and bind receptors on the postsynaptic neuron. The fusion of the SVs with the presynaptic membrane, which causes neurotransmitter release, is both temporally and spatially controlled. The proteins that mediate the SV fusion are located close to the presynaptic membrane at an area called the Active Zone (AZ). The organization of these proteins has intrigued researchers for many years. The majority of studies that have been conducted use a biochemical approach, in order to find the function of these proteins. Other studies isolated and purified presynaptic proteins, in order to analyze their structure *in vitro*. Observing these structures *in situ* has mainly been done by using conventional Electron Microscopy (EM) techniques, which require sample dehydration, embedding in raisin and heavy metal staining, thus, creating structural artifacts and making the study of the proteins more challenging. Previous use of cryo-Electron Tomography (cryo-ET) in vitrified, fully hydrated synapses, which allows the study of their proteins in their natural environment, without structural artifacts, showed that there are filaments that connect the SVs with each other (connectors) and with the AZ (tethers).

In this project, we studied the role of the AZ proteins RIM, Munc13 and SNAP25 in the SV distribution and tether organization. We established a protocol for synaptosomal isolation from dissociated neuronal cultures and from organotypic hippocampal slice cultures and isolated synaptosomes where our proteins of interest were genetically ablated. Genetically manipulated synaptosomes, *wild type* controls and pharmacologically treated synaptosomes were imaged by cryo-ET. Subsequently, we used hierarchical segmentation to detect membrane-bound complexes and performed comparative quantitative analysis of connectors, tethers and SVs. We showed that RIM is required for bringing the SVs to the region proximal to the AZ (closer than 45nm to the AZ membrane), Munc13 is necessary for bringing SVs closer than 10nm and SNAP25

brings them closer than 5nm from the AZ. Munc13 activation by PDBu increases the number of SVs closer than 5nm. Contrary to previous studies of dehydrated samples, we did not observe “docked” SVs (those that showed a direct contact between SV and AZ membrane). Concerning tethering organization, we found that Munc13 is important for the formation of tethers shorter than 10nm and that it affects the readily releasable pool of the SVs, because it affects the number of tethers bound to SVs. Although SNAP25 does not alter the number of tethers in total, it affects their number per SV. We suggested a model where Munc13 acts downstream of RIM and SNAP25 acts downstream of Munc13, supporting such hypotheses from previous studies. Finally, as an initial phase of a longer future project, we attempted to directly detect AMPA receptors (AMPArs) in cryo-tomograms of synapses, by using a monoclonal antibody that specifically binds to these receptors. We visualized parts of the antibody in one of the two resulting classes, showing that this is a promising technique for direct detection of AMPArs.

Zusammenfassung

Neuronale Synapsen bilden interzelluläre Verbindungen zwischen Neuronen. Die Kommunikation der Nervenzellen wird durch Neurotransmitter ermöglicht, die in synaptischen Bläschen am synaptischen Endköpfchen konzentriert sind. Diese werden von präsynaptischen Nervenzellen ausgeschüttet, um an die Rezeptoren der postsynaptischen Nervenzelle zu binden. Die Verschmelzung der synaptischen Bläschen zur Transmitterfreisetzung ist sowohl zeitlich als auch räumlich kontrolliert. Die Proteine, die die Membranfusion der Vesikel ermöglichen, befinden sich nahe der präsynaptischen Membran in der aktiven Zone (AZ). Die Organisation dieser Proteine beschäftigt Forscher seit vielen Jahren. Die Mehrheit der bisherigen Studien nutze biochemische Ansätze, um die Funktion dieser Proteine herauszufinden. Zusätzlich gab es Studien in denen diese Proteine isoliert und aufgereinigt wurden, um ihre Struktur in vitro zu analysieren. Für die in situ-Analyse dieser Proteine wurde bisher hauptsächlich die konventionelle Elektronenmikroskopie verwendet, welche Probendehydratation, Harzeinbettung und Schwermetallfärbung benötigt und folglich durch strukturelle Artefakte Herausforderungen birgt. In der Vergangenheit konnte mit Hilfe der Kryoelektronentomografie von vitrifizierten Synapsen die Analyse synaptischer Proteine in ihrer physiologischen Umgebung ermöglicht werden und Filamente, die synaptische Vesikel miteinander (connectors) und mit der aktiven Zone (tether) verbinden ohne strukturell Artefake gezeigt werden.

Im Rahmen dieses Projekts untersuchten wir den Einfluss der AZ-Proteine RIM, Munc13 und SNAP25 auf die Verteilung der Vesikel und die Organisation der Tether. Dafür entwickelten wir ein Protokoll für die Isolierung von Synaptosomen aus der Zellkultur von dissoziierten Neuronen und aus der Gewebekultur von Hippocampus-Schnitten, in welchen die Proteine von Interesse gentechnisch entfernt wurden. Diese gentechnisch manipulierten Synaptosomen, entsprechende Kontrollen und pharmakologisch behandelte Synaptosomen wurden mit Hilfe der Kryoelektronentomografie untersucht. In der Folge detektierten wir membrangebundene Komplexe durch hierarchische Segmentierung und führten eine vergleichende quantitative

Analyse der connector, tether und der synaptischen Vesikel durch. Wir haben gezeigt, das RIM benötigt wird um synaptische Vesikel in unmittelbare Nähe zur AZ zu bringen (näher als 45 nm zur Membran der AZ), Munc13 bringt synaptische Vesikel näher als 10 nm und SNAP25 näher als 5 nm an die AZ. Die Aktivierung von Munc13 durch PDBu erhöht die Anzahl der Vesikel im Abstand kleiner 5nm. Im Gegensatz zu vorherigen Studien an dehydrierten Proben, konnten wir keine „docked“ Vesikel beobachten (welche direkten Kontakt der AZ- und Vesikel-Membran zeigen. Bezüglich der Formation von tethern, fanden wir dass Munc13 die Bildung von tethern begünstigt, die kürzer als 10 nm sind und den „readily releasable pool“ beeinflusst, da es die Anzahl der tether pro Vesikel erhöht. Obwohl SNAP25 nicht die absolute Zahl der tether verändert, beeinflusst es ihre Anzahl pro Vesikel. Wir schlagen ein Modell vor in dem Munc13 in Abhängigkeit von RIM und SNAP25 in Abhängigkeit von Munc13 agiert, was die Hypothesen früherer Studien stützt. Schließlich initiierten wir ein zukünftiges Projekt, bei dem wir anstreben AMPA Rezeptoren direkt in Kryo-Tomogrammen zu identifizieren, indem wir einen monoklonalen Antikörper direkt an diesen Rezeptor binden. Wir visualisierten Teile dieses Antikörpers in eine der beiden Klassen und zeigen somit, dass dies eine vielversprechende Methode für die direkte Identifikation von AMPA Rezeptoren ist.

1. Introduction

1.1 Cryo-Electron Tomography on cellular samples

The attempt to understand biological phenomena has been, for many years, limited to the isolation of the molecules that make up the living cell. Despite the successful achievements in that field (atomic resolution structures of DNA, myoglobin etc.), which revealed the importance of molecular structural biology, studying individual models rarely attributes to discrete biological functions. The understanding of the spatial organization of the molecular assemblies and the biochemical pathways is of great importance. Although a plethora of information about the identity and functionality of these molecular players has been acquired and analyzed by means of genomics and mass spectrometry–based proteomics, structural methods need to be used, to confirm these findings (Lučić, Rigort, & Baumeister, 2013).

The development of x-ray crystallography and single-particle electron microscopy elucidated the structure of molecular assemblies that are held together by strong interactions that permit purification. However, there are often assemblies that cannot be purified for *in vitro* studies, or that only exist in transient states. Also, for some cases, it is important to study the structure of a molecular assembly in its native environment (*in situ*) and in relation to neighboring components (Lučić et al., 2013).

Cryo-Electron Tomography (cryo-ET) is the combination of Transmission Electron Microscopy (TEM) and Tomography with cryo techniques and enables the visualization of frozen hydrated biological samples, without the use of preparation methods that would affect the quality of the sample (e.g. heavy metal staining, dehydration, resin embedment etc.) (Brandt et al., 2010; Lučić et al., 2013; Koning et al., 2018). The hydration of the samples is achieved by vitrification (rapid freezing) which preserves the samples better than methods based on chemical fixation. The detailed ultrastructure of large cellular volumes can be revealed, allowing

nanometer resolution to be reached (Marsh, Mastronarde, Buttle, Howell, & Mcintosh, 2001). The main vitrification methods are plunge-freezing (Dubochet & McDowall, 1981) and high pressure freezing (Müller, Meister, & Moor, 1980).

There have been many advances in the field of cryo-ET throughout the years, both in the field of data collection and in the field of image processing. Automated tilt series acquisition allows the focusing and adjusting of errors to be performed at a location adjacent to the area of interest, minimizing the amount of dose on the sample (Dierksen, Typke, Hegerl, Koster, & Baumeister, 1992; A. J. Koster, Chen, Sedat, & Agard, 1992; Abraham J. Koster et al., 1997). The development of Volta Phase Plates (VPP) enhances the contrast and allows imaging closer to focus, thus improving the high-resolution information (Danev, Buijsse, Khoshouei, Plitzko, & Baumeister, 2014). The energy filter reduces the image noise by filtering out the inelastically scattered electrons (Krivanek, Friedman, Gubbens, & Kraus, 1995). Direct electron detectors (DDD) detect electrons without converting them to photons, providing better transfer properties, stronger signal and faster readout (Ruskin et al., 2013; McMullan et al., 2014). The fact that tomographic data of multiple tilt-series can be automatically recorded over several days and the constantly increasing amount of data storage availability provides the necessary conditions for acquiring more data in the same amount of time (reviews in Lučić et al., 2013 and Koning et al., 2018).

Concerning image processing, advances have been made in automated tomogram preprocessing and 3D reconstruction (review in Koning et al., 2018). The contrast-transfer-function (CTF) correction restores the high-resolution information that has been distorted by image defocusing (Fernández, Li, & Crowther, 2006). The subtomogram averaging and template matching methods allow the determination of macromolecular structures as well as their structural variety in native biological environments (review in Koning et al., 2018). Finally, tomogram segmentation (manual, or automated) allows surface representation of biologically-relevant structures, thus, helping the interpretation and 3D view of these volumes (reviews in Lučić et al., 2013 and Koning et al., 2018).

The development of cryo-ET and the advances in the field throughout the years, have paved the way for extraordinary research. A few notable examples are the visualization of actin

in the slime mold *Dictyostelium* (Medalia et al., 2002), the investigation of chromatin (Eltsov, MacLellan, Maeshima, Frangakis, & Dubochet, 2008), the location and study of the 26S proteasome inside the cell and nucleus (Asano et al., 2015; Albert et al., 2017) and the research into the molecular and cellular pathology of diseases (Bäuerlein et al., 2017) and pathogens (Wan et al., 2017).

1.2 Transmission Electron microscopy

Conceptually, an electron microscope (EM) is similar to a light microscope (LM). However, instead of using light for imaging, samples in EM are illuminated by an electron beam. Similar to focusing light by glass lenses in an optical microscope, electrons are focused by magnetic lenses. EM imaging resolution is limited by electron wavelength. While in diffraction-limited LM imaging the resolution that can be achieved is around 200nm, a theoretical EM resolution limit is in the picometer range. However, in practice this resolution cannot be reached because of other constraints (described below). There are several modalities of electron microscopy: in Scanning Electron Microscopy (SEM) the specimen is scanned by a focused electron beam. It is an excellent technique for determining the morphology of a specimen by detection of secondary and backscattered electrons, however, little structural information can be obtained by this modality. In Transmission Electron Microscopy (TEM), the electron beam provides a wide-field illumination and passes through the specimen. TEM is the technique used in this project and will be described in detail further on. Finally, in electron crystallography, the quantitative use of electron scattering information allows the determination of crystal structures. It is an important technique for the characterization of proteins which are periodically arranged in two-dimensional crystals (Zandbergen, 1997).

When an electron approaches the specimen in TEM it can either pass through it without any interaction (unscattered electron) or it can interact with its atoms (scattered electron). There are two major ways in which an electron can interact with the atoms of a specimen: elastic

scattering and inelastic scattering. In the first case, the electron interacts with the nucleus (protons) of the atom, eliciting a wide range of scattering angles, while the total kinetic energy remains the same. These electrons contribute to the high-resolution image formation (signal). On the other hand, interactions with phonons and electrons from the specimen that include electron excitation, ionization and interaction with plasmons results in a loss of kinetic energy and results in electrons that scatter at small scattering angles and have lower kinetic energy. Inelastically scattered electrons do not contribute to high resolution information, and often contribute to noise in images. The ratio between the elastically and inelastically scattered electrons that are detected is one of the important factors that determine the signal to noise ratio (SNR) (Reimer & Kohl, 2008).

The interaction of electrons with the atoms of an organic specimen results in breakage of chemical bonds and release of free radicals, which create sample damage (Glaeser & Taylor, 1978). This electron radiation damage ultimately leads to formation of hydrogen-gas filled cavities and appears as “bubbling” of the specimen during TEM imaging, locally destroying and deforming the sample (Karuppasamy, Karimi Nejadasl, Vulovic, Koster, & Ravelli, 2011; Meents, Gutmann, Wagner, & Schulze-Briese, 2010). By cooling down the sample at LN_2 temperatures, radiation damage can be substantially slowed down, but not entirely avoided. Therefore, the total electron dose that illuminates the specimen has to be low (Bammes, Jakana, Schmid, & Chiu, 2010).

To avoid a large number of interactions of the electrons with atoms constituting air that would occur at atmospheric pressure, the microscope is kept in high vacuum conditions (usually 10^{-10} bar) (Williams & Carter, 2009). Because liquid water is not compatible with the vacuum, aqueous biological samples cannot be maintained in EM. In conventional EM, this problem is solved by chemical fixation of the specimen, which is usually followed by dehydration and resin embedding of the specimen. In order to increase the contrast, specimens are often stained with heavy metals. However, all these methods are very likely to induce structural artifacts. The removal of water often causes aggregation and denaturation of the proteins. Also, in the case of heavy metal staining, the proteins themselves are not detected, but rather the molecules used for staining. Rapid freezing of hydrated samples results in the formation of amorphous ice, called

vitrification, which provides physical fixation. Vitrification immobilizes water molecules so fast that their reorganization to form crystals is prevented. Liquid water is transformed into a glass-like solid body. Crystal formation has to be avoided because its growth damages the specimen and distorts biological structures. It also induces imaging artifacts to the microscopic projections. Vitrification preserves the biological specimen to its native, fully-hydrated state, and also slows down the electron radiation damage (Dubochet et al., 1988).

1.3 Parts of a TEM

In this section, the different parts which a TEM is made of will be shortly described (figure 1).

1.3.1 Electron source

Located at the top of the microscope, the electron source emits and accelerates electrons into the column. In older microscope models, thermionic emission sources were used. However, the modern TEMs are equipped with Field Emission Guns (FEG). They consist of a pointed tungstein cathode tip and two or more anodes. High voltage, up to 300 kV, is applied to the crystal of the FEG and this produces a very strong electric field at its sharp tip (Kirkland, Chang, & Hutchison, 2007). The bright and steady beam that the FEGs produce, due to high temporal and spatial coherence, is necessary for high resolution imaging (Reimer & Kohl, 2008).

1.3.2 Illumination system

The electron beam emitted and accelerated by the FEG is focused by a set of electromagnetic condenser lenses. These lenses consist of coils that create a radially symmetric magnetic field. The strength of these lenses is set by the amount of current in their coils. In a Titan Krios TEM (ThermoFisher) there are three condenser lenses: C1 (also known as spot size) de-magnifies the gun crossover and controls the beam current. C2 sets the size of the illumination

area, which is used to limit the radiation damage of the specimen outside the field of view. Finally, C3 lens allows parallel illumination at different illumination sizes. The electron beam is restricted to the region close to the optical axis by apertures (each condenser lens has one) which are annular metal plates (figure 2).

1.3.3 Specimen stage

The EM grids that contain the specimen are loaded on the sample stage using different systems. Some microscopes use side entry holders to load the specimen manually on the sample stage. The recently developed computerized autoloading system has advantages compared to manual insertion: it is easier to use (specific training is required to be able to successfully insert the grid on the stage with manual insertion), it eliminates immediate interaction with the column of the microscope, and the grid is exposed less to ambient air, so there is smaller chance of sample contamination. The stage is a computerized goniometer which allows inserted grids to be precisely positioned in all three dimensions, and also to be tilted along an axis perpendicular to the beam (the stage's tilt axis). It is, also, cooled constantly to LN_2 temperature.

1.3.4 Imaging system

These lenses are responsible for creating the magnified image of the specimen. The objective lens system produces an image of moderate magnification, however, the quality of this image is crucial for the final resolution (Reimer & Kohl, 2008). The objective aperture is located in the back focal plane of the objective lenses. It improves the contrast of the image by screening out electrons scattered at high angles. The image formed by the objective lenses is magnified by the intermediate lenses and the projection lens to the final magnification. The final projection can be directly observed on a phosphor coated fluorescent screen, or is captured by the detector.

1.3.5 Energy filter

As mentioned before, inelastically scattered electrons lose kinetic energy and only contribute to noise in the final projection, resulting in poor contrast. To remove inelastically scattered electrons, a post column energy filter is placed directly before the detector. This filter consists of a magnetic prism that separates electrons according the their energy, a slit that selects the desired range of electron energies and a lens system to restore the final image on the detector (Krivanek et al., 1995). The energy filter operated in the zero-loss mode removes the inelastically scattered electrons that lost energy higher than a user set limit, increasing the SNR and enhancing the contrast (Rudo Grimm et al., 1997). The microscope used to record the data for this project is equipped with a Gatan energy filter operated in zero-loss mode (R. Grimm, Koster, Ziese, Typke, & Baumeister, 1996; Lučić, Förster, & Baumeister, 2005).

1.3.6 Detector

The final image needs to be recorded for further processing. Initially, the data was recorded on photographic films, but later on, the imaging plates replaced them because they had higher sensitivity and higher image quality. Although this offered a wide dynamic range and high quantum efficiency, it demanded complicated handling, digitalization and elaborate post processing (Mori, Oikawa, Katoh, Miyahara, & Harada, 1988). Attractive alternatives were the digital recorders, which made the images readily available for computational analysis without the time-consuming film handling. The first digital detectors used in microscopy were the scintillator-based charge coupled devices (CCD). The electrons are detected by the scintillator array, transformed into photons and transported to the CCD camera that further transforms the signal into an electronic signal for readout (Krivanek & Mooney, 1993). The fact that the signal is converted several times, introduces noise to the projection. Moreover, the photons are detected as a cloud of light by the sensor, resulting in a wide point spread function (PSF) and limiting the resolution (Booth & Mooney, 2013). Recently, direct electron detector devices (DDD) were developed. They detect electrons directly, without the need of extra conversions. The advantages of the DDD in respect to CCDs are: improved detection quantum efficiency (DQE) especially in high frequencies, decreased readout times, and the ability to record multiple frames per projection, which limits the effect of drift and sample movement (Ruskin et al., 2013; McMullan

et al., 2014). Furthermore, the counting mode of the DDD can localize electrons more precisely, suppressing the electronic noise (Booth & Mooney, 2013). Overall, the DDDs increased SNR and improved the contrast of the image. The microscope where the data of this project were acquired is equipped with a Gatan K2 detector.

1.3.7 Volta Phase Plate

In cryo-EM, contrast is mainly created by objective lens defocusing. In this case, image contrast arises from the local difference in intensity of two adjacent areas or pixels in an image. However, defocusing attenuates the contrast transfer at some high spatial frequencies resulting in loss of resolution, while the contrast transfer at low spatial frequencies continues to be poor.

Alternatively, contrast can be induced by Volta Phase Plate (VPP). It consists of a continuous carbon film, positioned in the back focal plane of the microscope in place of the objective aperture (on-plane condition). An initial "conditioning" exposure on the carbon film of a phase plate position develops a Volta potential which creates a phase shift to the unscattered beam relative to the scattered electrons. In order to prevent contamination and to enable the Volta potential, the VPP is heated to ~200^{o}C. Although the exact mechanism of the Volta potential formation is not yet completely understood, experimental data show that the phase shift of $\pi/2$ improves low frequencies, thus improving contrast and, also, allows imaging close to focus (-0.5µm), which enhances the transfer of high frequency information (Danev et al., 2014).

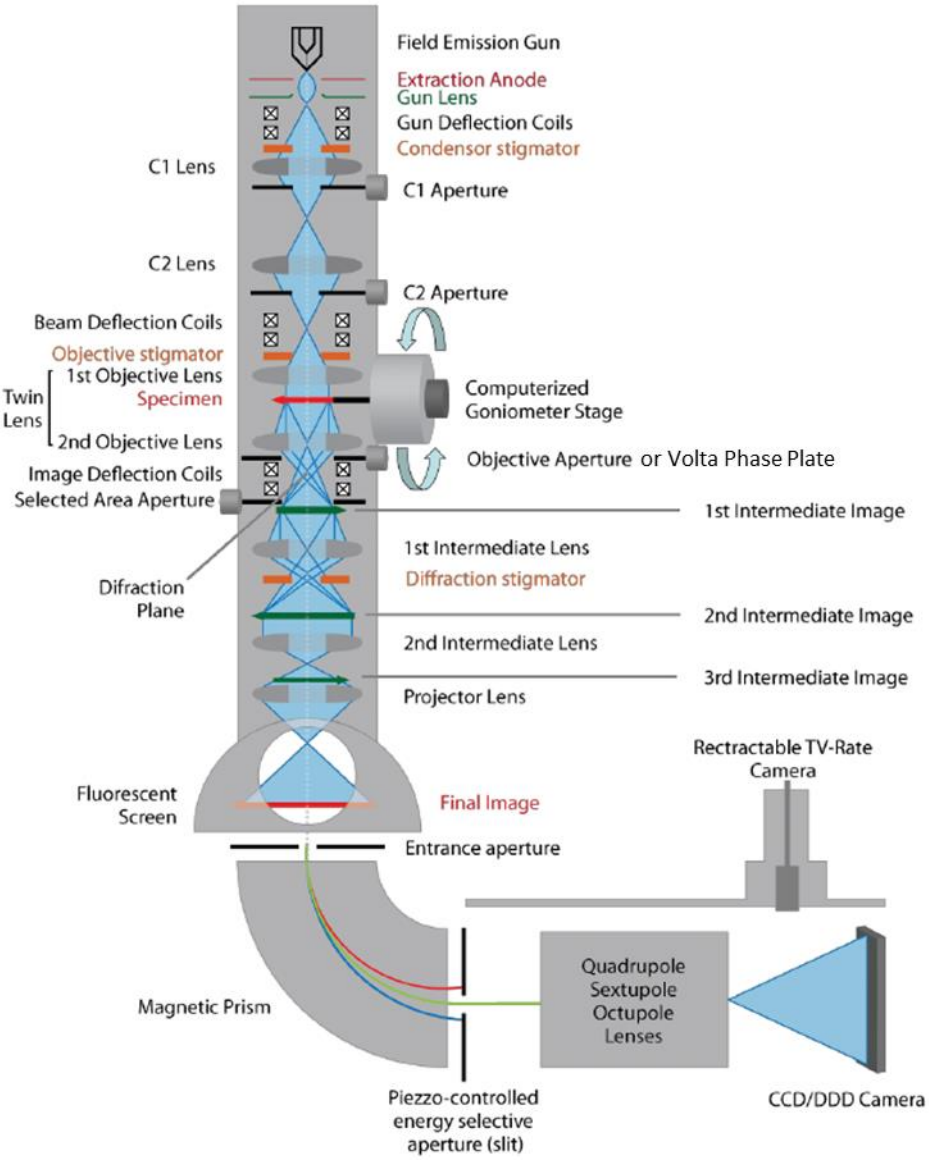

Figure 1: Schematic representation of the parts of a TEM. The beam path is depicted in blue. (Kochovski, 2014)

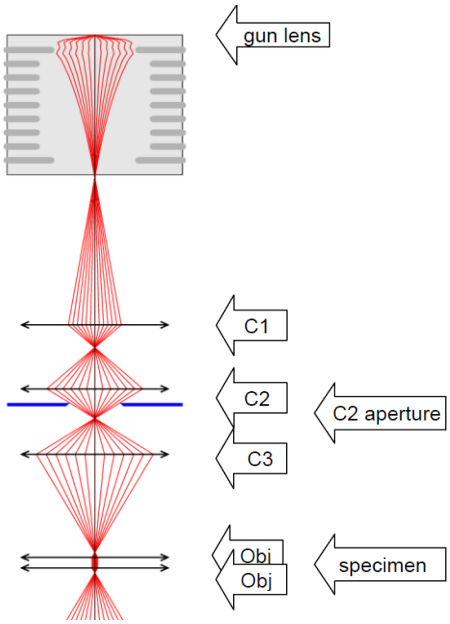

Figure 2: Position of the lenses on a 3 lens TEM like ThermoFisher's Titan Krios. The beam path is depicted in red. Taken from Titan – Condenser Manual (http://nchrem.nl/wp-content/uploads/2010/04/Titan-condenser-manual.pdf)

1.4 Image formation and resolution

The image contrast in TEM is comprised of amplitude and phase contrast.

As mentioned before, elastic scattering of electrons with the atoms of the specimen contributes to high resolution image information, while inelastic scattering results in image noise (SNR) (Reimer & Kohl, 2008). Amplitude (or absorption, or scattering) contrast is the difference of intensity at two neighboring regions. It arises because at electron-dense regions of the specimen, some electrons are scattered at high angles and are blocked by the objective aperture. Places of the image that correspond to high-scattering regions of the sample are dark, because the majority of the electrons interacting with this sample do not reach the detector. In heavy metal stained samples, for example, the stain has a high atomic number, which leads to high-

angle scattering upon the electron's interaction with it. Amplitude contrast in non-stained biological samples, like the ones acquired in this project, is achieved with the use of an energy filter, in zero-loss mode, right before the detector. This filters out the inelastically scattered electrons and increases the contrast (Yonekura, Braunfeld, Maki-Yonekura, & Agard, 2006).

Phase contrast has its origin in the phase-shift of the electrons' wave function, as they are elastically scattered in the specimen. It can be introduced when an image is recorded in defocus, where the superposition of electrons scattered from neighboring regions of the specimen creates an interference pattern. It can be mathematically described by contrast transfer function (CTF), which depends on the acceleration voltage, objective lens spherical aberration and the defocus value (Dubochet et al., 1988). In this project, the images were acquired in negative defocus (under-focus). While the defocus-induced phase contrast increases contrast and allows imaging of non-stained specimen, it also negatively affects features at higher resolution, thus reducing the resolution that can be achieved.

Phase contrast induced by the VPP is created by the superposition of the direct (unscattered) and scattered electron waves. This is made possible because the unscattered wave acquires a phase shift by interacting with higher potential localized on a region of the VPP where unscattered electrons pass. In this case, images can be recorded close to focus which reduces the defocus-induced alteration of higher frequencies and improves resolution

The capability of a microscope to separately visualize two points of an object defines its resolution (d). It is described by the Rayleigh criterion (Williams & Carter, 2009):

$$d = \frac{0.61 * \lambda}{\alpha}$$

with α being the angular aperture and λ the wavelength. It is clear that, by using this equation for the wavelength of a light microscope (~550nm), the resolution of diffraction-limited light microscopy cannot reach beyond 200nm (Williams & Carter, 2009). However, recently developed super-resolution light microscopy "breaks" the diffraction limit of conventional optical microscopy to achieve resolutions approaching tens of nanometers (Gustafsson, 2000; Klar & Hell, 1999; Patterson, Davidson, Manley, & Lippincott-Schwartz, 2010).

1. Introduction

As shown by De Broglie, the wavelengths of electrons are related to their energy. This can be described by:

$$\lambda = \frac{1{,}22}{E^{\frac{1}{2}}}$$

Here, the relativistic effects are ignored. Based on the particle-wave-duality, the particle momentum p of an electron can be related to its wavelength λ through the Planck's constant h:

$$\lambda = \frac{h}{p}$$

The momentum is conveyed to the electron by acceleration, inducing a kinetic energy eV:

$$eV = \frac{m_0 v^2}{2}$$

The momentum can be replaced by the electron mass m_0 times its velocity v:

$$p = m_0 v = (2m_0 eV)^{\frac{1}{2}}$$

As a result, the resolution of a TEM depends on the energy of the accelerated electrons and, thus, on the acceleration voltage of the microscope, as shown here:

$$\lambda = \frac{h}{(2m_0 eV)^{\frac{1}{2}}}$$

It is clear that, by increasing the acceleration voltage, the wavelength of an electron is decreased. Since modern TEMs are working with acceleration voltages of 100keV and above, the relativistic effects of the electrons should be taken into account. So, the equation that calculates

the wavelength of the electrons depending on the acceleration voltage of the microscope is as follows:

$$\lambda = \frac{h}{\left[2m_0 eV\left(1 + \frac{eV}{2m_0 c^2}\right)\right]^{\frac{1}{2}}}$$

The microscope used at this project, operates at 300kV. So, the wavelength of the electrons is 0.00197nm (Williams & Carter, 2009).

In practice, of course, this resolution cannot be reached because aberrations of the lens system reduce the achievable resolution. The most critical errors are: spherical aberration, astigmatism, coma and chromatic aberration.

The spherical aberration reduces the focal length of electrons that pass through the objective lens away from the optical axis. Refraction of electrons induced by a lens depends on the distance of electrons from the optical axis. It can be described by the spherical aberration coefficient Cs. Because electrons in a beam are not refracted homogeneously by the objective lens, the beam does not focus in one point, but in a disc of a specific radius r_{sa}. The minimal resolution is, then, limited by the spherical aberration coefficient:

$$r_{min} = 0.91 * (Cs\lambda^3)^{\frac{1}{4}}$$

Thus, the resolution limit is between 0.7 and 1.5Å (Reimer & Kohl, 2008).

The imperfect magnetic field of the lenses causes astigmatism. Because lenses cannot be produced in perfect cylindrical shape and they contain microstructural incoherencies, local changes to the magnetic field are induced. Contamination on apertures deflects the beam, further contributing to this phenomenon. Stigmator lenses, as well as the imaging system, to some extent correct this defect (Williams & Carter, 2009).

The electrons in the magnetic field of a lens are not moving straight, but rather spiral along the optical axis around a symmetry center. If the beam is not aligned with the axis of an electromagnetic lens, the formation of coma is observed and the rotation center is misaligned.

For this reason, a coma-free alignment prior to imaging, is a very important step for high resolution imaging (Reimer & Kohl, 2008; Williams & Carter, 2009).

The difference in scattering angles of electrons having different wavelengths by the objective lens causes chromatic aberration. This is because electrons with lower energy are scattered more strongly. Similar to spherical aberration, electrons are not focused in a point, but are projected into a disc with a specific diameter:

$$r_{chr} = Cc\left(\frac{\Delta E}{E_0}\right)\beta$$

where Cc is the chromatin aberration coefficient, E_0 is the initial energy of the electron and β is the semi-angle of collection of the lens (Williams & Carter, 2009).

1.5 Cryo-Electron Tomography

1.5.1 Sample preparation

As mentioned previously, the biological sample needs to be physically or chemically fixed before it is inserted to the microscope, because otherwise the water would evaporate due to the high vacuum. Vitrified samples are in the solid state and are thus protected from evaporation. Furthermore, vitrification differs from standard freezing in that it avoids the formation of ice crystals. This is achieved by rapidly freezing the sample (10^5 ^{o}C/sec in 20μm depth of sample) (Dubochet et al., 1988). Such fast freezing prevents reorganization of water molecules that is required for the formation of ice crystals. Water stays in its amorphous ice phase below -136^{o}C. Above that, it starts transitioning to crystalline ice. So, the vitrified samples need to be kept below this temperature. The main two vitrification methods are high pressure freezing, which is mostly used for thick samples (Müller et al., 1980) and the plunge freezing, mostly used for single cells

or protein solutions (Dubochet & McDowall, 1981). The technique used in this project is plunge freezing, and will be analyzed in more detail below.

Plunge freezing is the most widely used vitrification method for cryo-EM. The sample is usually placed on an EM grid with a pipette directly before vitrification, while cells are often grown on EM grids in a culture medium. The excess medium is removed by blotting to reduce the thickness of the sample. After blotting, the grid is rapidly immersed in the cryogen, with the help of a plunging device. It has been shown that a mixture of ethane (37%) and propane (63%) is an excellent cryogen. The effect of calefaction (creation of a layer of evaporating gas around the sample during freezing) does not occur, and thus, insulation around the sample is avoided. Also, it is liquid at -196^{o}C, which is the boiling point of LN_2. Thus, the ethane/propane gas mixture, can be easily liquefied when placed in a container surrounded by LN_2 Pure ethane can also be used as a cryogen, however the range of temperature values in which it remains liquid is much more narrow than the ethane/propane mix (Engelhardt, 2018).

1.5.2 Data acquisition

There are three main methods to obtain 3D images in the field of cryo-EM: Single Particle Analysis (SPA), cryo-Electron Tomography (cryo-ET) and electron crystallography, which can determine the atomic structure of 2D crystalline specimen. Both SPA and cryo-ET methods require 2D transmission EM images of thin biological samples as input and they rely on the computational reconstruction of these images.

SPA allows the 3D reconstruction of proteins or protein complexes at near atomic resolution. It requires the imaging of a large number of purified particles. The purified complexes are vitrified at such a concentration that allows the recording of multiple copies of the complex in different orientations. Particles are extracted from the projection images, where the complex is represented by the majority of its orientations, and are aligned and reconstructed in 3D iteratively, until a stable resolution has been acquired. A clear advantage of SPA over x-ray crystallography is the fact that native conformational states of a protein can be investigated. Moreover, proteins that cannot form crystals can be investigated with SPA (De Rosier & Klug, 1968; Taylor & Glaeser, 1976).

In cryo-ET, a typically more complex sample, such as cell organelles or cellular fractionations, or intact cells, is imaged in 3D (Baumeister, 2005). To obtain a 3D image (tomogram) of a sample with its full complexity at molecular resolution, a series of projections is being recorded at different orientations by tilting the computerized stage around its tilt axis. Limitations of the hardware allow a tilt range maximum at ±70°. In most cases, imaging is limited to ±60° or even a lower angular range, because the sample thickness in the direction of electron beam is increasing in high tilt angles (figure 3). The projections of each tilt are, then, computationally aligned and reconstructed to produce the final tomogram.

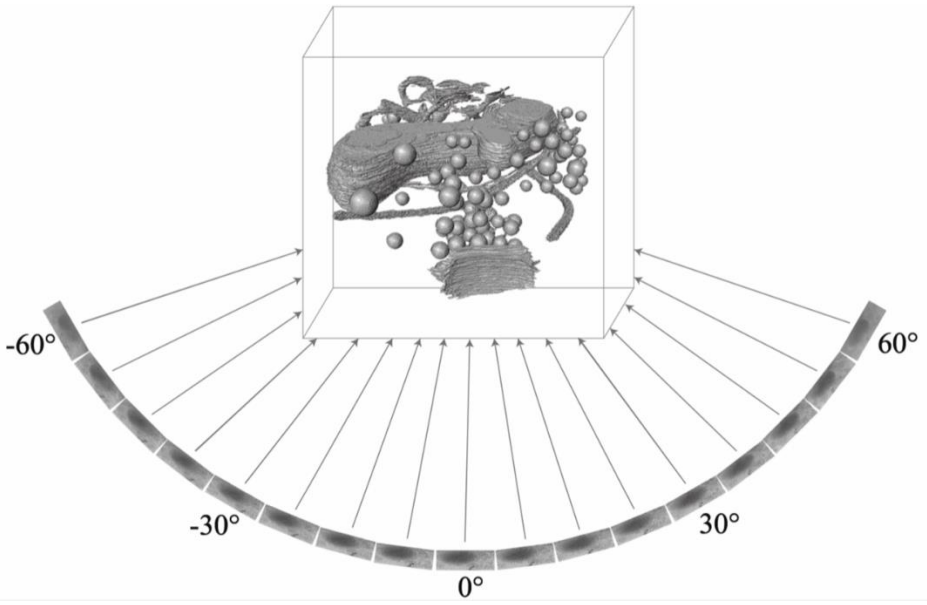

Figure 3: A projection series recorded at different orientations of the sample. An angular range of ±60° is used due to limitations of the hardware and sample thickness. (Laugks, 2018)

There are several angular increment schemes to record a tomogram: the Saxton scheme aims to compensate for the increasing thickness of the higher tilt angles by decreasing the tilt increments (Saxton, Baumeister, & Hahn, 1984). However, in the presence of noise, a constant angle increment between the different tilts appear to perform better. The unidirectional scheme starts from one end (-60°) and ends to the other (+60°), the bidirectional scheme records in two separate series (e.g. 0° - +60° and -2° - -60°) and the dose symmetrical scheme (also called Hagen

scheme) begins at 0^{o} tilt and alternates between increasingly positive and negative tilts (figure 4). The advantage of the dose symmetrical scheme is that all low tilt images, which contribute the most to the high frequency information, are recorded in the beginning, before the electron irradiation starts affecting the sample. High tilt images have lower SNR anyway, so the fact that their high-resolution information deteriorated because of the already received dose is not important. Moreover, a higher total electron dose can be applied, because accumulated radiation damage and sample deformation appear in higher tilts, which can be easily discarded during reconstruction and post-processing (Hagen, Wan, & Briggs, 2017).

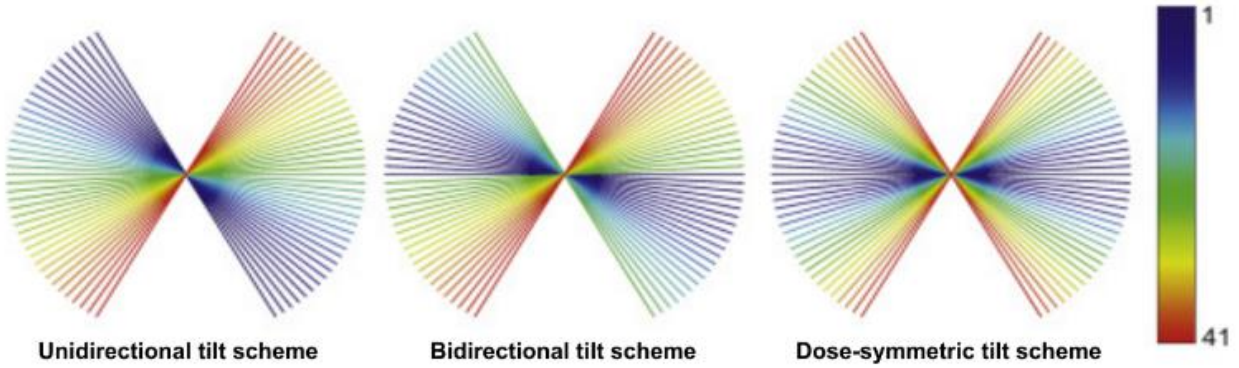

Figure 4: The 3 different angular schemes to record a tomogram. In each example the tilt series were recorded between ±60^{o} with an increment of 3 (41 projections in total). The higher the number of tilts, the higher the electron dose accumulated on each image. The dose-symmetric tilt scheme is preferred because the accumulated damage appears only in higher tilts. (Hagen et al., 2017)

As said above, there are limitations to the stage tilting, so a sample cannot be recorded outside the angle range of the stage. Each projection image is represented in the Fourier space as a slice perpendicular to the optical axis of the microscope. The lack of information due to the limited angle range is represented as a wedge-shaped region in the Fourier space, and thus, it has been called the missing wedge (figure 5) (Hoppe & Hegerl, 1980).

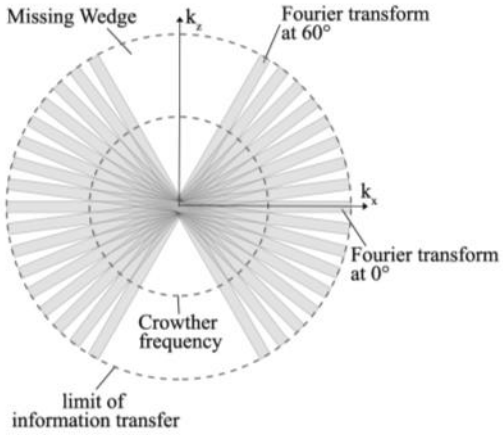

Figure 5: Representation of each projection as a thin slice in Fourier space. Because the acquisition is, usually, between ±60°, the lack information is shown as the missing wedge. (Laugks, 2018)

The maximum reachable isotropic resolution d of a tomogram is directly influenced by the chosen tilt increment $\Delta\alpha$, as described by the Crowther criterion (Crowther, DeRosier, & Klug, 1970):

$$d = D\Delta\alpha$$

with D being the diameter of the cylinder that would be created if the sample could fully rotate. Although this relationship does not take into account the tilt limitations, the noise, the missing wedge and the dose-dependent resolution impairment, it emphasizes that better resolution can be achieved with a smaller angle increment.

Because of the increased sample thickness at higher tilts, the beam needs to travel a larger distance through the sample. In order to keep the SNR constant, higher dose for projections at higher tilt angles is used. One way to apply this increase is by gradually increasing the exposure time in a fashion of 1/cosine of the tilt angle which also guarantees control over the total electron dose (Fernández-Busnadiego & Lucic, 2012).

Because of mechanical imperfections, each time the stage is tilted to a new angle, additional position shifts occur. If not corrected, these could result in the incomplete imaging of the biological region of interest and affect the quality of the projection. For this reason, the position of the beam and the focus are controlled and corrected after each tilt by tracking (x, y position) and auto-focusing (z position) respectively. Since the radiation damage at the area of recording has to be kept at a minimum level, these corrections are performed outside the field of view, but still, along the tilt axis of the stage (Abraham J. Koster et al., 1997).

Even during the short time that the sample is exposed to the electron beam, there can be stage drift and beam-induced movement of the specimen, causing a smearing of the projection image. For this reason, the dose is fractionated for each projection (dose fractionation). This means that each projection is divided into multiple shortly exposed frames that can be aligned afterwards to reduce the aforementioned effects and thus, to improve the resolution and sharpness of the projection (Bai, Fernandez, McMullan, & Scheres, 2013).

After the tomogram acquisition, the 2D projections (tilt series) are used to create the 3D tomogram. First, the tilt series need to be aligned, in order to correct for errors during the acquisition (imprecise tilting, imperfect tilt axis orientation etc.). The use of fiducial markers, such as high-contrast particles (usually gold), which are clearly visible in all the images of the tilt series, is the most straightforward way to align the image stack. After the alignment, the 3D reconstruction process begins, which transforms the aligned image stack into a 3D tomogram. The most commonly used procedure for 3D reconstruction is the weighted back-projection, which re-projects the images of the stack to the 3D space, while correcting for uneven radial distribution of information in the Fourier space (Fernández-Busnadiego & Lucic, 2012).

1.6 Neurotransmitter release at neuronal synapses

A neuronal synapse is an intercellular junction formed between a neuron (presynaptic) and another cell (postsynaptic), which, in our case, is also a neuron. This junction facilitates the

communication between the two cells by chemical neurotransmitters, initially packed in Synaptic Vesicles (SVs) at the presynaptic terminal. The release of the neurotransmitters is controlled both temporally and spatially. More specifically, when electrical signal in the form of an action potential reaches the presynaptic terminal, the Ca^{2+} voltage gated channels located there open, followed by Ca^{2+} influx to the cell. This may cause the fusion of the SVs that are close to the active zone (AZ) membrane that is a small part of the presynaptic membrane, directly opposed to the postsynaptic terminal. The neurotransmitters are released from SVs into the synaptic cleft – which is the area between the two cells – and bind to specific receptors at the outer membrane of the postsynaptic cells. This binding may open postsynaptic ion channels and activate molecular pathways at the postsynaptic cell, and thus, successfully transfers the signal from the presynaptic cell (figure 6) (Gray, 1963; Couteaux & Pécot-Dechavassine, 1970).

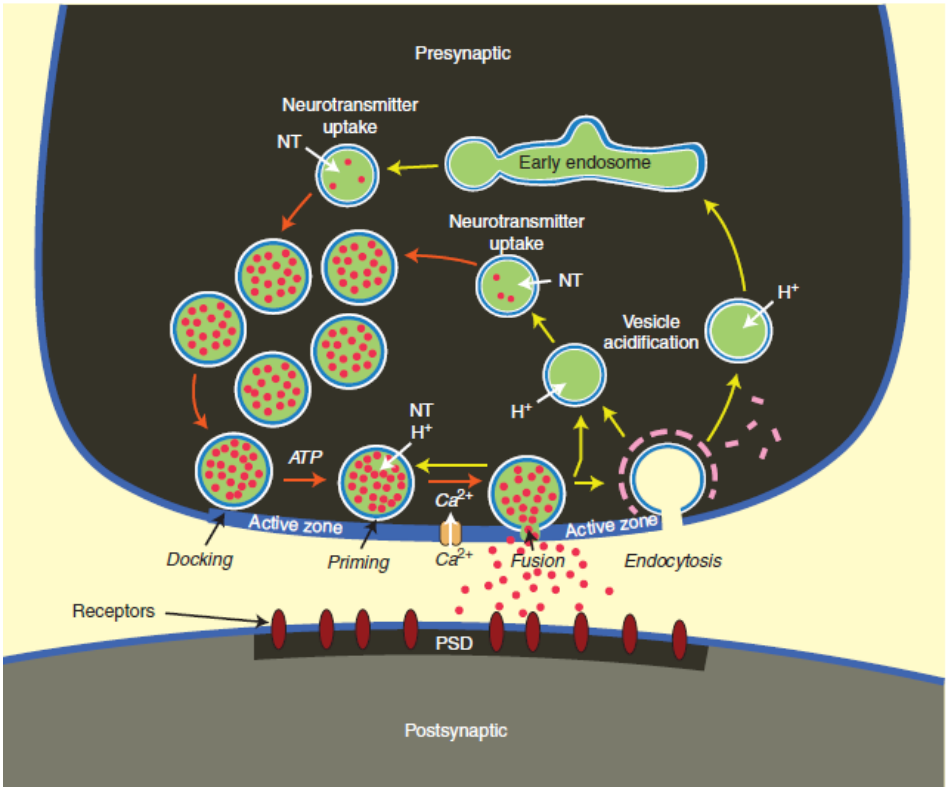

Figure 6: Schematic representation of a presynaptic nerve terminal. With the arrival of an action potential the Ca^{2+} voltage gated channels open and a local increase in intracellular Ca^{2+} occurs. This causes the fusion of the SVs (green) containing the neurotransmitters (red dots) that are close

to the AZ with the presynaptic membrane and the release of the neurotransmitters to the synaptic cleft. They bind, then, to receptors of the postsynaptic cell that are associated with the postsynaptic density (PSD). (T. C. Südhof & Rizo, 2011)

The AZ is a disc-shaped structure and, in the central synapses of the vertebrates, has a diameter of 0.2 – 0.5μm (Brodin & Shupliakov, 2006). Its main function is to organize the neurotransmitter release. Proteins present at the AZ play an important role to the SV release machinery, by preparing the SVs for exocytosis. They are responsible for recruiting voltage gated Ca^{2+} channels to the presynaptic membrane. With the help of transsynaptic cell-adhesion molecules, they take part to the precise location of pre- and postsynaptic specializations, exactly opposite to each other. They, finally, mediate the short- and long-term presynaptic plasticity that is observed in synapses (T. Südhof, 2012).

There has been a lot of research trying to explain the ultrastructure of the presynaptic terminal. Depending on the sample preparation technique and mode of analysis, there are diverging results concerning the association of SVs with the cytomatrix of the AZ (CAZ, a cytoskeletal matrix close to the presynaptic membrane) at the ultrastructural level. In the early 60s, pioneering EM described a symmetric grid structure of dense projections into the presynaptic cytoplasm in an organized pattern (Gray, 1963). Much later, chemically fixed, heavy-metal stained samples showed the docked SVs next to regularly arranged pyramidal densities (Phillips et al., 2001) while the analysis of chemically fixed synapses by Electron Tomography, revealed organization of the SVs in polyhedral cages (Zampighi et al., 2006). However, the former techniques were not optimal for structural analysis, because those samples were prepared using chemical fixation and dehydration, which may cause aggregation of cytoplasmic components or other artifacts. On the other hand, in preparations that were based on quick freezing and deep-etching, such organizations could not be observed. Instead, a dense network of filaments that could constrain SVs was shown for the first time (Hirokawa, Sobue, Kanda, Harada, & Yorifuji, 1989). Moreover, studies in which samples were prepared by High Pressure Freezing (HPF) and recorded using tomography also observed numerous filaments interconnecting SVs and tethering SVs to the AZ membrane (Siksou et al., 2007, 2009). With the development of cryo-ET and sample

vitrification, the existence of these filaments was verified and it was observed that they interlink the SVs to the AZ and to each other. Also, samples from cryo-ET did not show direct contact between the SVs and the AZ (docked SVs), in contrast with dehydrated samples (Fernández-Busnadiego et al., 2010).

According to emerging evidence, the core of the AZs is formed by five evolutionary conserved proteins: RIM, Munc13, RIM-BP, α-liprin, and ELKS. They are generally encoded by single genes in invertebrates, and by multiple ones in vertebrates. These core AZ proteins perform all the aforementioned functions of the AZs. What is interesting concerning these proteins, is the fact that they are not specific to AZ, or not even to neurons. This suggests that they perform other general functions (T. Südhof, 2012). Two large homologous proteins that form the presynaptic skeleton, called piccolo and bassoon, have been associated with the AZs in vertebrates (Fenster et al., 2000; Limbach et al., 2011; Tom Dieck et al., 1998; X. Wang et al., 1999). Additionally, synaptobrevin (or vesicle-associated membrane protein, VAMP) (Sutton, Fasshauer, Jahn, & Brunger, 1998; Weber et al., 1998) and the transmembrane proteins syntaxin-1, SNAP25 and Munc18 take part at SNARE's formation, and are also associated with the AZs in vertebrates (figure 7) (T. C. Südhof & Rothman, 2009). SNAP25, syntaxin-1 and synaptobrevin form the SNARE complex. This complex has been shown to control SV fusion and, thus, synaptic transmission. The rest of the AZ proteins regulate (either directly or indirectly) SNARE's formation (RIM, Munc13, Munc18), establish the AZ formation with recruitment of the SVs and Ca^{2+} channels (α-liprin, ELKS, RIM, Munc13, RIM-BP), or provide a presynaptic skeleton (piccolo, bassoon) (T. Südhof, 2012).

The order of events for the neurotransmitter release is outlined as follows: RIM activates Munc13 by reversing its homodimerization. Munc13, along with Munc18, promotes the proper assembly of the SNARE complex, which mediates the fusion between the SV and the presynaptic membrane upon the arrival of the action potential and Ca^{2+} influx. Proteins relevant for this study, RIM, Munc13 and SNAP25, as well as the formation and disassembly of the SNARE complex, are described in more detail below.

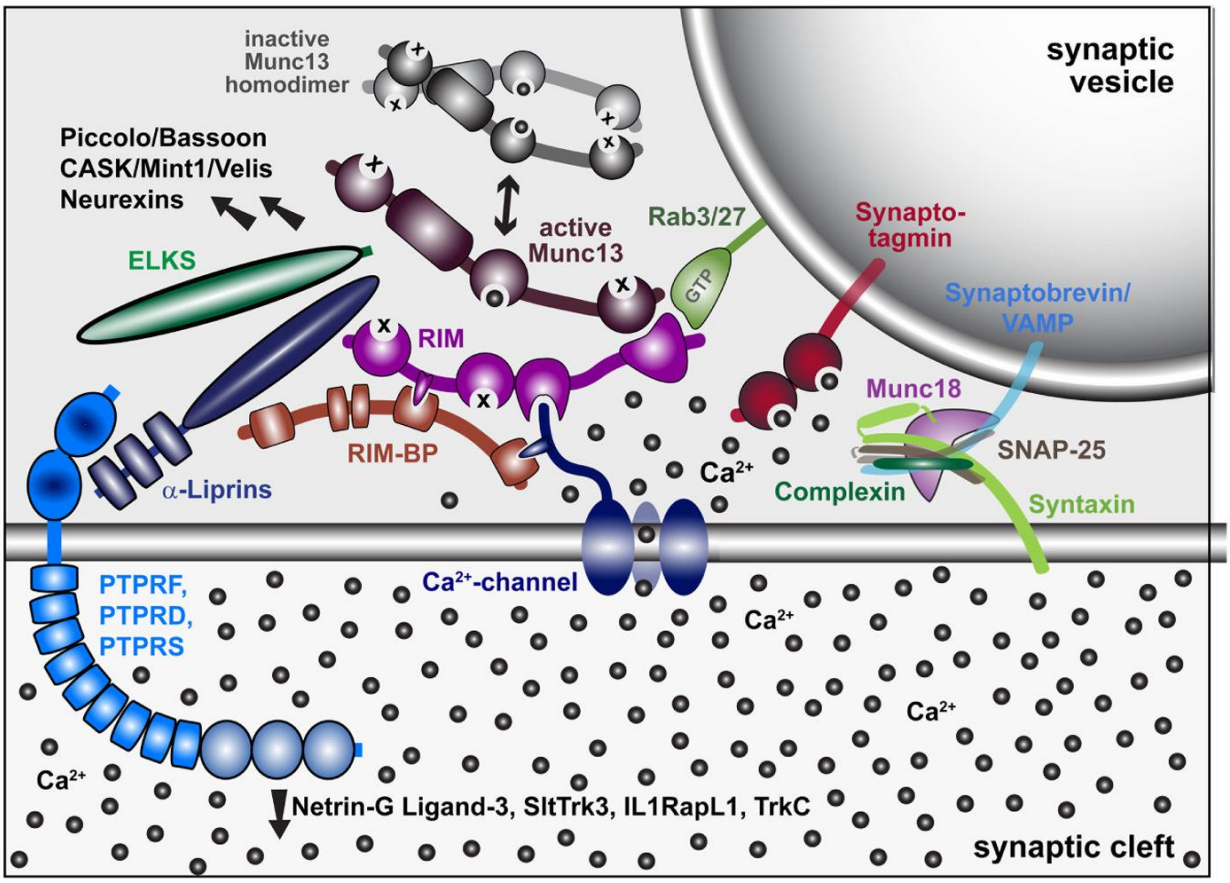

Figure 7: Schematic depiction of the proteins of the AZ and their relation to the SV fusion machinery and Ca^{2+} channels. Ca^{2+} molecules (black balls) interact with some of these proteins (whenever there is no interaction, an X is shown). (T. Südhof, 2012)

1.7 RIM

Rab3-interacting molecule (RIM), is a protein family first identified by Wang et al. (Y. Wang, Okamoto, Schmitz, Hofmann, & Südhof, 1997). It consists of five domains: an N-terminal domain (α helices surrounding a zinc finger), a central PDZ domain, two C-terminal C2 domains that differ from classical C2 domains in that they don't bind Ca^{2+}, and a conserved proline-rich sequence between the C2 domains (Y. Wang & Südhof, 2003). In vertebrates, four RIM genes are

expressed (RIM1, RIM2, RIM3, RIM4), which produce in total seven protein isoforms (RIM1α, RIM1β, RIM2α, RIM2β, RIM2γ, RIM3γ, RIM4γ) (figure 8). From these isoforms, only RIM1α and RIM2α include all the aforementioned domains. RIM1β and RIM2β lack a part of and the entire N-terminal domain respectively, while RIM2γ, RIM3γ and RIM4γ only contain the C2B domain (Kaeser et al., 2008; Wang, Sugita, & Südhof, 2000; Wang & Südhof, 2003; Südhof, 2012).

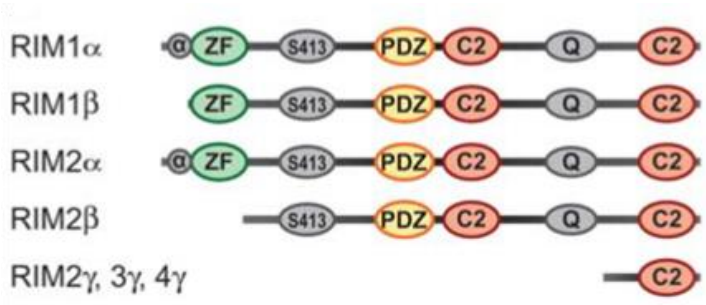

Figure 8: RIM protein family. Domain composition of the RIM isoforms generated from the four RIM genes. (Mittelstaedt, Alvaréz-Baron, & Schoch, 2010)

RIM has been shown to play a central role in AZ organization: it is essential for promoting SV priming by reversing Munc13 homodimerization (Deng, Kaeser, Xu, & Südhof, 2011), for recruiting Ca^{2+} channels to AZs (Kaeser et al., 2011), and for short-term plasticity of neurotransmitter release (Wang et al., 2002; Castillo, Schoch, Schmitz, Sudhof, & Malenka, 2002). RIM1α is the most abundant isoform in the brain and is important for all types of long-term presynaptic plasticity, which involve binding Rab3 (Pablo E. Castillo et al., 1997; Huang et al., 2005). Studies of RIM1α knockout (KO) mice that show severe deficits in synaptic transmission, memory and learning (Powell et al., 2004), a higher tendency for epileptic seizures (Pitsch et al., 2012) as well as schizophrenia-like behavior (Blundell, Kaeser, Südhof, & Powell, 2010) further argue that RIM1α plays a crucial role. Finally, hippocampal slices from RIM1α KO mice revealed a large reduction in release probability both in excitatory (Y. Wang et al., 2002) and inhibitory synapses (Kaeser et al., 2008).

The role of RIM1α in the organization of presynaptic cytomatrix has also been studied in our group, by comparing synaptosomes from mice that lacked the RIM1α isoform and WT mice.

Our group showed that RIM1α KO synapses had a 40% reduction in the concentration and the number of proximal SVs at the AZ. Moreover, two classes of synapses were described based on the organization of SVs in respect to the AZ: the aligned class, in which SVs showed the proximal concentration peak similar to the WT ones, and the altered one, in which the proximal concentration peak was absent (figure 9). The altered synapses showed drastic defects, severely reduced number of SVs close to the AZ and decreased number of tethers per AZ and per SV compared to the WT synapses. This shows that, although RIM1α is important for the formation of tethers, there are also RIM1α independent synapses. The aligned synapses had similar number of tethers as the WT, but they showed important differences in the connectivity and the distribution of SVs in the proximal zone. This argues that the tethering function of RIM1α is partially compensated in the aligned synapses, possibly by other RIM isoforms (Fernández-Busnadiego et al., 2013).

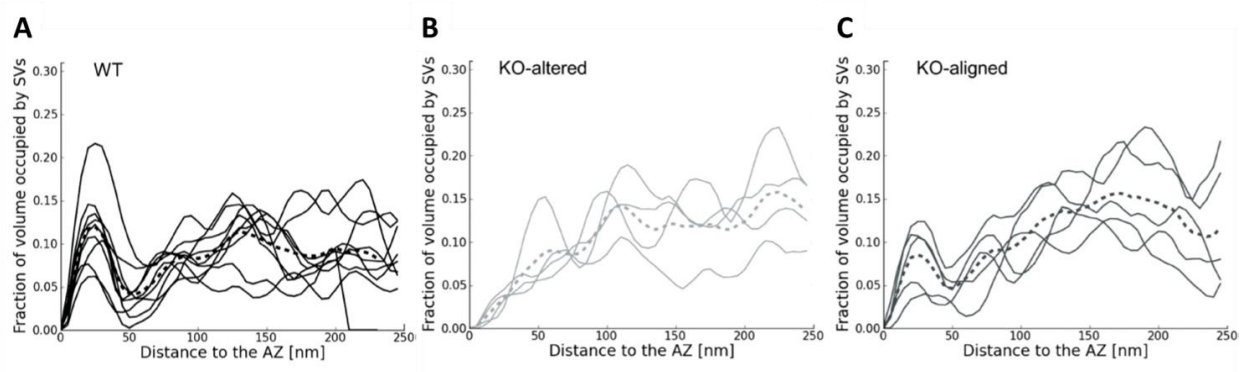

Figure 9: SV distribution of A: WT synapses, B: RIM1α KO altered synapses and C: RIM1α KO aligned synapses. The absence of a proximal concentration peak can be clearly seen at the KO-altered class. (Fernández-Busnadiego et al., 2013)

Taken together, the results of all the analyses to date, lead to the following conclusions: first of all, RIM1α plays a major role in priming and tethering of SVs to the active zone under physiological conditions. Second, regarding the molecular nature of the tethers, there is synapse heterogeneity in RIM1α KO synapses. The presence of two different classes leads to the hypothesis that other RIM isoforms have a similar function as RIM1α and also form tethers. The

synapse heterogeneity with regard to deficits in basal release properties (PPF) observed in RIM1α KO mice is a further indication for RIM1α independent tethers (P.E. Castillo et al., 2002).

The fact that, in spite of the absence of RIM1α, the formation of tethers still occurs, leads to the following question: What is the nature of the tethers in RIM1α-independent synapses? To address this question, synapses that lack all the isoforms of the RIM protein family need to be studied. Cryo-ET in vitrified, unstained synapses is the method required here. The reason is that studies with dehydrated, heavy metal stained samples, or samples made by High Pressure Freezing (HPF) and Freeze Substitution (FS) techniques are affected by artifacts induced by the aforementioned techniques. In previous studies based on HPF and FS, SVs were observed in direct contact to the plasma membrane , which is in contrast to our group's and other cryo data (Schrod et al., 2018; Tao et al., 2018; review in Zuber & Lučić, 2019).

1.8 Munc13

UNC-13 protein was originally identified in *C. elegans* and its mutation was shown to cause an 'uncoordinated' phenotype. However, its localization and function were not known at that time (Maruyama & Brenner, 1991). The mammalian homologs of UNC-13 were named Munc13s and were identified to be proteins of the AZ and to be crucial for SV priming (Brose, Hofmann, Hata, & Sudhof, 1995; Augustin, Rosenmund, Südhof, & Brose, 1999). Mammalian Munc13 protein family consists of five genes (Brose et al., 1995; Song, Ailenberg, & Silverman, 1998; Koch, Hofmann, & Brose, 2000). Munc13-1, Munc13-2 and Munc13-3 are genes that translate into large proteins, which are primarily expressed in the brain, while Munc13-4 and BAP3 produce smaller proteins that are mainly expressed outside the brain. More specifically, Munc13-2 has two promoters. One of them encodes the major form, which is ubiquitously expressed and is called ubMunc13-2. The other isoform is less abundant, is specific to the brain and is called bMunc13-2 (Brose et al., 1995; Song et al., 1998). All Munc13 isoforms have a C2B

domain, followed by a large domain (MUN domain) and a C-terminal Ca^{2+}- independent C2C domain (figure 10) (T. Südhof, 2012).

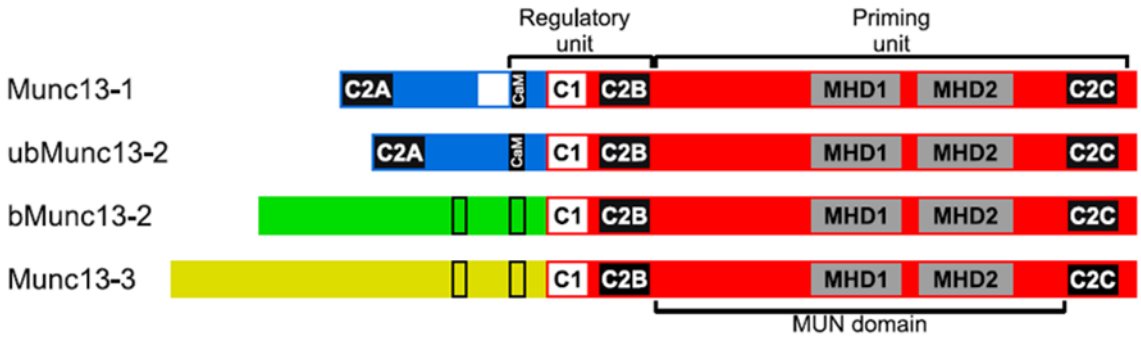

Figure 10: Munc13 protein family. Domain structure of Munc13 isoforms that are expressed in the brain. (Lipstein et al., 2012)

The two main functions of the Munc13 proteins, at the AZ, are the following. First, to ensure the correct assembly of the SNARE complex, so that all its components are assembled in a parallel configuration (see the "SNAP25 and SNARE complex" paragraph for more information about the parallel configuration). In this way, it primes the SNARE/SM protein fusion machinery for exocytosis, making the SV fusion possible. To achieve that, it binds to Munc18 to separate it from syntaxin-1 and, together, they promote the proper SNARE complex assembly (more information at the "SV fusion" paragraph). Second, to mediate short-term plasticity by the regulation of this priming activity. Munc13 forms homodimers of its N-terminal C2A domains, which inhibits its functions (Deng et al., 2011; Dulubova et al., 2005). When the C2A domain of Munc13 binds to the RIM zinc-finger, this homodimerization is disrupted and Munc13 is active (Deng et al., 2011). The priming of the SNARE/SM protein fusion machinery function is executed via the MUN domain of the Munc13 proteins (Basu et al., 2005; Stevens et al., 2005; Ma, Liging, Seven, Xu, & Rizo, 2013; Yang et al., 2015). The localization of Munc13 at the AZ membrane and the SV docking sites may be regulated by the binding of Ca^{2+} to Munc13's C2 domains (Liu et al., 2016), but also by interactions with proteins such as calmodulin (Junge et al., 2004) and Doc2 (Xue et al., 2018).

Munc13-deficient neurons lack a measurable Readily Releasable Pool (RRP), thus showing no SV fusion – neither spontaneous, nor evoked. This means that lack of all the Munc13 isoforms blocks the synaptic exocytosis in hippocampal neurons (Varoqueaux et al., 2002). Studies that used the techniques of HPF/FS for electron microscopy showed that lack of Munc13 (or UNC-13 in non-vertebrates) proteins in neurons has severe deficits in SV docking, both in *C. elegans* (Weimer et al., 2006) and in mice (Siksou et al., 2009). In a study of Nils Brose's lab, where HPF and FS on organotypic hippocampal slices from embryonic mice were studied, the following findings were shown: synapses lacking Munc13s had almost no docked SVs, although they had the tendency to accumulate close to the AZ membrane, so, the number of proximal SVs was unchanged compared to control synapses. They, also, observed a significant reduction in the number of SVs within 0–5 nm from the AZ membrane. Finally, the SV diameter and volume were increased in Munc13 DKO synapses (Imig et al., 2014). However, to our knowledge, no studies have, yet, examined the effects of Munc13 DKO on the organization of the tethers by using cryo-ET in vitrified, unstained synapses. This is important because (i) cryo-ET is the only method that allows reliable detection and quantitative characterization of tethers and (ii) vitrified, unstained samples can be studied without the artifacts created by HRF/FS, which show SVs in direct contact with the presynaptic membrane, in a not exo/endocytosis state.

1.9 SNAP25 and SNARE complex

Soluble N-ethylmaleimide sensitive factor Attachment protein Receptor (SNARE) proteins were first identified in 1980 (Novick, Field, & Schekman, 1980) and characterized in 1988 (Eakle, Bernstein, & Emr, 1988) in *S. cerevisiae*. SNARE proteins have been classified based on their location into two types: v-SNARE for SV membranes and t-SNARE for target plasma membrane bound. Vesicular, or v-SNAREs bind SV membrane and include synaptobrevin, while target, or t-SNAREs bind plasma membrane and include syntaxin-1 and SNAP25 (Synaptosomal Associated Protein 25 kDa) (Sutton et al., 1998; Weber et al., 1998). While the distinction of SNARE proteins

in v-SNARE and t-SNARE is still used often, it becomes ambiguous for many fusion reactions. Current findings suggest that SNAREs are characterized by conserved 60–70 amino acid stretches that are called SNARE motifs. Synaptobrevin and syntaxin-1 contain one SNARE motif each, which precedes a C-terminal transmembrane region, while SNAP25 contains two SNARE motifs and is anchored on the membrane by palmitate-modified cysteine residues. These four α-helical SNARE motifs can bind to form a stable coiled-coil structure creating a trans-SNARE complex. The helices are parallel in this bundle, so, a parallel four-stranded coiled-coil model for the structure of the trans-SNARE complex is proposed (figure 11A). Munc13 and Munc18 together ensure that the trans-SNARE components are in this parallel configuration (more information at the “SV fusion” paragraph) (Hanson, Roth, Morisaki, Jahn, & Heuser, 1997; Poirier et al., 1998; Sutton et al., 1998; Weber et al., 1998). The complex contains multiple layers of hydrophobic side chains and a central polar layer. The polar layer is conserved in all SNARE complexes and has led to the classification of the SNARE motifs into Qa, Qb, Qc and R types, according to their predicted locations in the four-a-helical complex. Q types have a polar layer that consists of a glutamine (Q) residue, while in R type this layer consists of an arginine (figure 11B) (Antonin, Fasshauer, Becker, Jahn, & Schneider, 2002; Fasshauer, Sutton, Brunger, & Jahn, 1998).

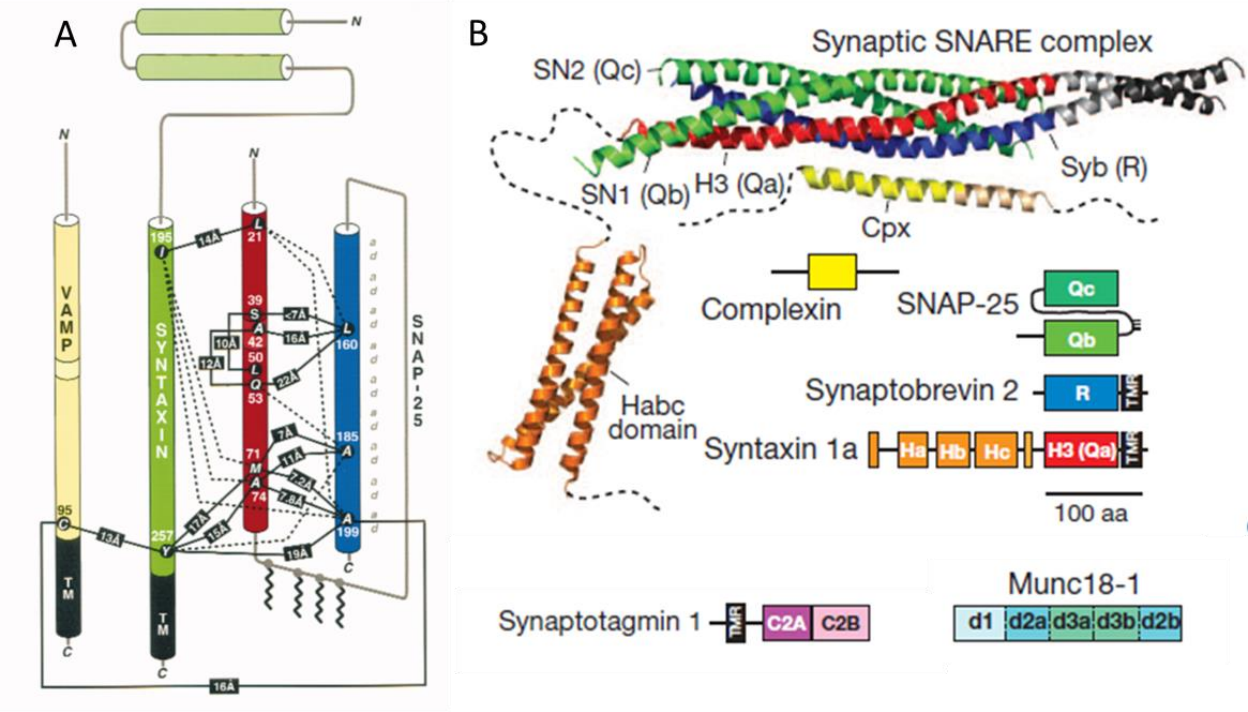

Figure 11: A: Schematic representation of SNARE complex components showing the parallel orientation of SNAP25, Syntaxin-1 and Synaptobrevin (Poirier et al., 1998)*. B: Domain structures of core proteins of the neuronal fusion machine and crystal structures of the synaptic SNARE complex. The four α-helical coiled-coil structure between SNAP25 (SN1 and SN2), Synaptobrevin (Syb) and the H3 domain of Syntaxin-1 (H3) can be observed.* (Jahn & Fasshauer, 2012)

The trans-SNARE complex plays an important role in SV exocytosis. Its formation provides the energy needed to overcome electrostatic repulsion between the SV and the target membranes and allows membrane fusion. This was shown by studies indicating that deletion of SNARE proteins resulted in strong impairments of neurotransmitter release (Broadie et al., 1995; Schoch et al., 2001; Jahn & Scheller, 2006; Delgado-Martínez et al., 2007; Rizo & Südhof, 2012;). Trans-SNARE complex formation is necessary for synaptic transmission. Therefore it is absolutely required for normal brain functions, such as learning, body movements and formation of memories (Zheng & Bobich, 1998).

SNAP25 is one of the proteins studied in this project. Even small alterations of the expression of SNAP25 can lead to a number of disorders including Alzheimer's (Clinton,

Blackman, Royston, & Roberts, 1994), schizophrenia (Thompson, Sower, & Perrone-Bizzozero, 1998), attention deficient hyperactivity disorder (Thompson et al., 1998), Down syndrome (Greber-Platzera, Fleischmanna, Nussbaumerb, Cairnsc, & Lubeca, 2003) and autoimmune disorders (Greber-Platzera et al., 2003). SNAP25 KO mice have been shown to develop a normal nervous system *in utero*. The growth of axons, targeting of synaptic contacts, and action potential-independent, spontaneous transmitter occur like in the WT. However, action potential -dependent release is completely abolished (Washbourne et al., 2002). Studies using HPF and FS on organotypic hippocampal slices isolated from embryonic mice at Nils Brose's lab, showed that SNAP25 KO synapses revealed a strong decrease in the number of docked SVs. Proximal SVs accumulated at ~4–8 nm from the AZ, which increased the number of SVs within 5-20nm from the AZ compared to the WT synapses. However, the total number of proximal SVs was the same in both cases. They, also, showed that the SV diameter in SNAP25 KO synapses was increased. They concluded that SNAP25 (but also the other SNARE proteins, synaptobrevin and syntaxin-1) is required for SV docking (Imig et al., 2014). Again, while these are very important studies, alterations of tethering proteins and SV locations induced by the preparation methods used necessitates investigation of this system by cryo-ET. Furthermore, there haven't been any studies that examine the SNARE complex in relation to tether organization.

1.10 SV fusion

In the resting state, syntaxin-1A is present at synapses in a heterodimeric complex with Munc18, which prevents binding of syntaxin-1A to other SNARE proteins and the formation of the trans-SNARE complex (Misura et al., 2000; Burkhardt et al., 2008). Munc13 dissociates the syntaxin from the aforementioned complex, because the MUN domain of Munc13 has a higher affinity for the isolated syntaxin than the Munc18/syntaxin complex (Rizo & Südhof, 2012). Both Munc13 and Munc18 are necessary for the correct assembly of the SNARE complex by ensuring that all the SNARE complex components are in parallel configuration (the N-terminals of all four

helices are on the same side) (Lai et al., 2017). According to the partially zippered model, currently the most prevalent one, the formation of the pre-fusion complex, composed of partially zippered trans-SNARE complex, complexin-1 and synaptotagmin-1 brings SVs to the primed state (Rizo & Südhof, 2012). In this state, SVs can fuse to the plasma membrane and release neurotransmitters upon Ca^{2+} influx (review in Brunger et al., 2019). However, an alternative non-zippered model proposes that SNAREs do not connect *in trans* before the Ca^{2+} signal arrives. Instead, proteins of the AZ (mostly RIM and Munc13) position the SV precisely on top of the patch of plasma membrane where t-SNARE complex is located. In this model, synaptotagmin may already connect the SV with the plasma membrane. Upon Ca^{2+} influx, the SV comes closer to the membrane, and v and t-SNARE complexes form the SNARE complex, which leads to SV fusion (figure 13) (Jahn & Fasshauer, 2012).

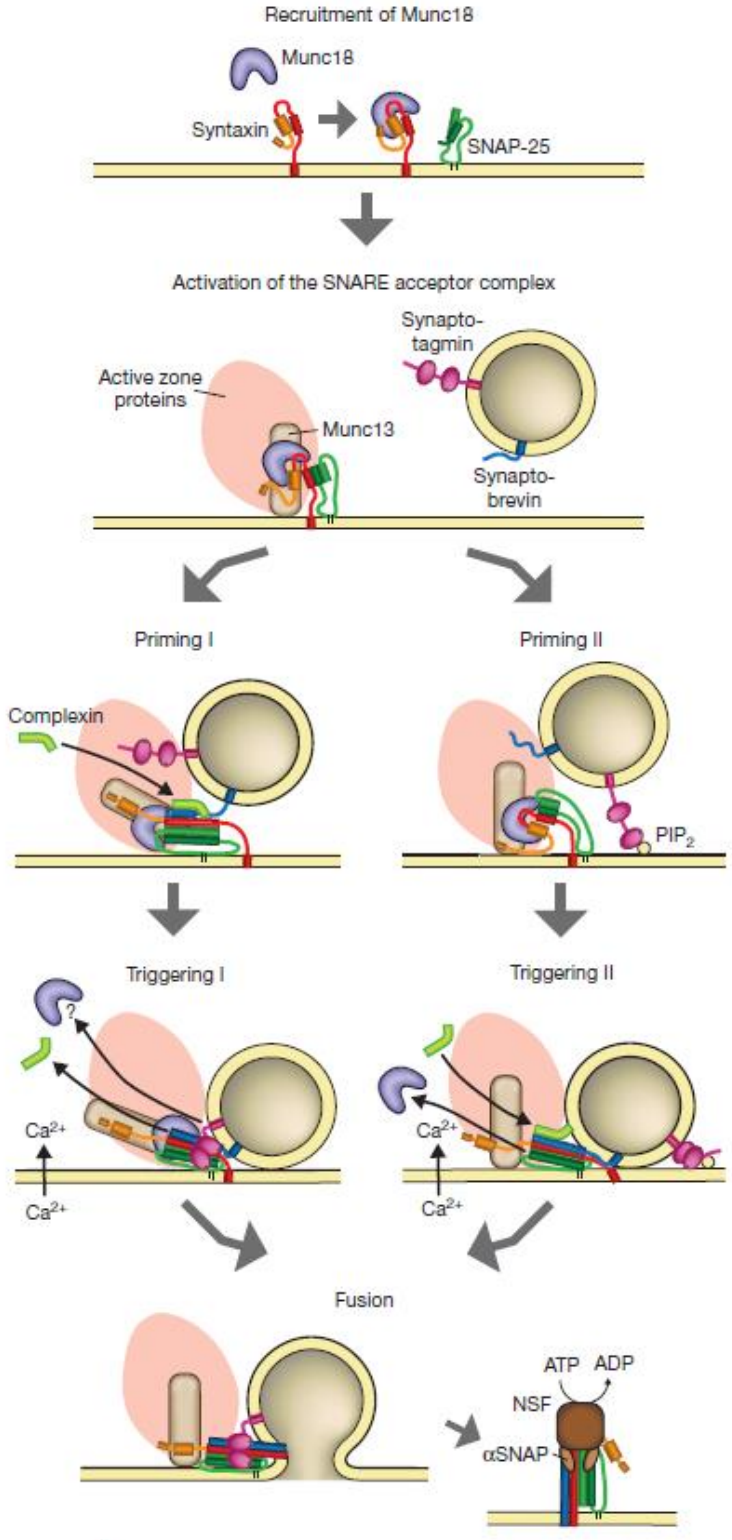

Figure 12: The two models for the formation of the pre-fusion complex: partially-zippered (left) versus non-zippered (right). (Jahn & Fasshauer, 2012)

As a consequence of an action potential reaching a presynaptic terminal, voltage gated Ca^{2+} channels open and Ca^{2+} enters the presynaptic cytosol. The increase of cytosolic concentration is detected by Ca^{2+}-sensor synaptotagmin. Synaptotagmin is necessary to detect Ca^{2+} influx because SNAREs themselves do not exhibit any Ca^{2+} sensitivity (Geppert et al., 1994; Fernández-Chacón et al., 2001). It was earlier thought that upon Ca^{2+}-binding, synaptotagmins activate fusion by bringing the SV and plasma membranes closer to each other. However, according to the recent release-of-inhibition model, Ca^{2+} binding to synaptotagmin-1 releases the inhibition the latter exerts on the SNARE complex and initiates the SV fusion with the presynaptic membrane (Zhou et al., 2017; Brunger et al., 2018). Subsequently, Ca^{2+} dislodges synaptotagmin-1 from the SNARE complex. It is currently not known what happens to the dislodged synaptotagmin-1. It may be inserted into a nearby membrane or it binds to a different region on the SNARE complex (Brunger et al., 2019). The primary SNARE/synaptotagmin-1 binding interface may assist in inducing membrane curvature upon Ca^{2+}-binding. It has been proposed that, when Ca^{2+} binds to the C2B domain of synaptotagmin-1, the Ca^{2+} binding loops of this domain partially insert into the membranes (both SV and plasma membrane). At the same time, the trans-SNARE complex is free to fully zipper. Together, these actions move the membranes closer than the critical distance (0.9nm), promoting membrane fusion (Zhou et al., 2015). The fact that all factors needed to promote fusion are already in place, could explain the high speed of the fusion block release and the SV fusion upon Ca^{2+} entering the presynaptic cell (Brunger et al., 2019).

It is shown that, at least, two SNARE complexes are required for Ca^{2+}-triggered fusion (Sinha et al., 2011; Shi et al., 2012). However, it has not been possible, yet, to visualize these complexes. Multiple SNARE complexes can interact with each other via synaptotagmin-1, but the precise arrangement hasn't been elucidated until now (Zhou et al., 2017; Brunger et al., 2018). Finally, if the presence of at least one inhibited pre-fusion complex prevents the fusion of the SV to the plasma membrane, the release-of-inhibition model would be independent of the actual number of SNARE complexes involved in the fusion of one SV (Brunger et al., 2019).

After fusion, the trans-SNARE complex needs to be disassembled, so that individual SNARE proteins can be recycled. The adaptor protein SNAP (not to be confused with SNAP25)

and the ATPase N-ethylmaleimide sensitive factor (NSF), have been revealed to disassemble the trans-SNARE complex upon ATP hydrolysis (Söllner et al., 1993; Mayer et al., 1996; Hanson et al., 1997). NSF, SNAPs, and SNAREs form the so-called 20S complex, the starting state for the disassembly process. SNARE interacts both with SNAP (mainly αSNAP, which is the most studied member of the SNAP protein family) and with NSF, as shown from structural studies (White, Zhao, Choi, Pfuetzner, & Brunger, 2018). However, the molecular mechanism of NSF-mediated SNARE complex disassembly is still unknown.

1.11 Synaptosomes

Isolation of nerve terminals from the brain is a very useful technique, which has dramatically enhanced the ability of studying and understanding neuronal synapses both at the physiological and the molecular level (P. Dunkley, Rostas, Heath, & Powis, 1987; Whittaker, 1993). First, fresh tissue, isolated from a brain region of interest, is homogenized in an isotonic solution of appropriate viscosity by using an appropriate shear force (De Robertis, Pellegrino De Iraldi, Rodriguez De Lores Garnaiz, & Salganicoff, 1962; Gray & Whittaker, 1962). In this way, the nerve terminals (boutons) are torn from the axons. Often, part of the postsynaptic membrane and its attached postsynaptic density remain attached to the presynaptic bouton. The membranes subsequently reseal and enclose the nerve terminal contents (P. R. Dunkley, Jarvie, & Rostas, 1988; Whittaker, 1993). These reconstituted nerve terminals are called synaptosomes (Whittaker, Michaelson, & Kirkland, 1964). Although some of them are being destroyed during homogenization, most synaptosomes remain, and have the form and the functionality that closely mimic synapses *in vivo* (P. Dunkley et al., 1987; Whittaker, 1993).

Synaptosomes have been characterized in functional terms: they can produce ATP and maintain membrane potentials and ion homeostasis thanks to functional ion channels. Synaptosomal SVs can take up and release neurotransmitters, their membranes can be recycled by endocytosis, and the functional enzymes and proteins they contain are normally present

within nerve terminals (Balázs et al., 1975; Morgan, 1976; Peter R. Dunkley & Robinson, 1986; P. Dunkley et al., 1987; Whittaker, 1993; Ashton & Ushkaryov, 2005). However, they do not have the machinery to produce new proteins. They start to lose ATP as soon as they are brought to 37°C, but they remain active for at least four hours at 4°C (Whittaker, 1993).

In our lab, the structure of synaptosomes has extensively been studied by imaging vitrified frozen-hydrated, unstained synaptosomes from rodent brains by cryo-ET. The membranes (presynaptic, postsynaptic, SVs) are clearly visible, without any signs of aggregation. In the cytoplasm of the presynaptic terminal, the SVs are observed, as well as mitochondria and occasionally cytoskeletal elements such as microtubules or actin (figure 13A). Previous research showed that SV distribution shows a concentration peak in the proximal zone (0 – 45nm from the AZ). In the intermediate zone (45 – 75nm), the concentration has a minimum and in the distal zones (75 – 150nm and 150 – 250nm) the concentration is increased again (figure 13E). It was also found that SVs show extensive interconnectivity. Numerous filamentous structures (up to 40nm long, termed connectors) link SVs to each other (figure 13C). Many proximal SVs were found to be tethered to the AZ membrane by short filaments (tethers) of variable length (figure 13D). Only rarely a direct contact between SV and cell membranes was observed, as opposed to "docking" observed by EM of chemically fixed and dehydrated samples. Finally, the data from our group suggested that proximal SVs that have multiple tethers, belong to the Readily Releasable Pool (RRP) (Fernández-Busnadiego et al., 2010).

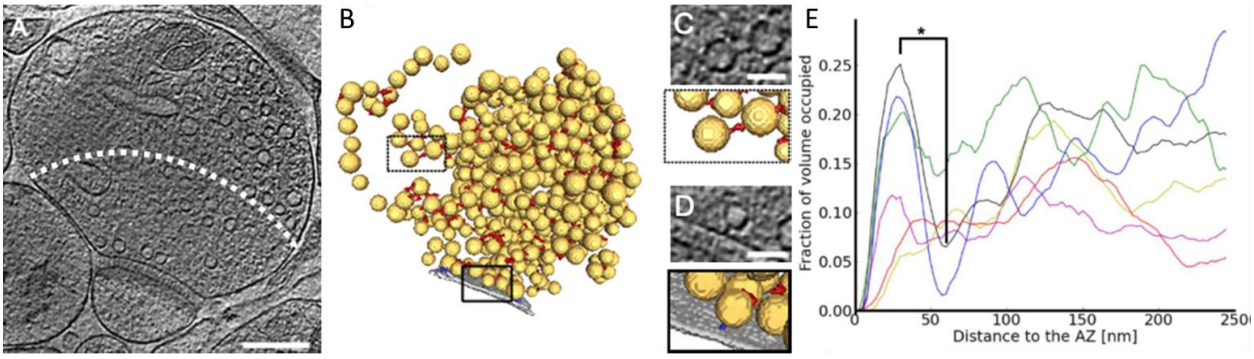

Figure 13: A: Tomographic slice of a synaptosome. The SVs, the synaptic cleft and the PSD are visible. Dashed line: first 250nm from the AZ. Bar: 200nm. B: 3D segmentation of SVs (yellow), SV connectors (red) and SV tethers (blue). Tomographic slices depicting a connector (C) and a tether

(D), and their 3D visualization. Bars: 50nm. E: Representative traces of SV distribution within presynaptic terminals of individual synapses. The concentration peak in the proximal zone and the concentration minimum in the intermediate zone are visible (P < 0.05). (Fernández-Busnadiego et al., 2010)

2. Aim of this Thesis

Synaptic vesicle (SV) priming and neurotransmitter release require an intricate coordination of multiple presynaptic proteins. A large body of previous research employed biochemical, genetic and biophysical methods to identify relevant proteins and determine their role in the release. Together with the high-resolution structural determination, these methods provided an array of possible interacting partners and led to models of neurotransmitter release. However, these methods could not discern the nano-scale organization of the proteins in their native state.

Studies that have used conventional EM techniques to observe this organization in situ relied on sample dehydration, resin embedding and heavy metal staining to increase the contrast. All these methods, however, are known to create structural artifacts. Imaging vitrified, fully hydrated samples by cryo-ET enables the study of biological macromolecules in their natural environment, without the induction of artifacts described above.

Previous work of our group using cryo-ET on vitrified synaptosomes, has shown that there are filaments that connect SVs with each other (connectors) and with the AZ membrane (tethers). The number and properties of tethers were shown to be indicative of the SV state towards the release.

The purpose of this thesis was to elucidate the role of specific proteins that have been proposed to form tethers, concerning the SV distribution and the tethering organization. The main technique used was cryo-ET, which allowed us to observe the changes caused by the lack of these proteins, without the creation of artifacts. In particular, we aimed to understand the role of RIM, Munc13 and SNAP25 by comparing tomograms of synaptosomes that lack one of these components to WT ones. Finally, we focused on Munc13 by analyzing the synaptosomal environment after treatment with a pharmacological activator of the protein.

3. Materials and Methods

3.1 Dissociated Neuronal culture preparation

One day before the neuronal preparation, the grids (Quantifoil R 1/4 SiO_2 Films, Au 200 mesh), were plasma cleaned (Harrick Plasma cleaner PDC-3XG) for 45s. This helped to remove any organic contamination from the grids and to apply a negative charge, thus creating a hydrophilic surface (Aebi & Pollard, 1987). Grids were placed in small 4 well dishes (Cellstar culture dishes, Cat. No. 627.170, Greiher Bio-One GmbH, Frickenhausen, Germany), one grid per well, with the coated side face-up. This was done on a clean bench, using tweezers sterilized on a flame. The dishes were kept under a UV lamp for 20min. 100µl of 1mg/ml PLL solution was gently added to each well. 10cm Petri dishes (100x20 Non-treated Culture Dishes, Sterile; Polystyrene; cat. No. CC7672-3394; Cyto One) were filled with 5ml 1mg/ml PLL solution, as well. All dishes were placed in an incubator (37^{o}C) and kept there overnight.

On the day of the preparation, the dishes were washed 3 times with DPBS. 2ml of the 5µg/ml Laminin solution was added in each dish containing grids and 5ml in each 10cm dish, and they were placed back in the incubator for 2hrs. The dishes were washed, again, 3 times with DPBS. If there were grids that were floating in the medium, tweezers sterilized on a flame were used to place them back to the wells. The dishes were filled with Neurobasal medium and stored in an incubator until cell seeding.

A pregnant mouse (CD-1) at E17-18 was sacrificed in accordance with the guidelines of the Max-Planck-Institute of Biochemistry. After being checked for reflexes, it was placed, with the ventral side up, on a Styrofoam surface and its paws were fixated on it using pins. The ventral area of the mouse was rinsed with 70% EtOH. A lateral cut was carefully made at the area of the uterus and then a coronal one until the ribs of the animal were exposed. The uterus was removed and placed on a 10cm petri dish filled with cold HBSS medium (4^{o}C). The embryos were exposed

by cutting the embryonic sack and were decapitated. Under a dissecting microscope, the skulls were opened using two pairs of tweezers and the brains were isolated. For each brain, the cerebellum was removed and the meninges were carefully peeled off. The brain hemispheres were separated and the hippocampi were located. They were removed from the rest of the brain and placed in a falcon containing cold HBSS medium (4^{o}C).

Trypsinization solution was mixed with the HBSS medium at 1:1 volume ratio in a falcon tube, and the hippocampi were incubated in a water bath (37^{o}C) for 16min. After that, the hippocampi were left to sink to the bottom of the tube, and the solution was carefully removed. Neurobasal medium was used to wash the hippocampi 3 times (the first time, 5% of FBS serum was added as well). Then, the hippocampi were triturated in the presence of Neurobasal medium: they were pipetted up and down against the bottom of the falcon 20 times, using a cut off 1ml pipette tip. They were, then, triturated 10 more times with a normal 1ml pipette tip. More Neurobasal medium was added, and the mixture was spun at 120g for 5min. The supernatant was carefully removed and fresh Neurobasal medium was added with a 1ml pipette tip (the cells were pipetted up and down 10 more times).

The cells were counted by mixing 10μl of the cell solution with 10μl of Trypan Blue solution, (0.4%, ThermoFisher Scientific) and adding 10μl of that in a Neubauer Hemocytometer. Only the cells that were not blue (meaning that their membrane was not broken so that Trypan Blue could enter in their cytoplasm) were counted. The mean number of cells from all 4 squares of the Neubauer Hemocytometer was multiplied by 2 (because the cells were diluted with Trypan Blue in a 1:1 ratio) and this was multiplied by 10^4. This formula gave the number of cells per 1ml of solution. The sample was, then, diluted to the desired concentration by adding Neurobasal. More specifically, this concentration would be:

- 45000 cells in a volume of 150μl on each grid
- 1.2million cells in a volume of 10ml in each 10cm dish

The Neurobasal medium was completely removed from the PLL-laminin-coated dishes before the cells were added.

The dishes were, very carefully, placed in the incubator. After 2 hours, 2ml of warm Neurobasal medium was added in each 4 well dish, very gently as to not disturb the cells. 5ml of

warm Neurobasal medium was added in each 10cm dish. After 3 days, half of the medium was removed and replaced with fresh warm Neurobasal medium. The medium was, then, replaced once per week, until the neurons were fully matured (DIV 21). Before each medium exchange, the cultures were thoroughly monitored: the seeding of the neurons, their viability and their development were carefully noted. Also, the proliferation of glial cells was inspected. If the number of glial cells was considered overwhelming, FuDR was added to the medium, to stop them from multiplying. FuDR (fluorodeoxyuridine) is a drug that has been reported to increase neurite growth by changing the composition and number of the non-neuronal cells (Oorschot, 1989).

3.2 Buffers for preparation of dissociated neuronal cultures

DPBS (Dulbecco Phosphate Buffer Saline)

- Dissolve the pre-mixed powder (Sigma, D5773) in 1L ddH_2O
- Autoclave

HBSS (Hank's Balanced Salt Solution) medium, 500ml

- HBSS (ThermoFisher, 14170-088)
- 10mM HEPES (1M Stock, ThermoFisher 15630-056)
- 1x GlutaMAX (1M Stock, ThermoFisher 35050-038)
- 1x Pen/Strep (100x Stock, ThermoFisher 15140-122)

Neurobasal medium, 500ml

- Neurobasal (ThermoFisher 21103-049)
- 1x GlutaMAX
- 1x Pen/Strep

- 1x B27 serum-free supplement (ThermoFisher 17504044)

Trypsinization solution

- HBSS medium
- 2.5 % Trypsin (10x Stock)
- 1% DNase I solution (10x Stock, Roche 10104159001)

Borate Buffer, 500ml

	c (M)	M (g/mol)	m (g)
$Na_2B_4O_7*10H_2O$	0.1	381.32	19.066

In ddH2O. Adjust to pH=8.5, autoclave.

1mg/ml Poly-L-lysine solution

- 100mg/ml Poly-L-lysine in stock (Sigma P2636)
- 0.1M Borate Buffer

5µg/ml Laminin solution

- 1mg/ml Laminin in stock (Trevigen 3401-010-02)
- DPBS

FuDR (5-Fluoro-2'-deoxyuridine)

- 1000x Stock (Sigma F0503)
- Neurobasal medium

FBS (Fetal Bovine Serum) (ThermoFisher 16000)

3.3 Synaptosome preparation from adult rodent hippocampi

Young adult rats and mice were sacrificed in accordance with the guidelines of the Max-Planck-Institute of Biochemistry. A rat was placed in a glass Desiccator with a tissue paper dampened with 2ml chloroform. After approximately 5 – 8min the rat showed no signs of movement. The animal was removed and a pair of tweezers was used to check its reflexes. The rat was decapitated with a guillotine (a cut behind the animal's ears). Alternatively, a mouse was removed from the cage, placed on top of it and a cervical dislocation was performed using a pair of tweezers. The mouse's reflexes were checked and it was decapitated using a guillotine.

The head of the animal was placed with its ventral side faced down, a cut of the skin was performed along the caudal – rostral axis and the skin was removed, revealing the skull. A skull breaker was, then, used to make two lateral incisions on the superior part of the cranium. With the help of a small spatula, the top part of the skull was removed, exposing the brain. The brain was rinsed with homogenization buffer at 4^{o}C, and was scooped from the skull, by cutting the optic chiasm with a spatula precooled to 4^{o}C. The brain was embedded in cold homogenization buffer and everything was poured in a 10cm petri dish (already placed on ice) covered with a filter paper (Whatman filter paper 1 Qualitative circles 90mm diameter, Cat No 1001 090). The brain was positioned with its ventral side down. Using a curved scalpel blade, the cerebellum was removed by making a coronal cut. A sagittal section in the middle of the brain cut the *corpus callosum* and separated the two hemispheres. Each brain hemisphere was placed with its lateral side down. With the help of two spatulas, the brainstem was removed (one spatula held the rest of the brain fixed, and the other removed the brainstem). Using the same technique, the hippocampus was pulled towards the caudal side of the brain. Using one of the spatulas, the hippocampus was carefully cut from the rest of the brain. The same was done for the hippocampus of the other hemisphere. Immediately after being removed, the hippocampi were put in a beaker with 4ml of homogenization buffer. The whole mixture was poured in a glass tube.

The sample was homogenized using a Teflon piston which was already connected to a drill in a cold room (4^{o}C). As soon as the whole piston was inserted to the mixture, one stroke was performed at low speed (100rpm) to break most of the tissue apart. Then, the speed was increased (700rpm) and 7 more strokes were performed. This broke the smaller pieces of the tissue apart. When the 7 strokes were done, the piston was carefully removed from the solution creating as few bubbles as possible. Throughout the whole process, extra care was taken so that the piston was not pressed hard against the tube and no unnecessary hand contact was made on the outside at the bottom of the tube.

The homogenate was added in a 50ml falcon tube and it was centrifuged at 2000g for 2min (4^{o}C), using an SS-34 rotor (Sorvall). The supernatant (S1) was carefully removed taking care that no pellet was taken away. The pellet (P1) was, then, resuspended with sucrose (1x) and centrifuged again at 2000g for 2min (this was done to ensure that as many synaptosomes as possible would end up to the supernatant). The supernatant (S1') was also collected and added to S1. The pellet (P1') was discarded. This centrifugation step was done to remove any heavy material (non-homogenized tissue, nuclei, whole cells etc.). The S1 was centrifuged at 9500g for 12min (4^{o}C) using the same SS-34 rotor. The supernatant (S2) was discarded and the pellet (P2) was thoroughly resuspended with Ca^{2+} free HBM. During resuspension, no bubbles were made and touching the bottom of the tube on the outside was avoided.

The final concentration of the sample was determined by diluting it with Ca^{2+} free HBM and measuring its Protein-UV using an Implen Nano Photometer. Concentration little below 1mg/ml was deemed optimal for plunge freezing. After the final concentration had been measured, the sample was added in 1.5ml Eppendorfs and was centrifuged at 10000g for 10min (4^{o}C) using a tabletop centrifuge (Eppendorf Centrifuge 5417 R). The supernatant was discarded and the pellet was kept on ice until plunging.

3.4 Synaptosome preparation from dissociated neuronal cultures

Roughly 2 weeks after the neuronal preparation (DIV 13 – 16), the synaptosome preparation began. The 10cm dishes containing the neuronal cultures were taken out of the incubator (37^{o}C), their medium was removed and they were briefly rinsed with 2ml of Tyrode's buffer at room temperature. After the Tyrode's buffer was removed, the dishes were placed on ice and 500μl of homogenization buffer (4^{o}C) was added. The neurons were scrapped in this buffer and were transported to a glass tube with a Pasteur pipette (everything was kept at 4^{o}C). After every dish of cultures that belonged to the same treatment had been scrapped and added to the tube, the homogenization process started as described at the previous protocol: one homogenization stroke at low speed (100rpm) and 7 more strokes at 700rpm. The drill was stopped and the piston was, carefully, removed from the solution.

The homogenate was loaded into 2ml Eppendorf tubes and centrifuged at 2000g for 2min (4^{o}C) using a tabletop centrifuge (Eppendorf Centrifuge 5417 R). The supernatant (S1) was carefully collected so that no pellet was removed with it. The pellet (P1) was resuspended with sucrose buffer and centrifuged again at 2000g for 2min. The supernatant (S1') was also collected carefully and, along with S1, were loaded into fresh 2ml tubes. They were centrifuged at 9500g for 12min (4^{o}C). The supernatant (S2) was discarded and the pellet (P2) was resuspended with Ca^{2+} free HBM.

The protein concentration of the resuspended solution was, then, measured, using a NanoDrop^{TM} spectrophotometer (ThermoFisher). A good density for this experiment was at a concentration a bit less than 1mg/ml, which was usually achieved by diluting the solution with Ca^{2+} free HBM. The solution with the desired concentration was loaded in 1,5ml tubes and centrifuged at 10000g for 10min (4^{o}C). The supernatant was discarded and the pellet was kept on ice until plunging.

All the embryos of a single mother were combined to make one neuronal preparation.

3.5 Synaptosome preparation from organotypic brain slice cultures

The synaptosomal preparation started approximately one month after the slices had been plated on a dish (DIV 28-30). These slices were obtained from E18 (mixed background) or P0 (C57/N) mice. The buffer in which the slices were incubated was removed and the slices were briefly rinsed with Tyrode's buffer at room temperature. They were, then, scooped with a brush, and were dropped in a glass tube, which contained the cold homogenization buffer. For each slice added to the tube, there were 50µl of buffer. After all the slices of one condition were added, a Teflon piston was inserted in the tube, and the homogenization procedure began, as described before (one stroke at 100rpm and 7 strokes at 700rpm). From that step on, the protocol was the same as the one described for the dissociated neuronal cultures: one centrifugation at 2000g for 2min (repeated twice) in order to remove the heavy parts (supernatant was saved), and one centrifuge at 9500g for 12min, to remove the light parts (pellet was saved). The pellet was, then, resuspended with Ca^{2+} free HBM and its protein concentration was measured using an Amersham Biosciences Ultrospec 3100 Pro Spectrophotometer (GE Healthcare). In this project, a desired concentration was around 0.3 – 0,5mg/ml. After that, the sample was centrifuged at 10000g for 10min and the pellet was stored on ice until plunging.

3.6 Buffers for synaptosomal preparation

Normal Tyrode's Buffer, 500ml

	c (mM)	M (g/mol)	m (g)
NaCl	120	58.44	3.51
KCl	3	74.55	0.11
$MgCl_2 * 6H_2O$	1.25	203.31	0.13
$CaCl_2 * 2H_2O$	1.25	147.02	0.09
HEPES	25	238.30	2.98
$NaH_2PO_4 * H_2O$	0.5	137.99	0.03
D-glucose	30	180.16	2.70

In ddH2O. Adjust to pH=7.4

Sucrose buffer (1x), 500ml

	c (M)	M (g/mol)	m (g)
Sucrose	0.32	342.3	54.768

In ddH2O. Adjust to pH=7.4

Homogenization buffer

- 1 tablet of protease inhibitor cocktail (cOmplete, Mini, EDTA-free Protease Inhibitor Cocktail, Cat. No. 11836170001, Sigma-Aldrich Chemie GmbH, Taufkirchen, Germany)
- 10ml sucrose buffer (1x)

Hepes-buffered medium (HBM) (10x), 500ml

	c (mM)	M (g/mol)	m (g)
NaCl	1400	58.44	40.91
KCl	50	74.55	1.86
$NaHCO_3$	50	84,01	2.10
$NaH_2PO_4 * H_2O$	12	137.99	0.83
$MgCl_2 * 6H_2O$	10	203.31	1.02
D-glucose	100	180.16	9.01
HEPES	100	238.30	11.92

In ddH2O. Adjust to pH=7.4

Ca^{2+} free HBM (1x), 500ml

- 50ml HBM (10x) + 450ml ddH_2O

HBM + $CaCl_2$ (1x), 500ml

- 50ml HBM (10x) + 450ml ddH_2O
- 0.088g $CaCl_2$ * $2H_2O$ (MW=147.02; c=1.2mM)

3.7 Vitrification by plunge freezing

One hour before plunging, the pellet containing the synaptosomes was thoroughly and carefully resuspended with warm HBM + 1.2mM $CaCl_2$ and was incubated at 37°C. Quantifoil R 2/1 Holey Carbon Films, Au 200 mesh EM grids were placed carbon side up on a glass slide and were plasma cleaned (Harrick Plasma cleaner PDC-3XG) for 45sec. After incubation and immediately before plunging, the synaptosomal solution was mixed with BSA-coated 10nm gold nanoparticle solution (Aurion, BSA tracer Conventional 10nm reagent, Product Code: 210.133, Wageningen, Netherlands) in a ratio of 1:10. These fiducial markers had been previously centrifuged at 16000g for 25min (4°C) twice (the first time their original buffer was replaced by Ca^{2+} free HBM and the second time, their pellet was kept on ice until plunging). The pellet had been resuspended with warm HBM + 1.2mM $CaCl_2$ and incubated at 37°C until the mixture with the synaptosomes.

The plunge freezing was done using a manual plunger (designed and built by Max Planck's workshop). For this, a mixture of ethane and propane was used (Linde Gas ethane/propane mixture (37% ethane, rest propane) UN 3161, Pullach, Germany). To liquefy this mixture, the area around the ethane/propane compartment was cooled down with liquid nitrogen (LN_2). As soon as this compartment was cooled down, it was carefully filled with the air mixture, which, when enough pressure was applied, and with the help of the low temperature, started to liquefy. For optimal results, LN_2 needed to cover at least 2/3 of the outside of the ethane/propane compartment. When the plunger was cooled down, a pair of inverted tweezers was used to grab the plasma cleaned grid. Tweezers were placed on the dedicated place on the plunger and 4µl of the synaptosomal solution was applied on the grid (on the side of the carbon film). After leaving the sample on the grid to settle down for approximately 7sec, a filter paper was used (Whatman

filter paper 1 Qualitative circles 90mm diameter, Cat No 1001 090) to blot the excess sample from the grid. The filter was applied at a slight angle to the grid, and the blotting time was 5 – 7sec. After blotting, the pedal of the plunger was pressed, the tweezers were released and they were dropped inside the liquid ethane/propane compartment. The grid was swiftly transferred into the area outside the compartment that was filled with LN_2 and was placed in an in-house designed grid box than can hold up to 4 grids, for storage. This procedure was repeated for all grids. The grid boxes were collected in a perforated 50ml Falcon tube and stored in a large Dewar in LN_2 until EM imaging.

Vitrification for the RIM project was done in Bonn. Because the Uniklinikum Bonn had no plasma cleaner, the plasma cleaning of the grids was done with a table top Turbo Sputter Coater Med 010 (Balzers) from the Caesar Institute. The grids were plasma cleaned for 2min.

The grids used for Munc13 and SNAP25 projects were plasma cleaned in Göttingen using also a table top Turbo Sputter Coater Med 010 (Balzers) for 2min.

For the experiments in Bonn and Göttingen the plunge freezing was performed using a portable manual plunger (again, designed and built by Max Planck's workshop). Also, pure ethane (Westfalen AG, Ethane 2.5 99.5% Vol. % C_2H_6, Münster, Germany) was used for the vitrification. Ethane solidifies at a higher temperature than the ethane/propane mixture, so, the level of LN_2 used to cool down the plunger did not exceed the bottom of the ethane compartment.

3.8 Synaptosome preparation from adult rodent hippocampi for the ionotropic glutamate receptors project

A monoclonal antibody that specifically binds the amino-terminal domain, NTD (aa 175-430) of the GluA2 subunit of the AMPAr was used (GluR2 Monoclonal Antibody (6C4) from ThermoFischer Scientific, Catalog # 32-0300). The protocol that was used for isolating synaptosomes from adult rats has been described above. The only difference was that, 20min

before plunging, the GluR2 antibody was added (1:100 or 1:30 dilution) to the synaptosomal solution incubated at 37°C.

Similar to the GluR2 preps, 20min before plunging, ZK 200775 hydrate (Merck, Catalog # Z4777) or (S)-5-Nitrowillardiine (NOW) (Abcam, Catalog # ab120063) was added to the synaptosomal solution (5µg/ml for ZK or 1mg/ml for NOW).

3.9 Cryo Electron Tomography

Tomographic series were acquired on ThermoFisher Titan Krios, a transmission electron microscope equipped with a field emission gun (FEG), a Gatan imaging filter (GIF), a Volta phase plate (VPP, Danev, Buijsse, Khoshouei, Plitzko, & Baumeister, 2014) which allows the acquisition of high contrast images at nearly zero defocus (-500nm) and a Gatan K2 Summit direct electron detector (DDD, 4k x 4k). The sample loading to Titan Krios was performed by an automatic loading system.

For these projects, the FEG was set at 300kV acceleration voltage, and the microscope was operated in low dose mode (Abraham J. Koster et al., 1997). The GIF was set in zero-loss mode (20eV slit width), and the K2 was operated in counting mode with dose fractionation.

After loading the samples in the microscope, the direct alignments were performed. Specifically, the beam tilt pivot point in X and Y axis, the rotation center, and the C2 aperture were aligned. The astigmatism of the beam was corrected, as well. The desired dose on a single image can be determined by changing the spot size and the intensity of the beam. All the alignments were done at the magnification and spot size at which the tomograms were acquired. After the direct alignments, the phase plate was inserted and aligned.

SerialEM (Mastronarde, 2005) was used for navigating, changing magnifications and saving pictures, and Digital Micrograph (Gatan) to control the K2 direct electron detector. The grids were scanned at medium magnification (4800x pixel size: 3.064nm) in search of synaptosomes. They usually resided at the outskirts of larger accumulations of biological

material. There were, probably, more synaptosomes towards the center, but the thickness of the material made the acquisition impossible. At this magnification, the synaptic cleft and the mitochondria were visible. If any of these was detected a picture at high magnification (33000x pixel size: 0.439nm) was taken. At this magnification, in addition to the aforementioned areas, the post synaptic density (PSD) and the SVs could be detected. The presence of all these components were used as criteria for the detection of synaptosomes. The stage position of the selected synaptosome was saved. After 5 to 10 synaptosomes were found (depending on the time left on the microscopy session, or the number of grids that needed to be studied), the navigator window of SerialEM was used to organize the selected positions for batch tomography acquisition. Tomograms were automatically recorded at each spot of interest.

Before the acquisition of each tomogram, the phase plate was moved to its next position and this spot was charged by the beam, in order to create a phase shift. The charging time depends on the phase plate and needed to be calculated by determining CTF on a high-dose image. Next, the stage was moved to the first tomogram. The eucentric height was adjusted and the image was being focused. This did not happen on the area of interest itself, as the extended exposure to the beam, would burn the synaptosome. The focusing was done 3.5 – 5μm away from the synaptosome, on the tilt axis. Then, the tomogram was being recorded, following a dose-symmetric scheme (Hagen et al., 2017), using a script written by Dr. Vladan Lučić and Dr. Philipp Erdmann. In this project, the increment used was either 1.5^{o} or 2^{o}, and the maximum tilt angles were +60^{o} and -60^{o}. Depending on the increment used, the total number of projections were either 81 (for 1.5^{o} increment) or 61 (for 2^{o} increment). The exposure time for the projection at 0^{o} was calculated by dividing the total exposure on each tomogram (it should not exceed 80e^{-} /A^{2}) with the total number of projections, and then, with the dose on a single projection. The exposure time for projections was increased with tilt angles to compensate for the increasing apparent thickness of the biological sample in the direction of the electron beam by using 1/cosine of tilt angle.

Projections were recorded in 16-bit tiff format by using dose fractionation. More specifically, one projection consisted of frames which, at 0^{o}, have 1/10 of the total exposure of

the projection. As a result, ten frames were recorded at 0°, and the number of frames was increased in higher tilts proportional to the increasing exposure time.

3.10 Tomogram reconstruction

A raw tomographic series consist of multiple frames acquired at each tilt angle. SerialEM generates a projection stack where each projection is simply a sum of the corresponding frames, and a mdoc file that has information about each tilt such as the tilt angle, the stage position, the defocus value and other parameters. In addition, the gain reference and the dark reference images are generated. The gain reference is a high-exposure image of an empty spot, which shows flaws of the direct detector (burned pixels, dark areas etc.). Throughout the projects, two methods of frame correction regarding the gain reference were used. In the first one, the frames were gain-corrected before saving, during the tomogram acquisition. In the second method, the frames were saved without correction, and the gain reference was saved separately. In both cases, MotionCor2 (Li et al., 2013) was used to align the frames within each projection and to apply the gain reference in the second method. A new stack file was, then, created using the aligned frame tilts. This was done by using Pyto package written by Dr. Vladan Lučić (Lučić, Fernández-Busnadiego, Laugks, & Baumeister, 2016). Projections were aligned and tomograms were reconstructed using IMOD (Kremer, Mastronarde, & McIntosh, 1996). In short, first the X-rays were removed, and the projections were coarsely aligned, by using cross-correlation, without changing the data type. For fine alignment, fiducial markers were seeded manually in the 0° image and were tracked automatically for the remaining projections. In some cases, especially in thick samples, bead tracking was fixed manually. Constraints on rotations and tilt angles of individual projections, and on beam tilt were incrementally relaxed. If the error was reduced, the changes were saved. Otherwise, the constraints were returned to the original values. Tomogram positioning was omitted. The projections were low-pass filtered at the frequency corresponding to the final pixel size and binned with factor four without linear

interpolation to generate the final aligned series. Tomograms were generated with weighted back projection method with a radial filter cutoff at 0.45. Linear density scaling factor was set so that intensity values range between -15,000 and 15,000, based on information extracted from the tilt.log file created by IMOD. During post-processing the tomogram was trimmed in Z-direction.

3.11 Selection of tomograms

Tomograms that were used for further process were selected using the following criteria: first of all, they needed to have enough contrast so that the individual parts (like SVs, membranes etc.) were clearly visible. Then, the synaptosomes had to be in an optimal (healthy) biological state. Namely, a mitochondrion with intact outer and inner lipid membrane and presence of cristae had to be in close proximity which would show that there is a proper supply of ATP (review in Cogliati et al., 2016). Moreover, the SVs had to be round instead of elongated and showing signs of degradation, and the presence of endosomes and large vacuoles had to be minimal. Finally, the presynaptic and postsynaptic structures had to be uninterrupted and enclosed by a smooth membrane, as well as connected by synaptic cleft proteins (figures 14A, 14B).

3.12 Segmentation of membranes and large regions

A semi-automated segmentation workflow (Fernández-Busnadiego et al., 2010), was used to segment membranes and other large structures. Initially, the presynaptic membrane and the equatorial planes of the SVs within a distance of 250nm from the AZ were manually segmented in Amira (FEI) (figure 14C). Large areas such as mitochondria, microtubules and vacuoles were segmented as well. All structures were labeled by unique ids. A script from the Pyto package was used to expand the equatorial planes of the SVs into spheres. Then, using another script, the

membrane and sphere segments were extended in a defined radius (in this case at 50nm) over unlabeled region (cytosol) and this extension was used as the segmentation region.

3.13 Detection and analysis of membrane-bound complexes

The following tasks were done for all individual tomograms using Pyto package (Lučić et al., 2016). The size, greyscale levels and distribution of the SVs within the presynaptic terminal were measured using the vesicles script. Filaments that connect different membranes with each other were automatically detected at multiple threshold levels using the hierarchical connectivity algorithm (script connectors). The higher limit of the threshold range depended on the average pixel values of the segmentation region, which was determined by the regions script. The lower threshold was set to the lowest threshold value at which segments were detected. The number of thresholds was similar in all analyzed tomograms (around 30). These filaments, were, then classified as tethers, if they were connecting SVs to the AZ (figure 14C), or as connectors, if they were connecting SVs to each other. The length, volume and number of these filaments (both in total and per SV) were measured and analyzed.

The analysis results from all individual tomograms were subsequently grouped by experimental conditions and statistically analyzed.

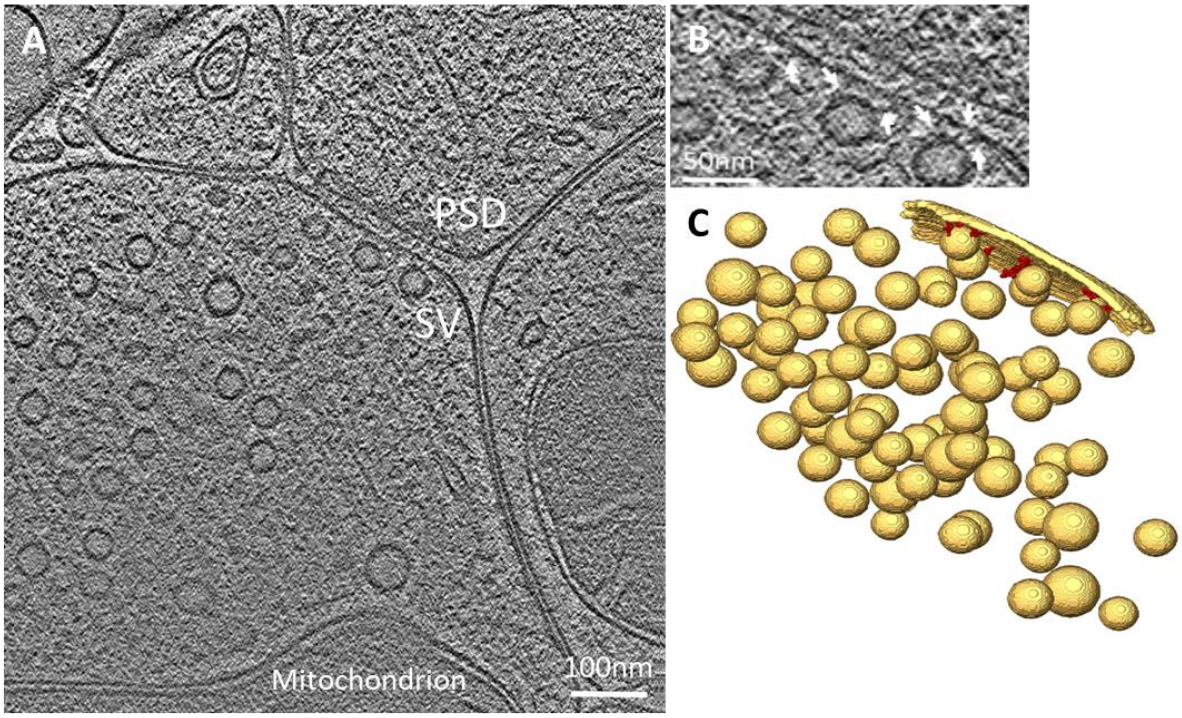

Figure 14: A: Tomographic slice of a synaptosome. A mitochondrion, the synaptic vesicles (SV), the synaptic cleft and the postsynaptic density (PSD) are clearly visible. B: Zoomed-in part of the tomographic slice from A that shows the SVs at the proximal area of the AZ. The white arrows depict the tethers. C: 3D segmentation of SVs and presynaptic membrane (yellow) as well as the tethers (red).

3.14 Statistical analysis

The analysis of connector and tether morphology, as well as SV size and distribution, were plotted with matplotlib (Hunter, J.D. Hunter, 2011). The confidence tests used during the analysis were Student's t-test for Gaussian distributed values, Kruskal-Wallis test for values not following a normal distribution and Chi-square test for values in discrete bins. Pearson's coefficient and t-test were used for correlation analysis. In all graphs, confidence values were indicated as: *: $p < 0.05$; **: $p < 0.01$; ***: $p < 0.001$.

3.15 Number of tomograms for each project

RIM

Condition	Tomos acquired	Tomos reconstructed	Tomos segmented	Tomos analyzed
WT	16	7	5	4
TKO	45	29	5	5
WT w/o PI	17	4	0	0
TKO w/o PI	8	6	4	4

Munc13

Condition	Tomos acquired	Tomos reconstructed	Tomos segmented	Tomos analyzed
WT	39	34	14	14
DHET	17	12	8	8
DKO	28	25	14	13
WT + PDBu	14	10	8	8
DKO + PDBu	15	11	9	9

SNAP25

Condition	Tomos acquired	Tomos reconstructed	Tomos segmented	Tomos analyzed
WT	24	11	9	9
KO	33	27	14	14
KO + PDBu	16	10	7	7

AMPAr

Condition	Tomos acquired	Tomos reconstructed	Tomos segmented	Tomos analyzed
GluR2_100	9	8	7	7
GluR2_30	7	7	6	6
NOW	4	4	0	0

Trans-synaptic columns

Condition	Tomos acquired	Tomos reconstructed	Tomos segmented	Tomos analyzed
Control	13	13	9	6
Stimulated	21	21	8	5

4. Results

4.1 The role of RIM protein family in organizing presynaptic architecture

4.1.1 Preparation of synaptosomes from dissociated neuronal cultures

The purpose of this project was to study the role of RIM protein family on tethering organization by cryo-ET. To achieve this, we followed the procedure developed before in our group, whereby genetically modified synaptosomes are imaged by cryo-ET, presynaptic complexes are quantitatively analyzed and the results are statistically compared with those obtained from WT synaptosomes.

However, we could not prepare neocortical synaptosomes from adult mutant mice like before because the genetical ablation of all RIM isoforms is postnatally lethal (Kaeser et al., 2011). Therefore, we decided to use a mouse line where the removal of RIM isoforms can be induced by the cre/loxp system (Sauer, 1987). To obtain RIM-free synaptosomes, we had to make dissociated embryonic hippocampal neuronal cultures from these mice, induce the mutation *in vitro*, allow sufficient time for synaptogenesis (DIV 13-16) and prepare synaptosomes from neurons grown in culture. The breeding of mice, the preparation of neuronal cultures and the induction of mutations were performed by our collaborators from Prof. Dr. Susanne Schoch-McGovern's lab at University of Bonn Medical Center.

Because synaptosomes obtained from dissociated neuronal cultures were not investigated by cryo-ET before, our first task was to optimize this procedure. What follows is the list of synaptosomal preparations we obtained together with the protocol optimization steps.

Preps 1 – 4:

For these preparations, we used the standard protocol for synaptosome preparation from dissociated neuronal cultures that has been used before for biochemical studies (Chang et al., 2012). In short, the neurons were grown on 6-well dishes (2cm per well). At DIV 14 - 16 we rinsed them with PBS before the addition of the homogenization buffer and scrapped the cells from the dishes. We used a filter (5µm pore size) to separate larger chunks of material from the synaptosomes. Lighter parts were removed by a medium-speed centrifugation, and the resuspended pellet was vitrified by plunge-freezing. Imaging under the electron microscope showed properly vitrified, membrane-enclosed cellular material. Overall synaptosomes looked healthy, but despite several microscopy sessions devoted to these samples we could find only a very small number of them.

Prep 5:

Two changes were made for this preparation. To make sure synaptosomes were properly detached from axons and dendrites, neurons were manually homogenized after scrapping, using a Teflon douncer. To separate heavy parts from the sample, we performed a slow centrifugation instead of using the filter. Similar to the previous preparations, a very small number of synaptosomes was observed.

Prep 6:

We reasoned that it might be beneficial to modify the protocol to make it more similar to the synaptosomal preparation from adult rodent brains that was previously used for cryo-ET. We rinsed the neuronal cultures with Normal Tyrode's buffer instead of PBS. Also, we decided to purify the crude synaptosomal fraction obtained after the medium centrifugation, in order to get more synaptosomes. For this, the supernatant of the crude fraction was centrifuged on a Percoll gradient. This method was used before in our group for purifying synaptosomes from adult brains. However, the amount of material to be purified in this project was much smaller than before. So, the following modifications were made: we used 11x34mm tubes (Ultracentrifugation Tube, Open-Top, PA, 11x34mm, Science Services GmbH, Munich, Germany) in which we added three concentrations of Percoll (Percoll density gradient media, GE Healthcare Europe GmbH,

Freiburg, Germany): 3%, 10% and 23%, all in 0.32M sucrose solution. We used 300µl of each concentration, with the heaviest (23%) at the bottom and the lightest (3%) on the top. Then, we added 200µl of the crude synaptosomal solution on top of the gradient. The sample was centrifuged at 25000g for 4min. After the centrifugation, three bands of material were visible in the tubes: the top one was previously shown to contain membranes and myelin, the middle one contained synaptosomes and the bottom one contained mitochondria (Peter R. Dunkley, Jarvie, & Robinson, 2008). We carefully removed the interface between 10% and 23% Percoll using a Pasteur pipette. In the standard procedure, this solution is diluted with Ca^{2+} free HBM and centrifuged in order to remove the Percoll. However, the volume of the sample was very small, so it was just diluted with HBM + $CaCl_2$ (2x) and H_2O (10% synaptosomal solution from the Percoll gradient, 40% H_2O and 50% HBM + $CaCl_2$ (2x)) and this solution was used at plunging. After studying the grids from this prep in the electron microscope, we found properly vitrified biological material, but it was not healthy (presynaptic "buttons" with smeared material instead of SVs) and the sample in general, was very dirty (a large part of the grid surface was covered with small, spherical-like shapes, something that made the search for synaptosomes more difficult). We concluded that this was probably because of the presence of Percoll on the grid. No viable synaptosomes were found from this preparation.

Prep 7:

To increase the interaction between neurons, and thus, increase the synaptogenesis, we used larger dishes, 10cm instead of the 6-well ones. We omitted Percoll gradient; the crude fraction from the medium centrifugation was used for plunging. The absence of Percoll significantly increased the clarity of our grids, resulting in nicely vitrified biological material. Some synaptosomes were observed here, but their number was similar to the previous preparations.

Preps 8 – 11:

We also reasoned that increasing the concentration of synaptosomes during the preparation might give improved results. To achieve this, we pooled neuronal cultures from multiple preparations, thus increasing the volume of the sample. This did not make a big

difference compared to the previous preps. Again, a very small number of synaptosomes was observed.

Prep 12:

No protease inhibitor cocktail (PI) was used for the RIM1α KO project. So, we decided to make a preparation without PI. The homogenization buffer included only sucrose. We took extra care as to all the steps from the cell scrapping onwards were done strictly at 4°C, to keep the proteases inactive. The rest of the protocol remained the same. There was biological material present here and the grids were properly vitrified. Some synaptosomes were found, but their quality was not good (the number of their SVs was very small).

Prep 13:

At the last preparation that we performed for this project, we used half of the neuronal cultures to isolate synaptosomes using the PI, while the other half was homogenized without it. Only two grids from the TKO + PI condition have been studied under the microscope. Although the vitrification was successful and biological material was observed, we could not find any synaptosomes.

In conclusion, despite all the modifications and optimizations that we made to our protocol, finding synaptosomes isolated from dissociated neuronal cultures turned out to be a very challenging task. There have been many microscope sessions where several grids were screened and no synaptosomes were detected. The synaptosomes were prepared from neuronal cultures at DIV 13 – 16 because the TKO neurons could not survive after DIV 16. Although synaptogenesis already started at DIV 10, it has been shown that the number of synapses is steeply increased during the third week *in vitro* (Grabrucker, Vaida, Bockmann, & Boeckers, 2009). We hypothesize that this is the main reason why the number of synaptosomes remains so low, after all the aforementioned changes that we made to our protocol. None of the preparations showed a great difference concerning the number of synaptosomes, however, we suggest that the protocol used in preps 8 – 11 is the one that could potentially give the best

results (details about that protocol at the Materials and Methods section), because it is very close to the protocol that has been used before to isolate synaptosomes from adult rodent brains. From all preparations combined we managed to record and analyze 4 WT synaptosomes, 5 TKO synaptosomes and 4 TKO – PI ones.

4.1.2 Preparation of dissociated neuronal cultures

Because our attempts of finding a reliable amount of synaptosomes from the neuronal cultures that were prepared in Bonn were unsuccessful, we decided to prepare some WT dissociated neuronal cultures at our Institute, in parallel. We wanted to see if we could improve the protocol to find synaptosomes from cultures more consistently.

The neuronal preparations were done along with Dr. Ulrike Laugks, Dr. Philipp Erdmann and Cristina Capitanio. We were plating cultures both directly on grids to be used for direct imaging and on petri dishes for synaptosome isolation.

We evaluated hippocampal synaptosomal preparations from both rat and mouse embryos. We found that the preparations were more successful when mouse hippocampi were used.

Initially, we did not coat carbon support film on grids with Laminin, but only with poly-Lysine. We found out that neurons were growing better on both poly-Lysine and Laminin coated grids.

Carbon film grids showed to be more prone to destruction during handling, so we decided to use SiO_2 ones which were more resistant to mechanical stress during washing and coating with Laminin. Also, the neurons were growing better on the SiO_2 film compared to the carbon one.

In our hands, placing a high number of hippocampi for digestion in a single falcon tube (14 – 16 hippocampi in 6ml medium) did not produce satisfactory results. We found that the optimal condition was reached by placing 8 hippocampi in 6ml of HBSS medium + Trypsin.

The rat hippocampi were minced using scalpel blades before digestion. When we switched to mouse hippocampi, we omitted that step, because mice hippocampi are smaller than the rat ones.

Initially, we did not include DNase I during digestion with Trypsin. As a result, there was an accumulation of DNA, which was holding the hippocampi together and would keep them floating in the medium. With the addition of DNase I, this accumulation stopped and the hippocampi were very quickly settling at the bottom of the falcon.

We also used Papain to digest the tissue instead of Trypsin. While Papain is known to have milder effects on the cells, we did not observe any difference in comparison with the cells from tissue digested with Trypsin. Digestion with trypsin required fewer steps than Papain, making the preparation time shorter, which benefited the viability of the neurons. Therefore, Trypsin was preferred.

Another alteration of the initial protocol involved adding Neuronal Plating Medium (NPM) (MEM with Earl's salts and L-glutamine, Invitrogen 31095-029; D-glucose (45% sol), Sigma G8769, 0.6%; FBS, Invitrogen 16000, 5%) after protease digestion, instead of immediately changing to neurobasal medium. We changed the medium to neurobasal after seeding cells.

Following the standard protocol, we filtered the cells immediately before counting, to avoid seeding clumps of cells in our cultures. However, it was observed that small clumps of cells (up to 5 cells) grew better than isolated neurons. Thus, we avoided filtering, unless we observed big chunks of cells (more than 6) during cell counting.

In the initial experiments, we were adding FuDR every time we exchanged the medium. In many cases, though, the day after the addition of FuDR, the neurons started dying. For that reason, we decided to add it only in case of very high glial cell proliferation.

After successfully managing to make dissociated neuronal cultures, we used the 10cm dishes for synaptosomal preparation. We scrapped cells from cultures at DIV 21. The protocol we used is described in the materials and methods section.

We have screened some grids containing synaptosomes obtained from one of the neuronal preparations. No synaptosomes were observed, although biological material was present and the grids were properly vitrified. This confirmed that it is quite difficult to purify synaptosomes from dissociated neuronal cultures for imaging by cryo-ET. There are more grids prepared from other preparations as well, which could be used to continue this project in future.

4.1.3 Visual assessment and detection of macromolecular complexes in cryo-electron tomograms

In order to decipher the role of RIM protein family in the organization of the release machinery at the presynaptic terminal, we analyzed cryo-tomograms of synaptosomes that lacked RIM proteins and compared the results with those obtained from the WT synaptosomes.

After reconstructing the acquired tomograms, they were visually assessed to select properly vitrified tomograms of healthy synaptosomes (see the Materials and Methods section) for further analysis. These contained uninterrupted, smooth membranes, pre- and postsynaptic terminals with well-defined synaptic cleft. Like in the previous publications from our group, many small spherical SVs were observed in the presynaptic terminals, together with some connectors and tethers. SVs could be observed very close to the AZ membrane, but the direct contact between them was rare.

As it was mentioned before, even in best preparations only a small number of synaptosomes were found. For the TKO condition, 5 tomograms were used for further analysis (11% from all the acquired tomograms). For the WT, 4 tomograms were analyzed (25% of the total tomograms acquired). Finally, 4 tomograms were analyzed further for the TKO without PI condition (50% from all the tomograms acquired).

In order to quantitatively analyze the selected tomograms, large synaptic structures were segmented in a manual or semi-manual fashion. These included plasma membranes, SVs, as well as mitochondria, microtubules and vesicles of other shapes and sizes. SV membrane-attached macromolecular complexes, tethers and connectors were detected automatically, using the hierarchical connectivity algorithm as implemented in the Pyto package (Lučić et al., 2016). The results of the quantitative analysis of these complexes and their statistical assessment are presented in the sections that follow.

4.1.4 SV distribution

The previous work from our group has shown that SVs possess distinct organization within the presynaptic terminal. It has been shown that in healthy synapses the SV concentration had a

maximum in the proximal zone (0 – 45nm from the AZ), in the intermediate zone (45 – 75nm) the concentration had a minimum and in the distal zones (75 – 150nm and 150 – 250nm) the concentration was increased, again (figure 13D). For that analysis, the part of the interior of the presynaptic membrane occupied by SVs was divided into 1-pixel-thick layers according to the distance from the AZ. The fraction of the cytoplasmic volume that was occupied by SVs was, therefore, measured excluding, at the same time, other organelles that might be present, such as mitochondria, microtubules, lysosomes etc. (Fernández-Busnadiego et al., 2010).

The distribution of the SVs within the presynaptic terminal in the WT synaptosomes used in this project, was similar to these previous results: SV concentration showed a maximum close to the AZ, followed by a region of lower concentration. However, the SV distribution in the RIM TKO synaptosomes was different: there was no SV distribution maximum in the proximal zone. In some cases, there was a peak located further than 50nm from the presynaptic membrane (figure 15).

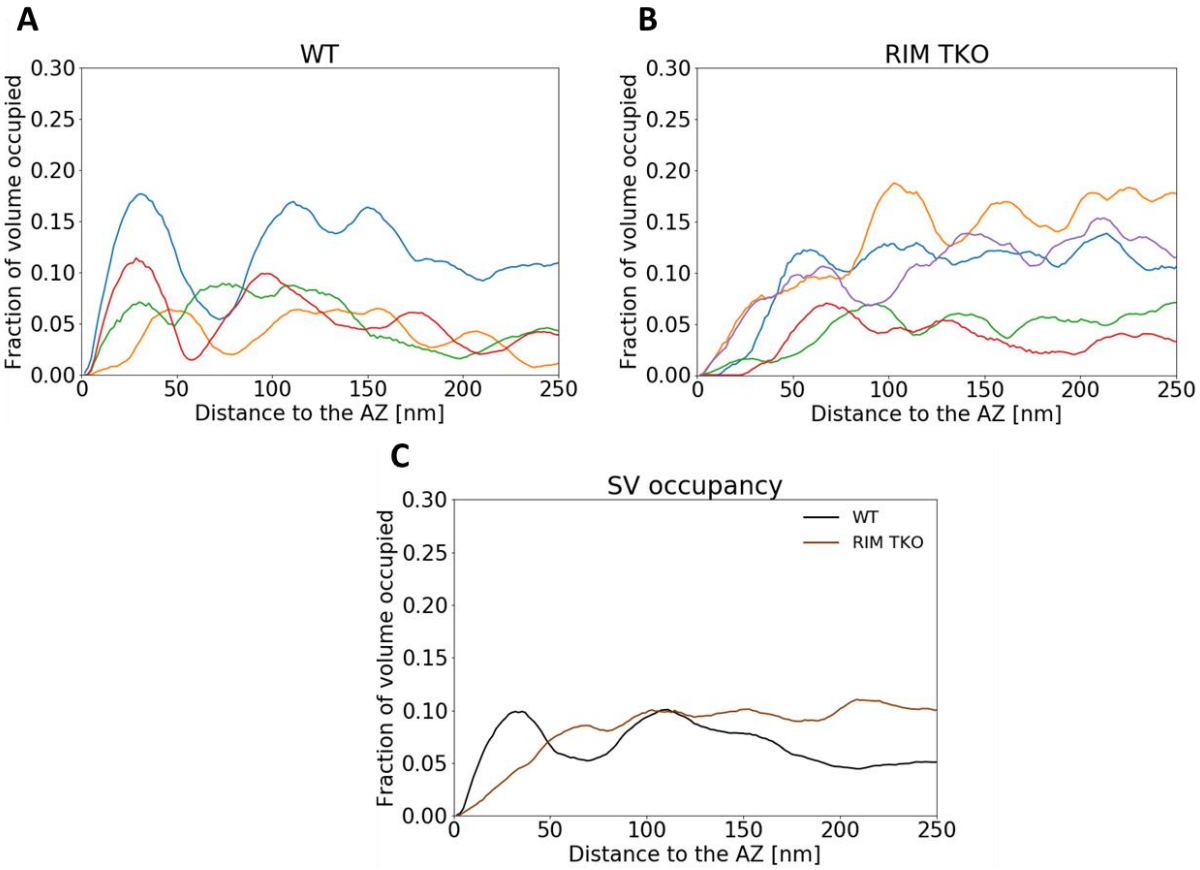

Figure 15: SV occupancy of A: WT synaptosomes, B: RIM TKO synaptosomes. C: Mean SV occupancy of WT and RIM TKO. The difference in SV distribution between the 2 conditions is clearly depicted.

Moreover, the number of proximal SVs per synapse in the TKO synaptosomes was significantly reduced compared to the WT ones (TKO: 2, +/- 0.63, WT: 8.5, +/- 2.72, $P < 0.05$, t test) (figure 16).

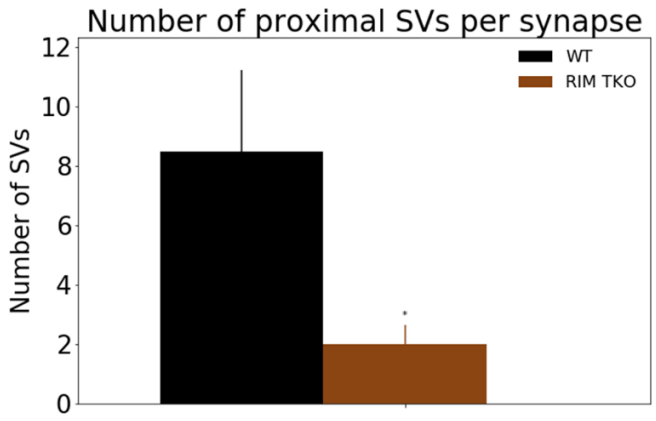

Figure 16: Number of proximal SVs per synapse

As mentioned before, RIM1α KO synaptosomes were divided into 2 classes based on SV distribution: an aligned one, which is similar to the WT synapses, and the altered one, which shows severe deficits (Fernández-Busnadiego et al., 2013). The SV distribution of the TKO synaptosomes resembled the one from the altered class of the RIM1α KO synaptosomes, because in both cases the peak in SV concentration at the proximal zone is missing (figure 17).

These results argue that RIM protein family plays a major role in the localization of the SVs in the proximal region.

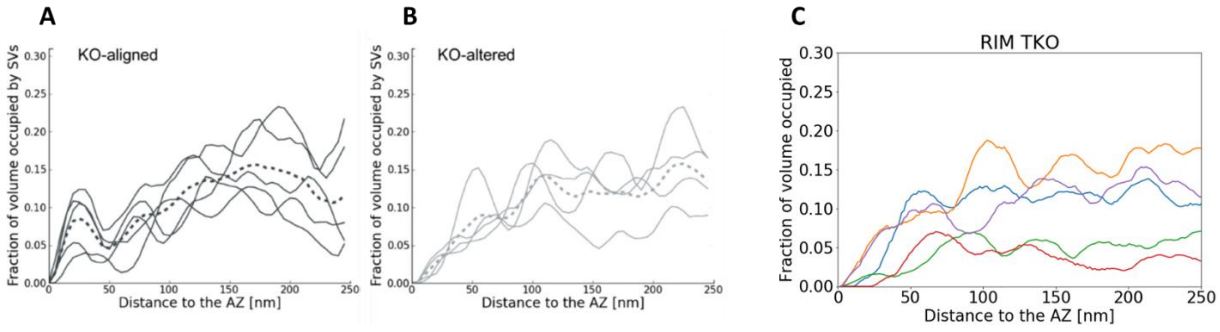

Figure 17: Division of the RIM1α synaptosomes based on the SV distribution in A: KO-aligned and B: KO-altered class (Fernández-Busnadiego et al., 2013). C: SV occupancy of RIM TKO synaptosomes. Its SV distribution, resembles the one of the KO-altered class.

4.1.5 Analysis of tethers

The mean number of tethers per synapse in the TKO synaptosomes was significantly smaller than the WT ones (TKO: 7.80, +/- 2.42, WT: 47.00, +/- 18.53, $P < 0.05$, t test) (figure 18A).

However, there was no difference concerning the length of the tethers between TKO and WT synaptosomes (TKO: 11.99nm, +/- 1.63, WT: 11.28nm, +/- 0.73, Kruskal test). We note that in both cases the mean tether length was above 10nm (figure 18B, 18C). Furthermore, the distribution of tether lengths was similar in TKO and WT synaptosomes. These results show that RIM proteins do not affect tether length and suggest that tethers are not composed of RIM proteins.

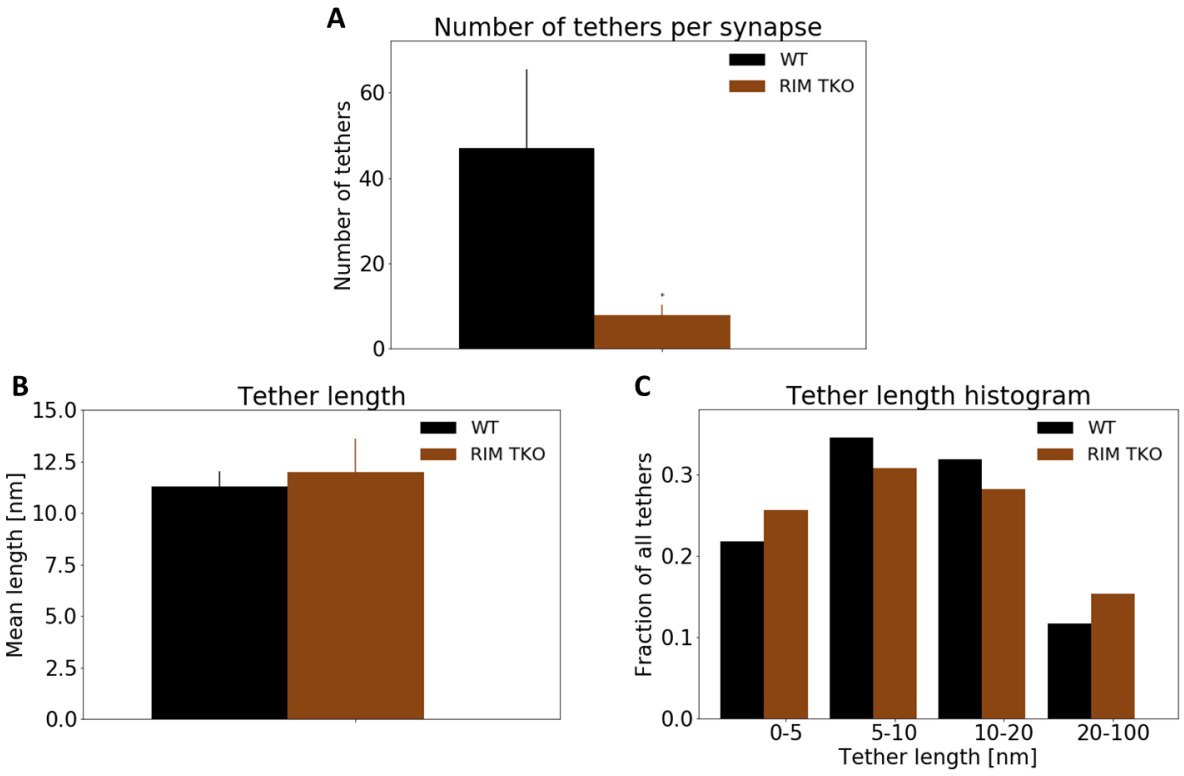

Figure 18: A: Number of tethers per synapse, B: Mean tether length, C: Histogram of tether length

4.1.6 SV tethering

The number of proximal SVs that are tethered, per unit AZ area, was more than two times smaller in the TKO synaptosomes, but this difference was not significant because of large variability between synapses and the low number of observations (TKO: 16.8, +/- 6.79, WT: 39.28, +/- 13.83, t test) (figure 19A). However, this result can be explained by the smaller number of proximal SVs in the TKO synaptosomes.

There were no differences between TKO and WT synaptosomes regarding the fraction of the proximal SVs that are tethered (TKO: 0.9, n=10, WT: 0.882, n=34, chi^2 test) (figure 19B). Moreover, there was no significant difference in the number of tethers per SV (TKO: 3.8, +/- 1.19, WT: 5.44, +/- 0.67, Kruskal test) (figure 19C). Both in WT and TKO synaptosomes, the majority of SVs had more than 2 tethers (figure 19D). These results further argue that RIM family does not have a function downstream of tether formation.

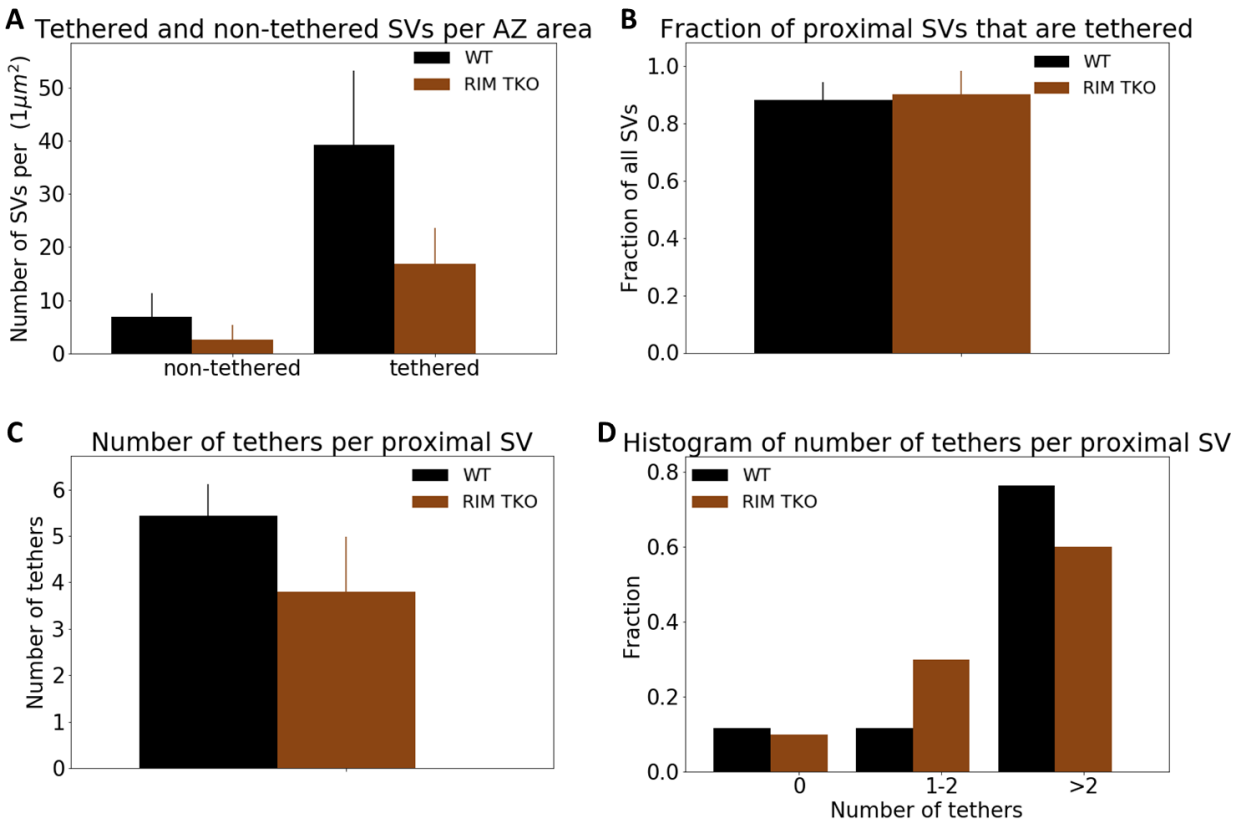

Figure 19: A: Number of tethered and non-tethered SVs per AZ area. B: Fraction of proximal SVs that are tethered. C: Number of tethers per proximal SV. D: Histogram of number of tethers per proximal SV

4.1.7 TKO synaptosomes without PI

As mentioned above, for the RIM1α KO project no protease inhibitor cocktail (PI) was present in the homogenization buffer during synaptosomal preparation. In order to compare these results with our data, we decided to make a synaptosomal preparation without PI. We were able to find some synaptosomes from this preparation (n=4), but their quality was not good. The number of SVs in RIM TKO without PI synapses was very small (figure 20A) and only one synaptosome had SVs at the proximal level, which precluded the tethering analysis (figure 20B). While it is difficult to interpret this data because of the low quality of the preparation, this data

is consistent with our RIM TKO data with PI (figure 15B). It is reasonable to conclude that without PI, RIM TKO synapses are more disturbed than those purified in the presence of PI.

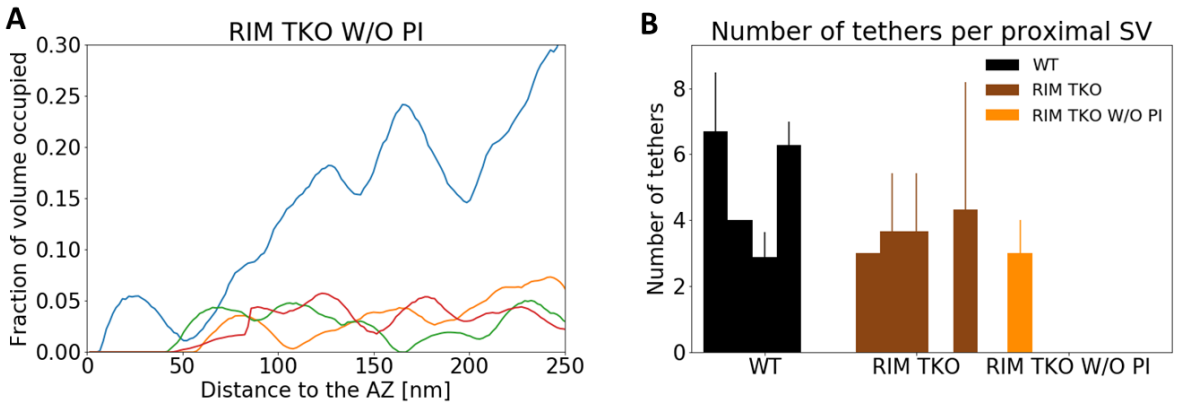

Figure 20: A: SV occupancy of RIM TKO synaptosomes prepared without PI cocktail. The number of SVs was, in general, very small. B: Number of tethers per proximal SV. We can see that only one RIM TKO w/o PI synaptosome had proximal SVs.

4.1.8 Conclusion

The lack of all RIM isoforms alters the SV distribution at the presynaptic terminal by reducing the SV concentration at the proximal level. This reduction leads us to the argument that RIM is responsible for bringing the SVs to the proximal region of the AZ. The SV distribution of RIM TKO synaptosomes resembles the one from the RIM1α KO altered synaptosomes (lack of the proximal concentration peak). These results suggest that the partial compensation of the proximal concentration peak that was observed in RIM1α KO aligned synaptosomes is caused by RIM isoforms other than RIM1α. This confirms our hypothesis that there are other isoforms that have similar actions like RIM1α in RIM1α independent synapses.

The number of proximal SVs was further decreased in the RIM TKO synaptosomes without PI. However, these results should be interpreted with care because it is likely that there was a substantial protein degradation in these synaptosomes.

While the number of tethers was reduced in RIM TKO synapses, the remaining tethers were not significantly different from the WT tethers. This argues that tethers are not composed of RIM proteins and that most likely the function of tethers is to bring SVs to the proximal zone where they can get tethered by other proteins.

Unfortunately, the number of synaptosomes that we obtained was very small, due to the preparation issues that we had. In general, synaptosomes isolated from dissociated cultures were of low quality. That drastically decreased the yield and likely contributed to a large variability, which together made interpretation of the results very challenging. Finally, the preparation without the PI had a very low quality and this does not allow us to make reliable conclusions.

4.2 Structural role of Munc13 in synaptic release

In this project, we were interested in studying the roles of Munc13 in the organization of the tethers and SV progression towards release, by comparing synaptosomes lacking all isoforms of the Munc13 protein family and WT synaptosomes.

4.2.1 Protocol optimization for synaptosome preparation from organotypic brain slice cultures

Similar to the RIM KO animals, the complete genetic ablation of all Munc13 isoforms is postnatally lethal (Siksou et al., 2009). However, our collaborators generated homozygous Munc13-1/2 DKO (Munc13 -/- -/-) embryos by interbreeding homozygous Munc13-2 KO and heterozygous Munc13-1 KO mice (Varoqueaux et al., 2002). In addition, Munc13 +/- +/- (DHET, littermate controls of the DKO mice) slices and WT slices were obtained. Because Munc13-1/2 DKO and DHET slices were obtained from E18 mice and had mixed background, and WT slices from C57/N mice at P0, strain and age differences between Munc13-1/2 DKO and WT cannot be excluded.

The hippocampi of the aforementioned embryonic mouse brains were cut into thin slices (around 4 per hippocampus) and the slices were grown in culture for 28 – 30 DIV. The breeding and crossing of mice, and the preparation of organotypic hippocampal slice cultures were performed by our collaborators, Dr. Cordelia Imig and Dr. Benjamin Cooper, at Prof. Nils Brose's lab at Max Planck Institute of Experimental Medicine in Göttingen. Hippocampal slices were rinsed with Normal Tyrode's buffer before being scooped with a brush and put in a glass tube containing the homogenization buffer (50µl of buffer per slice). We found that at least six slices were needed to obtain enough material for plunge freezing. After homogenization and the low and medium centrifugation (see detailed final protocol in the Materials and Methods section), three different protocols were employed and compared:

1. Plunge-freezing the crude P2 fraction. The pellet resulting from the medium-speed centrifugation was resuspended in Ca^{2+} free HBM to the desired concentration (0.3 – 0,5mg/ml using a spectrophotometer) and was used for plunging. Cryo-EM observations showed properly vitrified grids that contained abundant healthy biological material. There were many synaptosomes present on each grid and it was very easy to find them.
2. Percoll gradient for purifying synaptosomes, without removing Percoll. 300µl of the crude P2 fraction of synaptosomal solution were added in a 13x51 (thick wall) tube (Tube, Thickwall, Polyallomer, 3.5 mL, 13 x 51 mm, Catalog Number 349623, Beckman Coulter GmbH, Krefeld, Germany). The tubes contained the Percoll gradient (3%, 10% and 23% in 0.32M sucrose, 800µl each) and were centrifuged at 25000g for 4 min. Three bands of material were visible and the interface between 10% and 23% Percoll was taken. It was diluted with HBM + $CaCl_2$ (2x) and H_2O (10% synaptosomal solution from the Percoll gradient, 40% H_2O and 50% HBM + $CaCl_2$ (2x)) and this solution was used for plunging. Cryo-EM investigations showed that some grids contained a thick layer of material and were barely transparent to the electron beam, while others were empty, with no biological material, and, thus, no synaptosomes present.
3. Percoll gradient for purifying synaptosomes followed by Percoll removal. Similar to the previous protocol, in this case 500µl of synaptosomal material was added on the Percoll gradient. Importantly, the interface between 10% and 23% of the gradient was diluted

with Ca^{2+} free HBM and was centrifuged at 22000g for 10min to remove Percoll. There was a very small amount of pellet, barely visible, so, the supernatant was removed very carefully. The pellet was resuspended with HBM + $CaCl_2$ (1x) and was used for plunging. Although the material on the grids was very sparse, there were synaptosomes present. Their number was similar to the one from the grids in which the crude P2 fraction of synaptosomal solution was used.

We decided to continue with the first protocol (plunge freezing the crude fraction), because, similarly to the third protocol, synaptosomes were abundant on grids, and omitting Percoll gradient step made the preparation time shorter, which benefited the viability of the synaptosomes. The details of this protocol can be found at the Materials and Methods section.

4.2.2 Visual assessment and detection of macromolecular complexes in cryo-electron tomograms

Just like in the RIM project, the tomograms were visually assessed after being reconstructed. Only properly vitrified tomograms of healthy synaptosomes with uninterrupted, smooth membranes, pre- and postsynaptic terminals with well-defined synaptic cleft, spherical SVs and visible tethers and connectors were used for further analysis.

For the DKO condition, 13 tomograms were analyzed (46% from all the acquired tomograms). For the WT, 13 tomograms were used for further analysis, as well (33% of the total tomograms acquired). Finally, 8 tomograms were analyzed further for the DHET (47% from all the tomograms acquired).

In order to quantitatively analyze the selected tomograms, large synaptic structures were segmented in a manual or semi-manual fashion. These included plasma membranes, SVs, as well as mitochondria, microtubules and vesicles of other shapes and sizes. SV membrane-attached macromolecular complexes, tethers and connectors were detected automatically, using the hierarchical connectivity algorithm as implemented in the Pyto package (Lučić et al., 2016). The results of the quantitative analysis of these complexes and their statistical assessment are presented in the sections that follow.

4.2.3 SV distribution

The distribution of the SVs within the presynaptic terminal in DKO, WT and DHET synaptosomes showed increased SV concentration in the region proximal to the AZ. This shows that removal of Munc13 did not cause large rearrangements of SVs (figure 21).

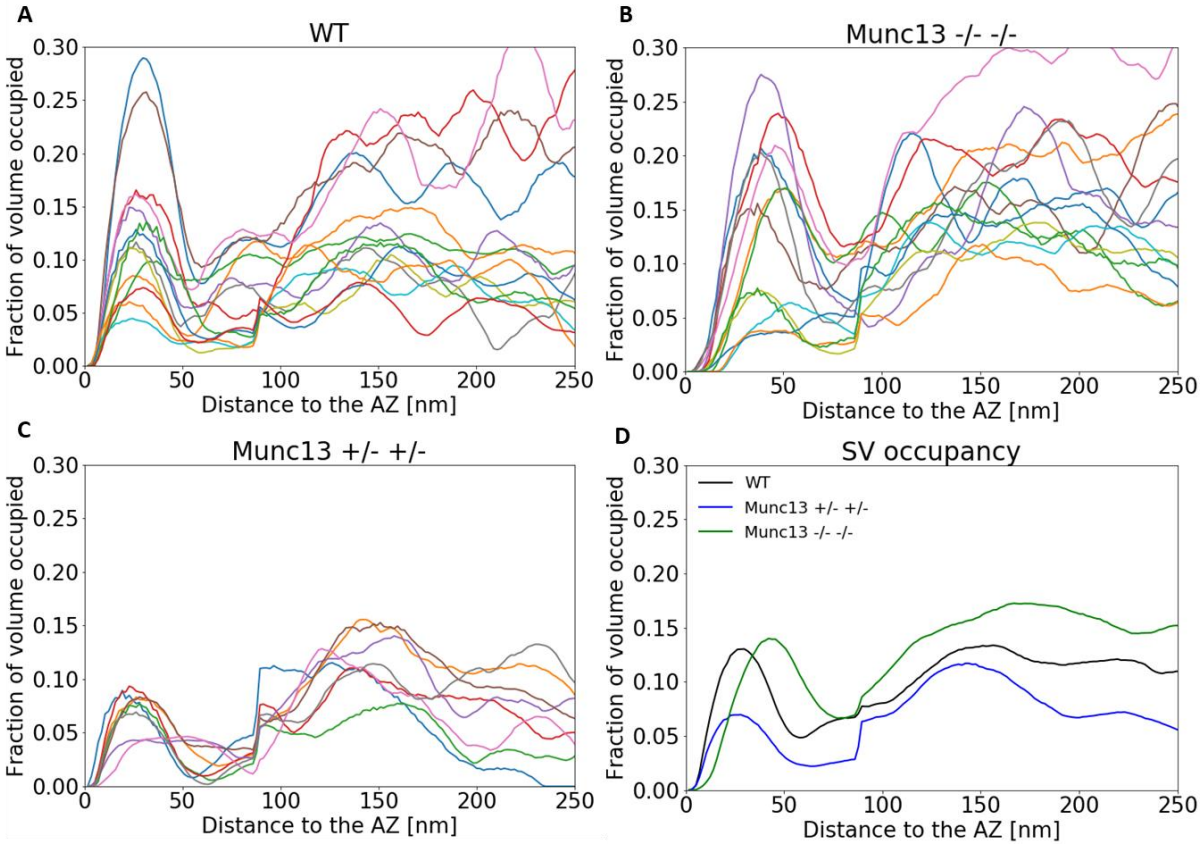

Figure 21: SV occupancy of A: WT, B: Munc13 DKO, and C: Munc13 DHET synaptosomes. D: Mean SV occupancy of WT, Munc13 DKO and Munc13 DHET.

The concentration of SVs in the region proximal to the AZ, as measured by the fraction of cytoplasmic volume occupied by SVs, did not differ between DKO and WT synaptosomes (DKO: 0.08 +/- 0.01, n=13, WT: 0.09 +/- 0.01, n=14 t test) (figure 22A). Surprisingly, it was significantly reduced in the DHET synaptosomes in respect to WT (DHET: 0.05 +/- 0.00, n=8, $P < 0.01$, t test).

Furthermore, the same pattern was observed at intermediate and distal zones. There was no statistically significant difference concerning the AZ surface area in all of the conditions studied (DKO: 0.15µm^2 +/- 0.03, n=13, DHET: 0.17 µm^2 +/- 0.02, n=8, WT: 0.14 µm^2 +/- 0.02, n=14, t test), so, the reduced fraction of SVs in DHET was not due to smaller synapses (figure 22B). These synapses have been used as controls both in electrophysiological (Man et al., 2015) and in cryo-ET studies (Maus et al., 2020) and no differences have been found compared to WT synapses. Altogether, the difference in SV concentrations between DHET and WT synapses might be caused by the differences in age and genetic background between WT and DHET mice, or by other factors that control the overall number of SV at a synapse but do not influence their localization.

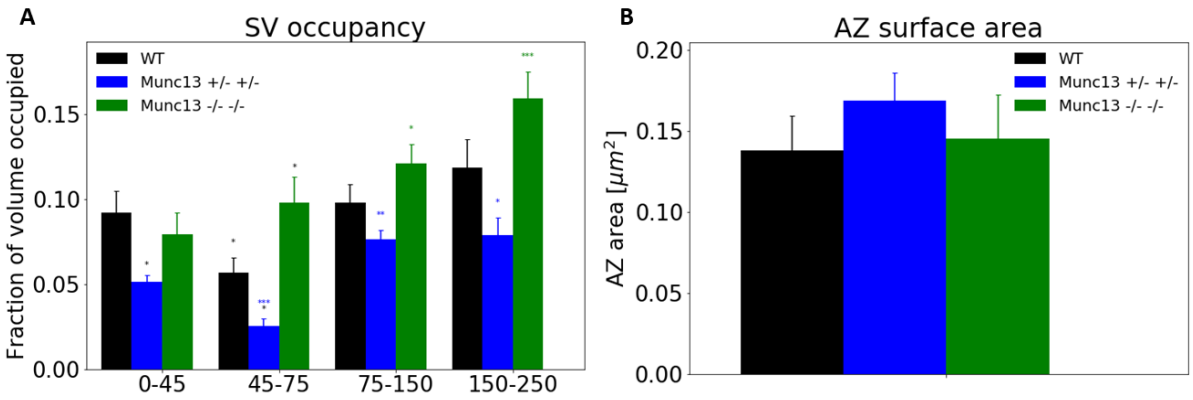

Figure 22: A: SV occupancy of WT, Munc13 DKO and Munc13 DHET, B: AZ surface area.

The minimum distance of proximal SVs to the AZ was significantly increased in the DKO synaptosomes compared to both the WT and the DHET ones (DKO: 14.33nm +/- 0.43, WT: 8.32nm +/- 0.32, DHET: 8.45 +/- 0.61, P < 0.001, t test) (figure 23A). There was a striking difference in the distribution of SVs. Namely, the SV distribution in the DKO synaptosomes was significantly different compared to the WT one (DKO: n=98, chi^2=97.9102, P < 0.001, chi^2 test) (figure 23B). More specifically, while 80% of SVs in the WT and DHET synaptosomes were located closer than 10nm from the AZ (DKO: 0.16 +/- 0.04, WT: 0.80 +/- 0.04, DHET: 0.76 +/- 0.07, P < 0.001, Kruskal test) (figure 23C), approximately 70% of the SVs in the DKO synaptosomes were located between

10nm and 20nm from the AZ (DKO: 0.72 +/- 0.06, WT: 0.18 +/- 0.04, DHET: 0.17 +/- 0.08, P < 0.001, Kruskal test) (figure 23D).

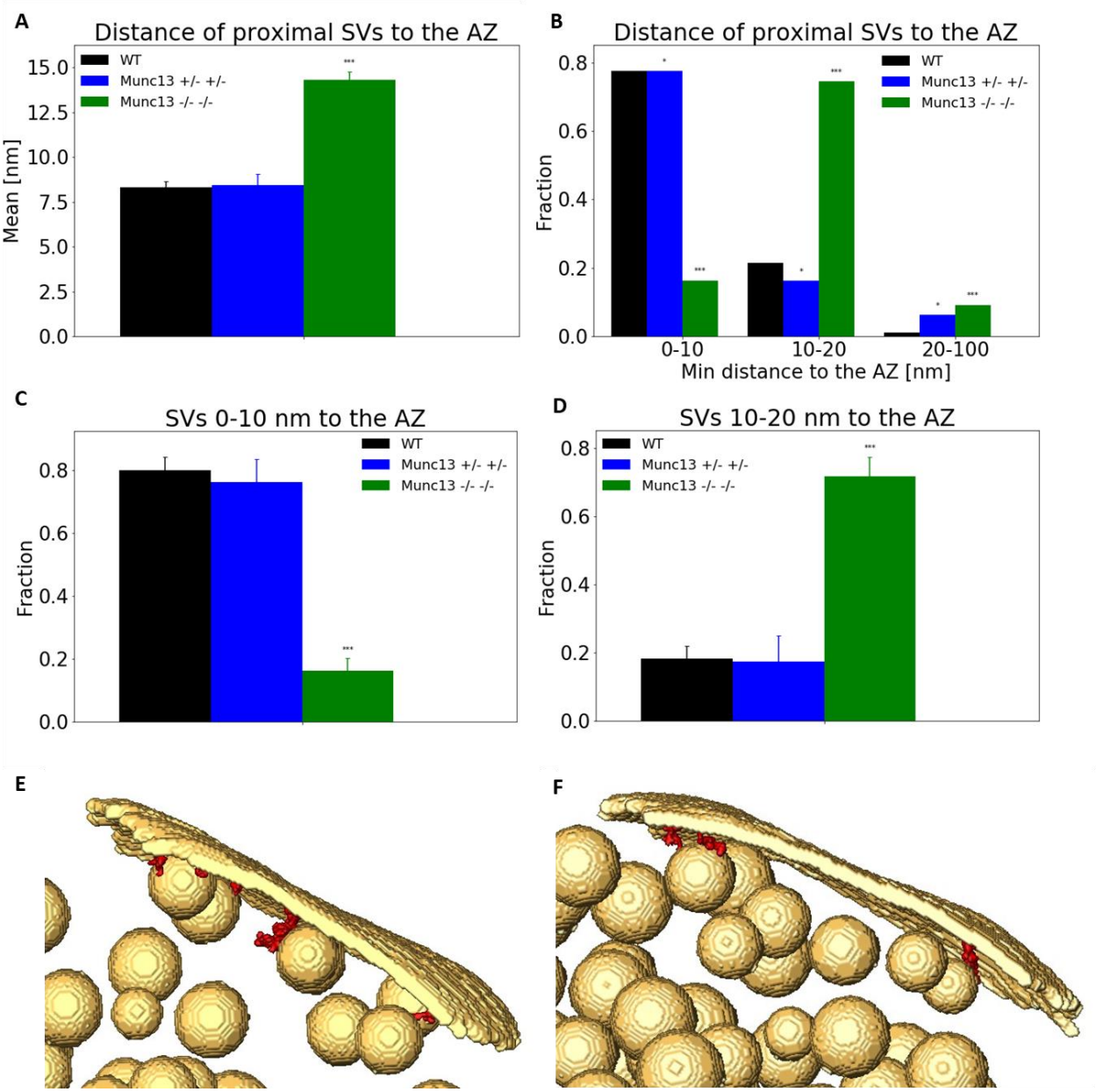

Figure 23: A: Mean distance of proximal SVs to the AZ, B: Histogram of the distance of proximal SVs to the AZ, C: SVs located between 0 and 10nm from the AZ, D: SVs located between 10 and 20nm from the AZ. 3D segmentation of SVs and presynaptic membrane (yellow) of E: a WT and F:

a Munc13 DKO synaptosome. The proximal SVs are located further away from the AZ in the Munc13 DKO synaptosome compared to the WT one.

Our data argue that overall Munc13 does not contribute to the accumulation of SVs in the proximal zone. It is necessary for localizing proximal SVs closer than 10nm to the AZ.

4.2.4 Tether number and morphology

Overall, the number of tethers per AZ area was significantly reduced in DKO synaptosomes compared to the WT and DHET ones (DKO: 84.78 +/- 19.46, WT: 283.34 +/- 35.80, DHET: 200.90 +/- 30.56, $P < 0.001$, t test) (figure 24A). Analysis of the mean tether length, showed that DKO tethers were 40% longer compared to WT and DHET (DKO: 20.89nm +/- 1.17, WT: 14.00nm +/- 0.38, DHET: 13.10nm +/- 0.50, $P < 0.001$, Kruskal test) (figure 24B).

Further analysis of tethers separated in classes based on their length showed that, in general, the length was significantly different in the DKO synaptosomes compared to the WT and DHET ones (DKO: n=117, $chi^2=51.8847$, $P < 0.001$, chi^2 test) (figure 24C). More specifically, 40% of tethers in WT and 45% in DHET were between 0 and 10nm long, compared to 15% of the DKO tethers (DKO: 0.15 +/- 0.05, WT: 0.42 +/- 0.03, DHET: 0.44 +/- 0.07, $P < 0.001$, Kruskal test) (figure 24D). For tethers between 10nm and 20nm, the results were not significant: 30% of DKO, 40% of WT and 35% of DHET tethers were that long (DKO: 0.32 +/- 0.05, WT: 0.40 +/- 0.03, DHET: 0.34 +/- 0.04, Kruskal test) (figure 24E). While more than 50% of the DKO tethers were longer than 20nm, only 20% of WT and DHET were of that length and these differences were highly significant (DKO: 0.54 +/- 0.06, WT: 0.18 +/- 0.02, DHET: 0.22 +/- 0.05, $P < 0.001$, Kruskal test) (figure 24F).

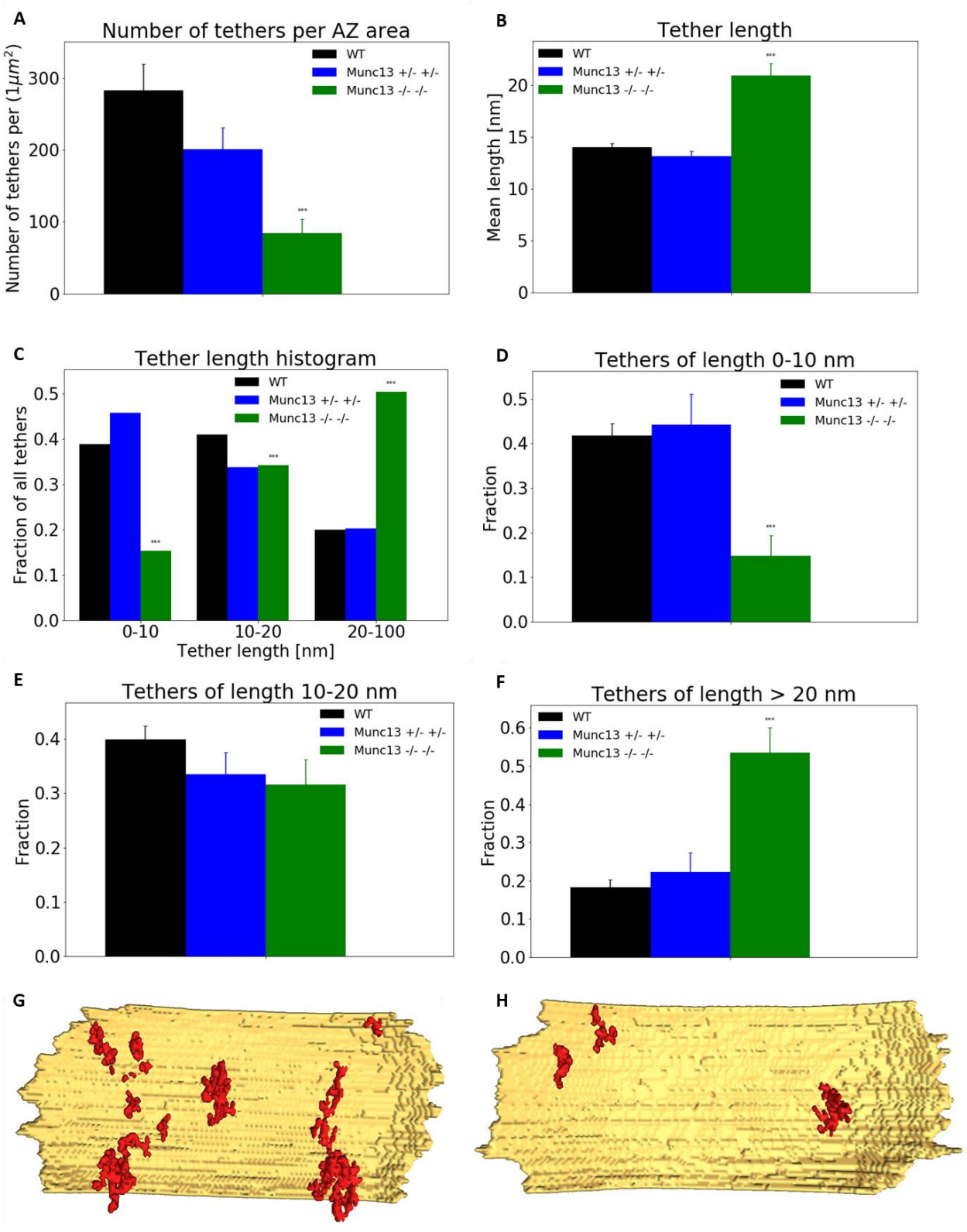

Figure 24: A: Number of tethers per AZ area, B: Mean tether length, C: Histogram of the fraction of tether length, D: Tethers between 0 and 10nm, E: Tethers between 10 and 20nm, F: Tethers

longer than 20nm. 3D segmentation of the presynaptic membrane (yellow) and tethers (red) of G: a WT and H: a Munc13 DKO synaptosome. The reduced number of tethers in Munc13 DKO synaptosomes is shown here.

To conclude, lack of Munc13 severely impairs the formation of tethers, especially the ones shorter than 10nm. The existence of these short tethers might be the reason why SVs are closer to the AZ in the presence of Munc13. This further supports our hypothesis that Munc13 is responsible for bringing the SVs closer than 10nm to the AZ.

4.2.5 SV tethering

The fraction of proximal SVs that are tethered was significantly lower in the DKO synaptosomes compared to the WT and DHET ones (DKO: 0.571, n=98, chi^2=24.3950, DHET: 0.850, n=80, chi^2=0.0367, WT: 0.841, n=182, $P < 0.001$, chi^2 test) (figure 25A). Accordingly, the number of tethered proximal SVs is reduced significantly in the DKO synaptosomes compared to the WT ones (DKO: 39.54nm +/- 9.24, WT: 78.20nm +/- 9.37, $P < 0.01$, t test) (figure 25B). Concerning the number of tethers per proximal SV, almost 90% of SVs in DKO synaptosomes did not have any, or had up to 2 tethers compared to 40% of the SVs in WT and DHET synaptosomes. On the other hand, the largest number of SVs in WT and DHET SVs had 3 to 4 tethers (32%), but there were also SVs that had even more than 7 tethers (10%) (figure 25C).

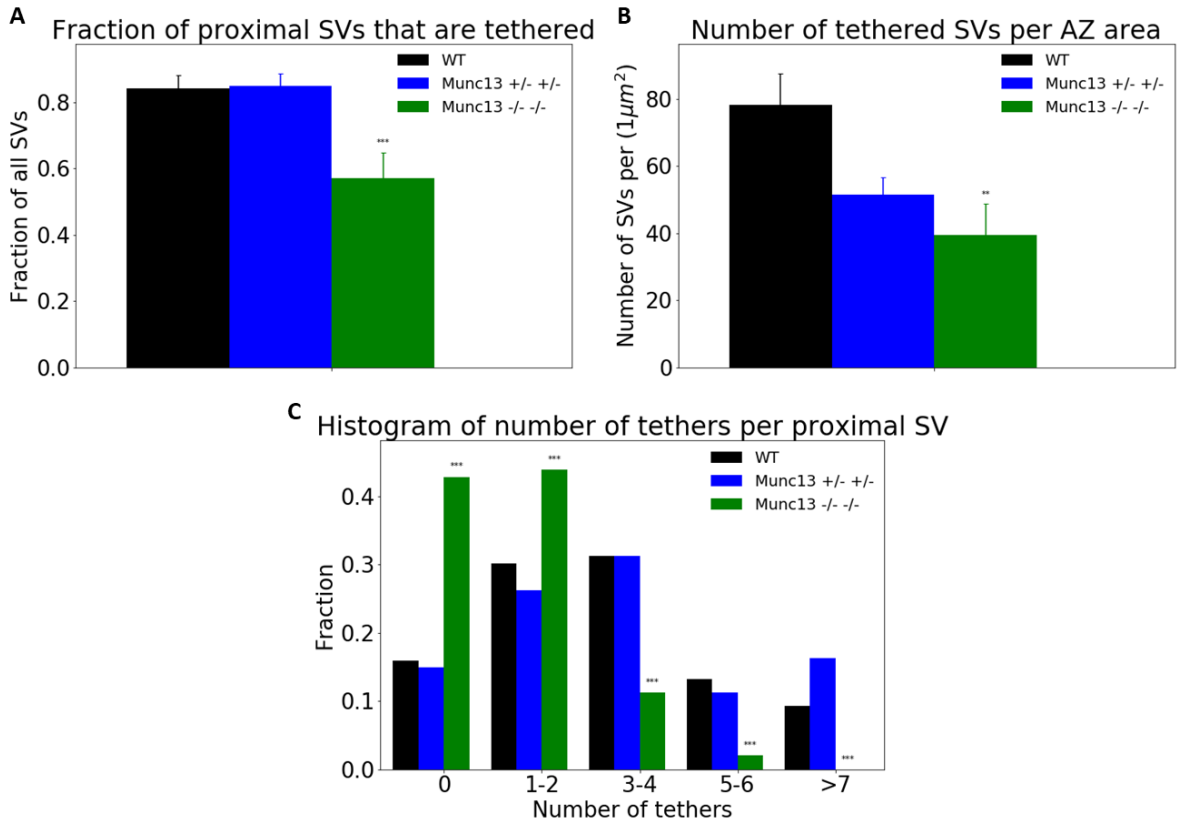

Figure 25: A: Fraction of proximal SVs that are tethered, B: Number of tethered SVs per AZ area, C: Histogram of number of tethers per proximal SV.

In conclusion, lack of Munc13 results in SVs that have at most few tethers. Our group has previously defined the structural readily releasable pool (RRP) to comprise multiply tethered SVs and showed evidence that structural RRP corresponds to the physiologically determined RRP (Fernández-Busnadiego et al., 2010). Therefore, our data shows that Munc13 is necessary for the structural RRP. Considering that previous studies showed that Munc13 is necessary for priming (formation of RRP) (Varoqueaux et al., 2002; Imig et al., 2014), our data further support the structural identification of primed SVs.

4.3 Activation of Munc13 by PDBu

Results from studies of Dr. Ulrike Laugks show that PDBu treated neocortical synaptosomes have SVs with significantly smaller distance to the AZ compared to the WT untreated ones. Also, the number of tethers per AZ unit and per SV is significantly higher in the PDBu treated synaptosomes. To ensure that these effects were a result of the activation of Munc13 by PDBu, a pharmacological approach was used: application of antagonists that blocked this activation reverted the results to the values obtained for the untreated samples (Laugks, 2018).

In the current project, we used a genetic approach to study the effects of PDBu on Munc13: at first, WT synaptosomes were treated with PDBu, in order to replicate the results observed previously. Then, Munc13 DKO synaptosomes were treated with PDBu, to show whether the observed effects of PDBu are mediated by Munc13. For WT + PDBu condition, 8 tomograms were analyzed (57% from the tomograms acquired). For the DKO + PDBu, 7 tomograms were used for further analysis (47% of all the tomograms acquired).

Concerning the SV distribution, in WT synaptosomes treated with PDBu the fraction of proximal SVs that are closer than 5nm to the AZ was significantly bigger compared to the untreated WT synaptosomes (WT + PDBu: n = 59, $chi^2 = 7.2352$, $P < 0.01$, chi^2 test) (figure 26A), although the mean distance from the AZ showed no difference between WT treated with PDBu and WT untreated synaptosomes (WT PDBu: 7.69nm +/- 0.68, n = 59, WT: 8.32nm +/- 0.32, n = 182, t test) (figure 26B).

The mean tether length was significantly smaller in WT PDBu synaptosomes compared to untreated ones (WT + PDBu: 11.93nm +/- 0.60, n = 200, WT: 14.00nm +/- 0.38, n = 555, $P < 0.001$; Kruskal test) (figure 26C). Also, there were significantly more tethers shorter than 10nm in PDBu treated synaptosomes, compared to the untreated ones (WT + PDBu: 0.55 +/- 0.02, WT: 0.42 +/- 0.03, $P < 0.01$, Kruskal test) (figure 26D). We found no differences between WT PDBu synaptosomes and untreated ones, concerning the fraction of proximal SVs that are tethered and the number of tethers per SV (WT + PDBu: n = 59, $chi^2 = 4.7286$, $P = 0.3163$, chi^2 test) (figure 26E).

Importantly, comparing DKO treated with PDBu and untreated DKO synaptosomes, gave no differences in all of the aforementioned measurements. This strongly argues that Munc13 is necessary for the observed effects of PDBu.

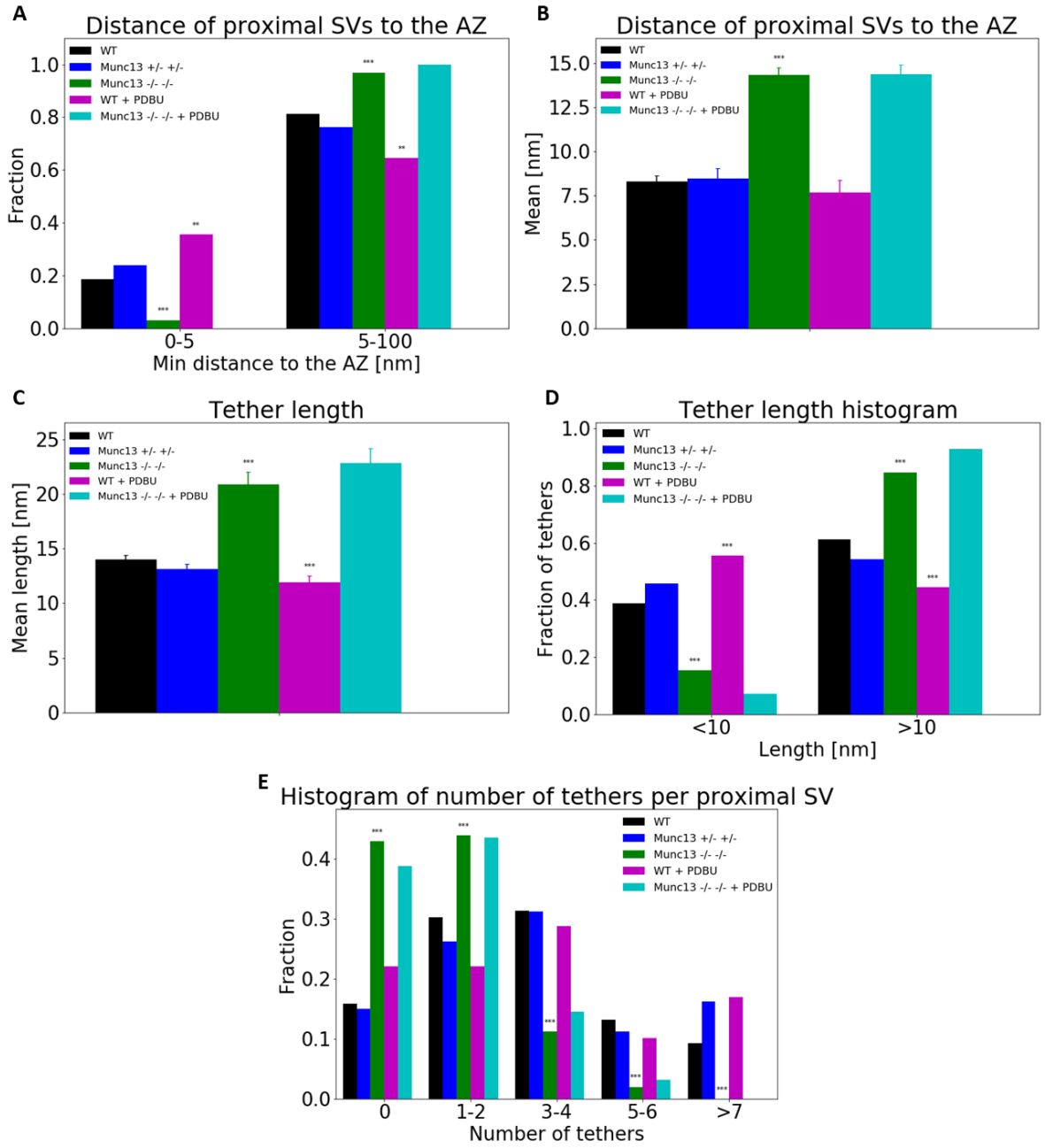

Figure 26: A: Proximal SVs closer and further than 5nm from the AZ, B: Mean distance of proximal SVs to the AZ, C: Mean tether length, D: Histogram of tethers shorter and longer than 10nm, E: Histogram of number of tethers per proximal SV.

The main conclusion from these experiments is that the presence of PDBu increases the number of proximal SVs closer than 5nm from the presynaptic membrane, which agrees with previous results from our group. Also, it decreases the tether length, resulting in more tethers shorter than 10nm. On the other hand, we failed to confirm that PDBu treated synaptosomes have more tethers per SV compared to the untreated ones. These differences might be explained by differences in the methods between the two projects. Namely, the pharmacological approach was done in synaptosomes from the neocortex of adult rats, while the genetic approach in synaptosomes from organotypic hippocampal slices from mice embryos. Perhaps this is one reason why we managed to confirm some but not all of the results of the pharmacological approach.

4.4 Cryo-ET of synapses lacking SNAP25

We already showed that the activation of Munc13 by PDBu results in SV localization closer to the AZ and increases the fraction of tethers shorter than 10 nm. We hypothesize that, at least some of these short tethers depend on the SNARE proteins. In order to validate this hypothesis, we analyzed presynaptic cytomatrix of SNAP25 -/- synaptosomes.

Because SNAP25 KO is perinatally lethal in homozygous mice (Jeans et al., 2007), we crossed SNAP25 heterozygous knockout mice to get the homozygous knockouts. We made organotypic hippocampal slice cultures from these mice and purified synaptosomes in the same way as for the Munc13 project. The breeding and crossing of mice, and the preparation of organotypic hippocampal slice cultures were performed, once again, by Dr. Cordelia Imig and Dr. Benjamin Cooper at Nils Brose's lab at Max Planck Institute of Experimental Medicine in Göttingen. For the KO condition. 14 tomograms were analyzed (42% from the tomograms acquired for this condition). For the WT, 9 tomograms were used for further analysis (37% of all tomograms acquired).

The SV distribution within the presynaptic terminal and the number of proximal SVs between the SNAP25 KO synaptosomes and the WT ones showed no differences (KO: 0.07 +/- 0.01, WT: 0.06 +/- 0.01, t test) (figures 27A, 27B). The distance of proximal SVs to the AZ was increased significantly in SNAP25 KO synaptosomes (KO: 9.82nm +/- 0.29, n = 147, WT: 8.16nm +/- 0.48, n = 110, $P < 0.01$, t test) (figure 27C). More specifically, there were fewer SNAP25 KO proximal SVs closer than 5nm to the AZ, resulting in a significant decrease of the fraction of these SVs in comparison to the WT (KO: 0.07 +/- 0.03, WT: 0.23 +/- 0.07, $P < 0.05$, Kruskal test) (figure 27D). There was no significant difference concerning the fraction of proximal SVs located between 5nm and 10nm to the AZ (KO: 0.43 +/- 0.06, WT: 0.55 +/- 0.08, $P = 0.2435$, Kruskal test) (figure 27E).

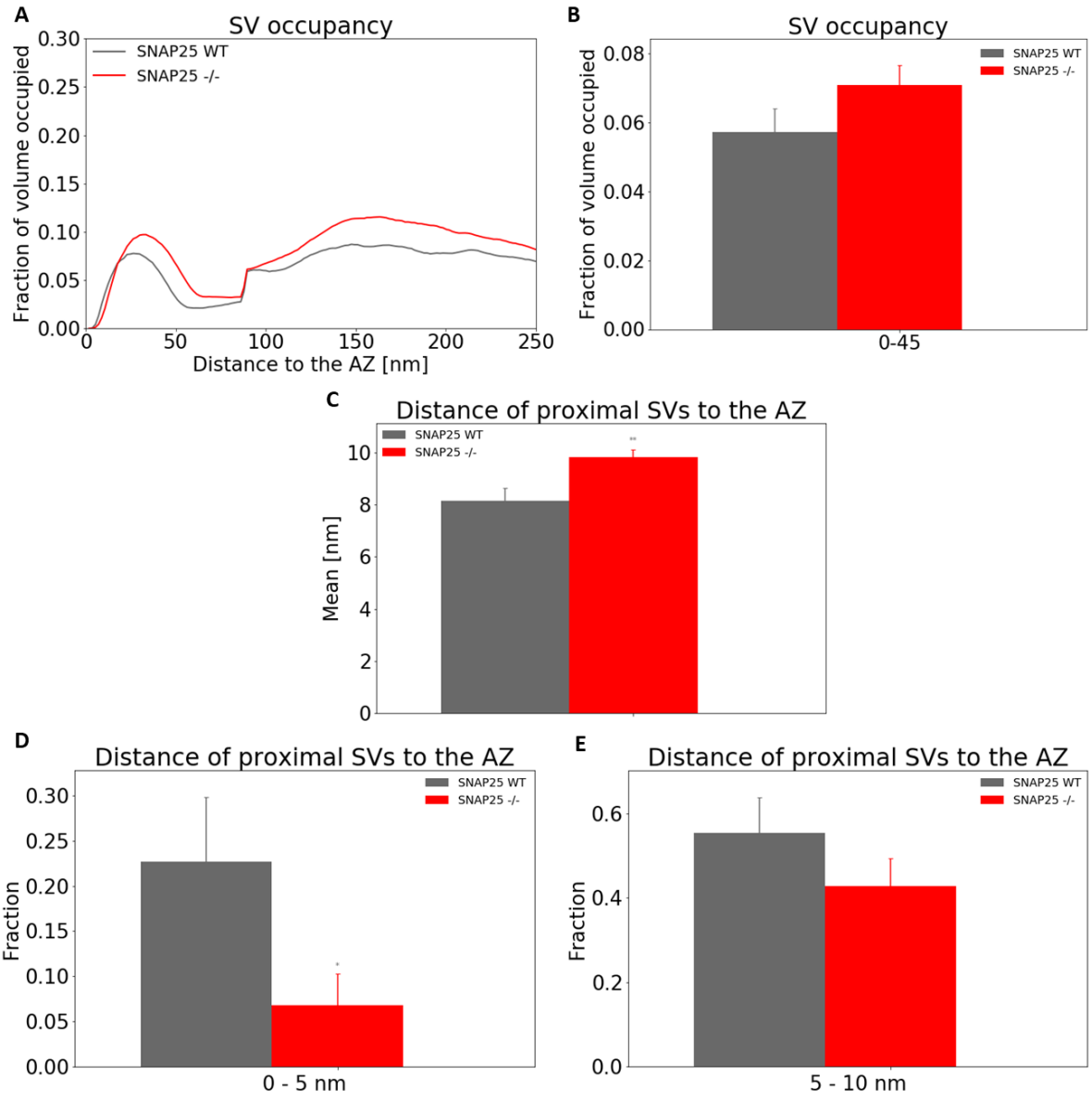

Figure 27: A: Mean SV occupancy of WT and SNAP25 KO, B: Occupancy of proximal SVs, C: Distance of proximal SVs to the AZ, D: Proximal SVs between 0 and 5nm from the AZ, E: Proximal SVs between 5 and 10nm from the AZ.

The mean tether length was significantly increased in the KO synaptosomes (KO: 16.41nm +/- 0.49, n = 344, WT: 12.70nm +/- 0.41, n = 349, $P < 0.001$, Kruskal test) (figure 28A). There were significantly fewer tethers shorter than 5nm in SNAP25 KO synaptosomes compared to the WT ones (KO: 0.02 +/- 0.01, n = 13, WT: 0.10 +/- 0.03, n = 9, $P < 0.01$, Kruskal test) (figure 28B).

Between 5nm and 10nm the tethers were somewhat fewer in SNAP25 KO, but still significant (KO: 0.17 +/- 0.04, n = 13, WT: 0.30 +/- 0.03, n = 9, P < 0.05, Kruskal test) (figure 28C).

Finally, the fraction of SVs that are tethered was similar between KO and WT synaptosomes (KO: 0.803, n = 147, WT: 0.791, n = 110, P = 0.8156, chi^2 test) (figure 28D). However, the number of tethers per tethered proximal SVs was significantly different (KO: 2.90 +/- 0.20, n = 118, WT: 4.01 +/- 0.28, n = 87, P < 0.001, Kruskal test) (figure 28E).

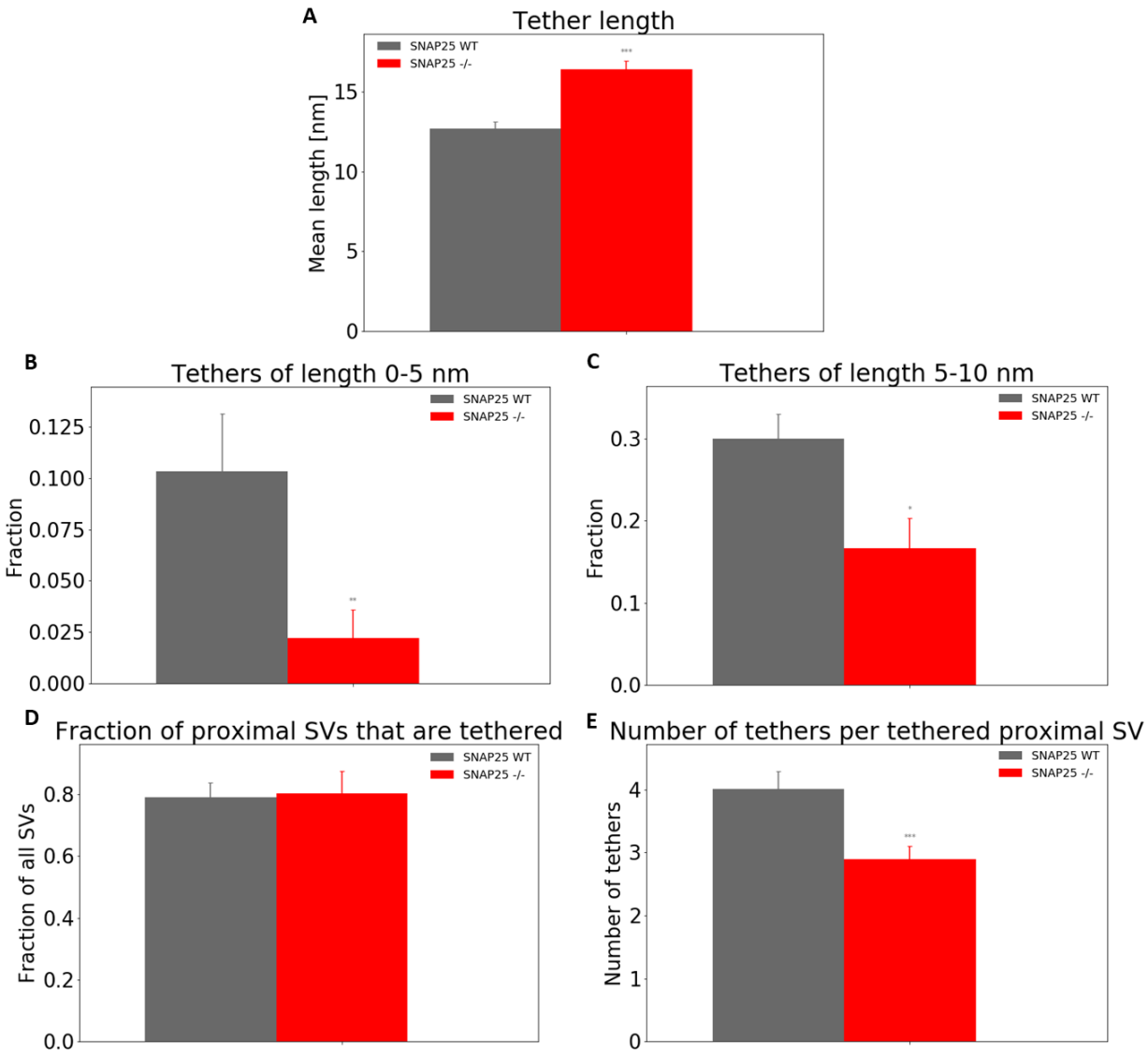

Figure 28: A: Mean tether length, B: Tethers between 0 and 5nm, C: Tethers between 5 and 10nm, D: Fraction of SVs that are tethered, E: Number of tethers per tethered proximal SV.

In conclusion, SNAP25 is very important to bring the SVs closer than 5nm to the AZ. Similarly, SNAP25 is crucial for the formation of shorter than 5nm tethers, and also of shorter than 10nm ones, but not in such a great manner. It is likely that the short tethers are responsible for localizing the SVs to the region of the presynaptic membrane where the t-SNARE is present.

4.5 Effects of PDBu on SNAP25 KO

We treated SNAP25 KO synaptosomes with PDBu, to study its effects in the absence of SNAP25 and we compared those synaptosomes with SNAP25 KO untreated ones. 7 tomograms of SNAP25 KO + PDBu were used for analysis (44% of all tomograms recorded from this condition). We didn't find any differences between those groups concerning the SV distribution and the distance of the proximal SVs from the AZ.

Concerning the tether length, there were, again, no differences (0 – 5nm: KO + PDBu: 0.02 +/- 0.01, n = 7, KO: 0.02 +/- 0.01, n = 13, P = 0.6091; 5 – 10nm: KO + PDBu: 0.18 +/- 0.05, n = 7, KO: 0.17 +/- 0.04, n = 13, P = 0.7810; > 10nm: KO + PDBu: 0.80 +/- 0.06, n = 7, KO: 0.81 +/- 0.04, n = 13, P = 0.9052; Kruskal test) (figures 29A, 29B, 29C). However, the number of tethers per AZ area was significantly increased in PDBu treated SNAP25 KO synaptosomes compared with the SNAP25 KO untreated ones (KO + PDBu: 233.47 +/- 27.16, n = 7, KO: 142.77 +/- 24.18, n = 14, P < 0.05, t test) and it was similar to SNAP 25 WT (figure 29D).

The fraction of SVs that were tethered was increased in SNAP25 KO PDBu treated synaptosomes, compared to the untreated ones, but not significantly. (KO + PDBu: 0.887, n = 124, KO: 0.803, n = 147, WT: 0.791, n = 110, P = 0.0582, chi^2 test) (figure 29E). On the other hand, the number of tethers per proximal SV was bigger (highly significant) between the treated and untreated synaptosomes (KO + PDBu: 4.13 +/- 0.24, n = 110, KO: 2.90 +/- 0.20, n = 118, P < 0.001, Kruskal test) (figure 29F).

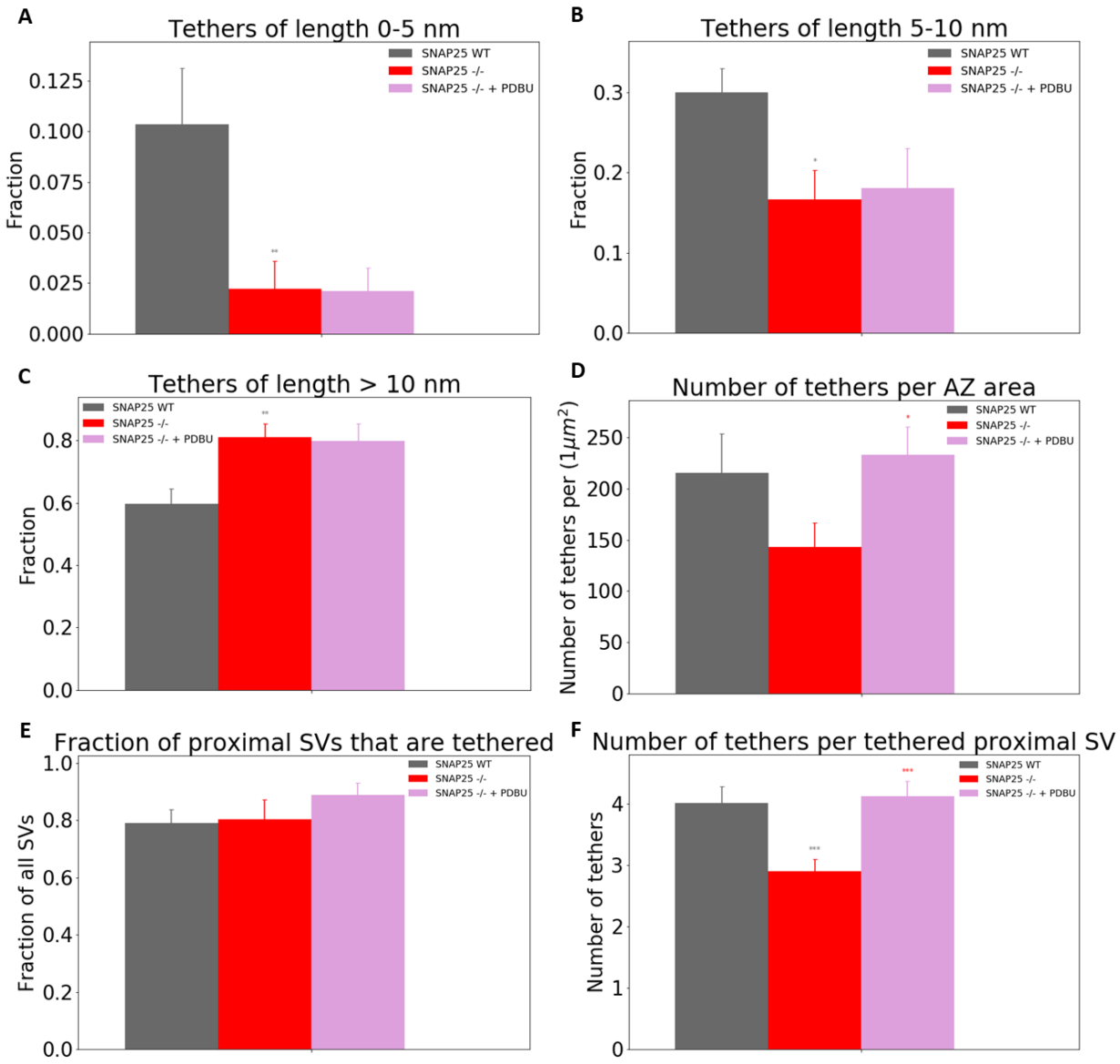

Figure 29: Tethers of length A: 0 – 5nm, B: 5 – 10nm, C: > 10nm, D: Number of tethers per AZ area, E: Fraction of proximal SVs that are tethered, F: Number of tethers per tethered proximal SV.

Our data shows that the presence of PDBu is not sufficient to bring the SVs closer than 5nm to the AZ in SNAP25 KO synaptosomes, because short tethers could not be formed due to the absence of SNAP25 (figure 29A). PDBu rescued the phenotype of SNAP25 KO concerning the decreased number of tethers per AZ area and the decreased number of tethers per proximal SV. However, PDBu does not fully rescue the SNAP25 KO phenotype because it doesn't increase the

fraction of tethers up to 5nm in length. Considering that the fraction of tethers in each of the tether length bins (< 5nm, 5-10nm and > 10nm) are very similar for SNAP25 KO with and without PDBu (Figure 29A-C), it appears that in this case PDBu does not modify the nature of tethers but only their number.

4.6 Connectivity

We did not find any differences between Munc13 DKO and WT concerning the fraction of proximal SVs that were connected (DKO: 0.878, n = 98, WT: 0.885, n = 182, chi^2 test) and the number of connectors per proximal SV (DKO: 5.02 +/- 0.42, n = 98, WT: 6.19 +/- 0.38, n = 182, Kruskal test). On the other hand, PDBu treated WT synaptosomes had alterations in connectivity in comparison with the untreated WT ones. Specifically, there were significantly fewer SVs that were connected when PDBu was present (WT + PDBu: 0.746, n = 59, WT: 0.885, n = 182, $P < 0.01$, chi^2 test) and the SVs from PDBu treated synaptosomes had significantly fewer connectors (WT + PDBu: 2.68 +/- 0.38, n = 59, WT: 6.19 +/- 0.38, n = 182, $P < 0.001$, Kruskal test). SNAP25 KO synaptosomes showed the opposite effects from PDBu. The fraction of SVs that were connected was significantly higher in SNAP25 KO compared to WT (KO: 0.932, n = 147, WT: 0.845, n = 110, $P < 0.05$, chi^2 test). Also, the number of connectors per proximal SV was significantly increased in SNAP25 KO synaptosomes (KO: 9.15 +/- 0.58, n = 147, WT: 5.24 +/- 0.46, n = 110, $P < 0.001$, Kruskal test). Treatment of SNAP25 KO synaptosomes with PDBu further increased the fraction of proximal SVs that were connected (KO + PDBu: 0.992, n = 124, KO: 0.932, n = 147, $P < 0.05$, chi^2 test) and did not significantly alter the number of connectors per proximal SV (KO + PDBu: 8.76 +/- 0.50, n = 124, KO: 9.15 +/- 0.58, n = 147, Kruskal test) (figures 30A, 30B).

It is an unexpected finding that the same two conditions that increase the number of tethers shorter than 5nm, PDBu treatment and the presence of SNAP25, decrease SV connectivity. We conclude that facilitation of SV release is inversely correlated with the proximal SV connectivity.

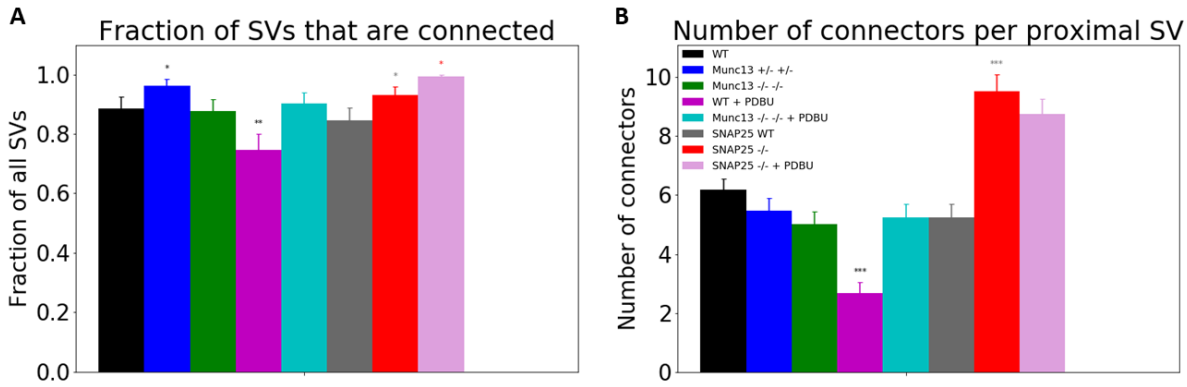

Figure 30: A: Fraction of proximal SVs that are connected, B: Number of connectors per proximal SV.

4.7 Correlation between the number of tethers and the SV distance to the AZ membrane

The number of tethers on each SV was inversely proportional to the SV's distance from the active zone. The more tethers a SV had, the closer to the AZ was (figure 31A). This correlation was significant for all the conditions of this project. This raises the possibility that the more tethers a SV had, the shorter its tethers were. This was indeed the case, as we found that this correlation was significant for all the conditions (figure 31B). In release-defective synapses that were previously investigated in our group, it was shown that there was a lack of the aforementioned correlation (Fernández-Busnadiego et al., 2013). Taken together we argue that this correlation can be used to detect disturbances in the SV accumulation in the proximal zone that are caused by processes upstream of SV priming.

<u>Proximal SV correlation between minimum distance from the AZ and number of tethers</u>

Condition	Number	r	Confidence	aRegress	bRegress
Munc13 WT	153	-0.5138	0.0000	-0.42	6.59
Munc13 DHET	68	-0.3985	0.0008	-0.23	5.48
Munc13 DKO	56	-0.5332	0.0000	-0.16	3.85
Munc13 WT + PDBu	46	-0.3156	0.0326	-0.24	5.76
Munc13 DKO + PDBu	38	-0.2559	0.1209	-0.08	3.07
SNAP25 WT	87	-0.4675	0.0000	-0.39	6.49
SNAP25 KO	118	-0.6130	0.0000	-0.46	7.02
SNAP25 KO + PDBu	105	-0.5374	0.0000	-0.43	7.97

Correlation between mean tether length (per SV) and number of tethers

Condition	Number	r	Confidence	aRegress	bRegress
Munc13 WT	153	-0.2316	0.0040	-0.09	5.02
Munc13 DHET	68	-0.2368	0.0519	-0.09	5.07
Munc13 DKO	56	-0.3291	0.0133	-0.04	2.84
Munc13 WT + PDBu	46	-0.2112	0.1589	-0.12	5.77
Munc13 DKO + PDBu	38	-0.0536	0.7491	-0.01	2.20
SNAP25 WT	87	-0.4382	0.0000	-0.20	6.88
SNAP25 KO	118	-0.2693	0.0032	-0.08	4.25
SNAP25 KO + PDBu	105	-0.2436	0.0123	-0.11	6.12

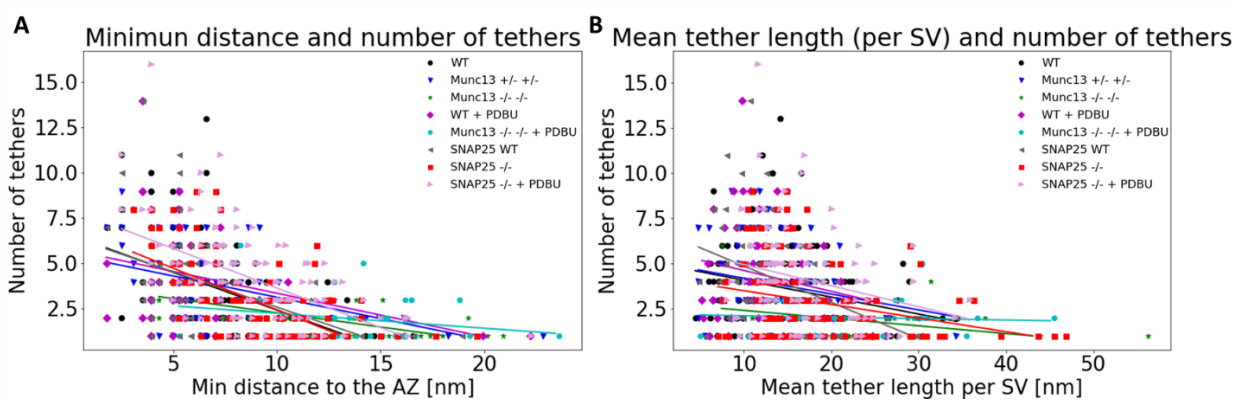

Figure 31: A: Proximal SV correlation between minimum distance to the AZ and number of tethers, B: Correlation between mean tether length (per SV) and number of tethers.

4.8 SV radius

The SVs of the Munc13 DKO synaptosomes had significantly bigger radius than the ones of the WT for the proximal (0 – 45nm from the AZ) (DKO: 23.04nm +/- 0.35, WT: 21.71nm +/- 0.34, $P < 0.05$, t test), the intermediate (45 – 75nm from the AZ) (DKO: 23.75nm +/- 0.35, WT: 21.01nm +/- 0.31, $P < 0.001$, t test), the distal 1 (75 – 150nm from the AZ) (DKO: 23.79nm +/- 0.26, WT: 22.18nm +/- 0.37, $P < 0.01$, t test) and the distal 2 (150 – 250nm from the AZ) (DKO: 23.62nm +/- 0.26, WT: 22.02nm +/- 0.33, $P < 0.001$, t test) SVs. The radius of the SVs in SNAP25 KO synaptosomes was, also, significantly bigger than the SNAP25 WT ones in all the aforementioned cases. More specifically, in the proximal level: KO: 24.60nm +/- 0.25, WT: 22.03nm +/- 0.33, $P < 0.001$; in the intermediate level: KO: 24.90nm +/- 0.39, WT: 21.50 +/- 0.48, $P < 0.001$; in the distal 1 level: KO: 24.81nm +/- 0.26, WT: 22.45nm +/- 0.39, $P < 0.001$ and in the distal 2 level: KO: 24.52nm +/- 0.25, WT: 22.06nm +/- 0.33, $P < 0.001$ (t test) (figure 32).

These results indicate that there is an inverse correlation between SV size and the synapse capability for neurotransmitter release.

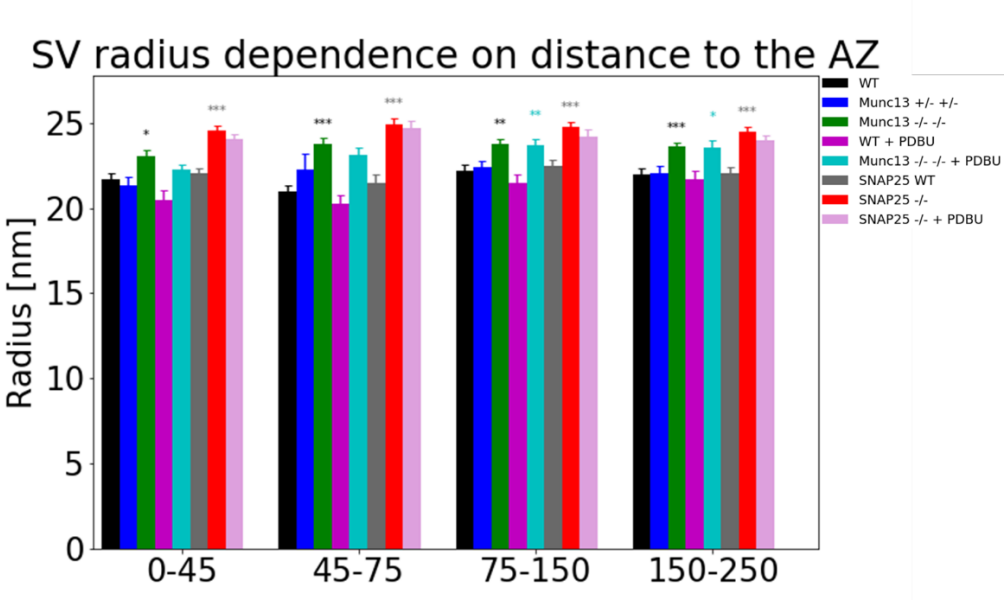

Figure 32: SV radius depending on the distance from the AZ.

4.9 Conclusion

The results of this project show that Munc13 and SNAP25 do not affect the overall distribution and number of SVs, but are required for the precise localization of proximal SVs. More specifically, they are both necessary for the localization of SVs up to 5nm from the AZ. Munc13, is also required for the localization of SVs up to 10nm from the AZ. Activation of Munc13 by PDBu increases the number of SVs closer than 5nm to the AZ. This points to a model where Munc13 is responsible for bringing the SVs closer than 10nm to the AZ and SNAP25 is necessary for bringing them closer than 5nm. Furthermore, both Munc13 and SNAP25 are required for the PDBu-induced increase in the number of SVs closer than 5nm.

The genetic removal of Munc13 reduces the number of tethered SVs and the number of tethers per SV, while it increases the length of the existing tethers. Considering that the fraction of tethers shorter than 10nm is significantly smaller when Munc13 is absent, we argue that MunC13 is required for the formation of these short tethers and that the absence of Munc13

significantly decreases SV tethering and affects the RRP. The fact that there were more tethers shorter than 10nm in the presence of PDBu, further supports this argument. SNAP25 is important for the formation of shorter than 5nm tethers and, to a lesser extent, for the formation of the tethers that are shorter than 10nm. The fraction of tethers up to 5nm in length did not increase upon PDBu application on SNAP25 KO synaptosomes, arguing that both SNAP25 and Munc13 are required for the formation of these, very short, tethers.

4.10 Trans-synaptic columns and ionotropic glutamate receptors

Besides the projects presented above about the role of tethers in neurotransmitter release, I also participated in a project aimed to detect the trans-synaptic colocalization of complexes residing at the pre and post synaptic terminal of a neuronal synapse. For this project I acquired tomograms from synaptosomes prepared by Dr. Zdravko Kochovski. There were two categories: control and stimulated synaptosomes (300μM Glu, 300μM Gly, and 30μM KCl for 1 min).

In total, 13 control and 21 stimulated synaptosomes were acquired and reconstructed, that came from two different preparations. From these tomograms, 11 were segmented and further processed by Dr. Antonio Martinez – Sanchez. These were used, along with tomograms recorded previously, to determine whether proteins of the pre and postsynaptic terminal are colocalized with each other forming trans-synaptic columns. Indeed, it was previously shown by super-resolution fluorescence that some proteins of the presynaptic terminal that are required for neurotransmitter release form nanoclusters, and are directly aligned with postsynaptic ionotropic glutamate receptors, which are necessary for synaptic transmission (Tang et al., 2016). The results of this project have been submitted for publication (Martinez-Sanchez et al., in submission).

The α-amino-3-hydroxy-5-methyl-4-isoxazole propionic acid (AMPA) receptors are abundant on the postsynaptic membrane. They belong to the ionotropic glutamate receptor

family and are localized at the excitatory synapses. AMPArs appear either as homo- or as heterotetramers from combinations of four core subunits: GluA1 – 4. In the brain, the majority of those tetramers contain the GluA2 subunit. The main domains of these receptors are the amino-terminal domain (NTD), the ligand-binding domain (LBD) and the transmembrane domain (TMD) (Greger, Watson, & Cull-Candy, 2017).

The atomic structure of AMPArs has already been solved (figure 33). However, this has been done by using crystallography or single particle electron microscopy. The problem with these techniques is that they require reconstituted receptors, but the exact composition of ion-pore forming and auxiliary subunits is not known. Furthermore, they are detergent-extracted from their native environment, which might cause changes in their conformation and composition. To obtain high resolution structures, they were also artificially stabilized by genetic modifications or pharmacological treatments (Sobolevsky, Rosconi, & Gouaux, 2009; Herguedas et al., 2016).

Together with AMPArs, N-methyl-d aspartate (NMDA) receptors are the main receptor families that bind L-glutamate. Ion currents through these channels initiate biochemical pathways that can change synaptic strength in a stimulation dependent manner (synaptic plasticity) and may lead to long term potentiation (LTP), which underlies higher cognitive processes such as learning and memory. Both channels are prominent components of synaptic nanodomains and have been found to be important for LTP (Nicoll, 2017).

We are interested in studying the structure and precise localization of the AMPArs in their native state, by using cryo-ET. Subtomogram classification and averaging has led to the point where we can distinguish the ionotropic glutamate receptors from other particles present on the postsynaptic membrane and tentatively identify AMPArs and NMDArs. Our goal in this project is to develop a method for direct detection AMPArs in cryo-tomograms of synapses.

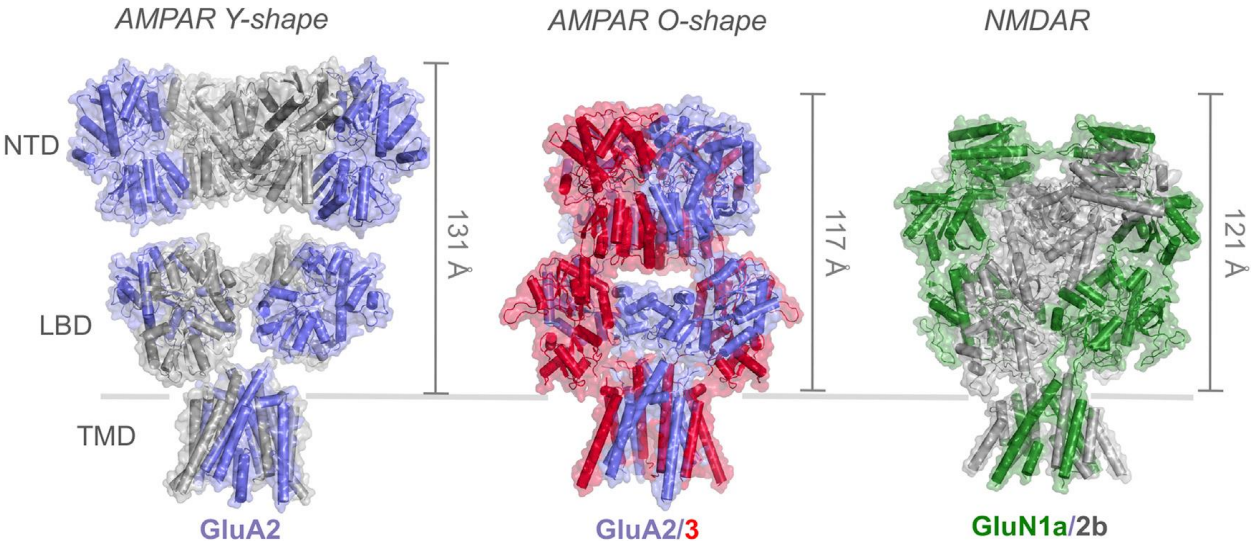

Figure 33: Structures of homomeric GluA2 (left), heteromeric GluA2/GluA3 (center) AMPAr and the GluN1a/2b NMDAr (right). Using current subtomogram classification and averaging techniques we can distinguish the ionotropic glutamate receptors from other particles present on the postsynaptic membrane (Greger et al., 2017)

To this end, we prepared hippocampal rodent synaptosomes, applied an antibody that specifically binds GluA2 ion-pore forming subunit (figure 34) and imaged them by cryo-ET. We plan to detect, classify and average postsynaptic complexes (Martinez-Sanchez et al., in submission) according to the procedure we already developed (Martinez-Sanchez, Kochovski, et al., 2020). This may yield a class average that is similar to AMPA structure but contain an additional density. I recorded and reconstructed 13 tomograms (7 from the 1:100 dilution prep and 6 from the 1:30 one) which were pooled together for analysis.

Figure 34: Structure of the full-length AMPAr GluA2 homomer (Dürr et al., 2014). *Part of the NTD (aa 175-430) of the GluA2 subunit at which the monoclonal antibody specifically binds are shown in green (ThermoFisher GluR2 clone 6C4)*

Previous studies have shown that, in their most upright state, AMPArs are taller than NMDArs (Greger et al., 2017). However, both AMPArs and NMDArs can adopt a range of different conformations, which makes it difficult to obtain average structures. Consequently, previous studies used different reagents to stabilize their conformation. It was shown that AMPArs can be stabilized by using ZK 200775 hydrate, an AMPAr antagonist (Yelshanskaya, Saotome, Singh, & Sobolevsky, 2016) or (S)-5-Nitrowillardiine (NOW), which is an AMPAr agonist (Dürr et al., 2014).

I have treated synaptosomes with both ligands and recorded and reconstructed 4 tomograms from the NOW preparation. We expect that by stabilizing these receptors, we will be able to obtain averages at higher resolution and that these will be more similar to the published (stabilized) structures. This will provide another way to distinguish between the ionotropic glutamate receptors. Regarding NMDArs, Ifenprodil hemitartrate and Ro 25-6981 maleate salt are both NMDAr inhibitors that bind between GluN1b and GluN2b NTD proteins, stabilizing their

form (Karakas, Simorowski, & Furukawa, 2011). We are planning to use both these substances for synaptosomal preparations.

To prepare the tomograms for further processing, the following regions were manually segmented: pre and post synaptic membrane, the cytosol areas of the pre and post synaptic terminals up to 30nm from their respective membranes, the proximal SVs and the synaptic cleft.

The next step was the picking of the particles of interest, which, in this case, were the ionotropic glutamate receptors. Densities were traced in 3D using the discrete Morse theory segmentation and the topological persistence simplification (Sousbie, 2011; Martinez-Sanchez et al., 2020). The particles were detected by applying topological and geometrical restrictions and by determining their membrane-normal vectors. In this way, the tracing of the densities and the picking of the particles avoid template-based picking bias (Henderson, 2013). These particles were cleaned and split into different classes according to their morphological features by using affinity propagation (AP) clustering. The classes were, finally, refined and 3D reconstructed (figure 35).

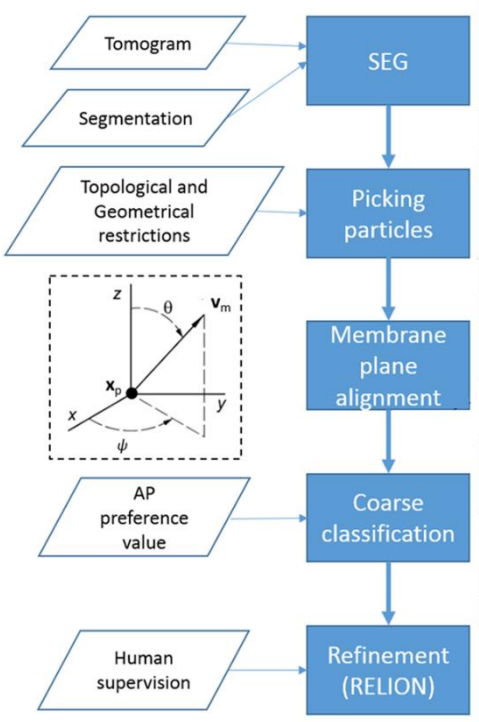

Figure 35: Pipeline used for this project, from the reconstructed tomogram, to the final structure refinement (image courtesy of Dr. Antonio Martinez-Sanchez).

Preliminary processing yielded two main classes of postsynaptic complexes (figure 36). Based on their dimensions, it can be seen that they both are ionotropic glutamate receptors. In one of the classes, some protrusions can be observed, that haven't been shown in previous experiments, something that leads to the hypothesis that they depict parts of the antibodies binding to the GluA2 subunit of the AMPArs. Therefore, we established that this is a promising procedure to directly detect and identify AMPArs and NMDArs at synapses.

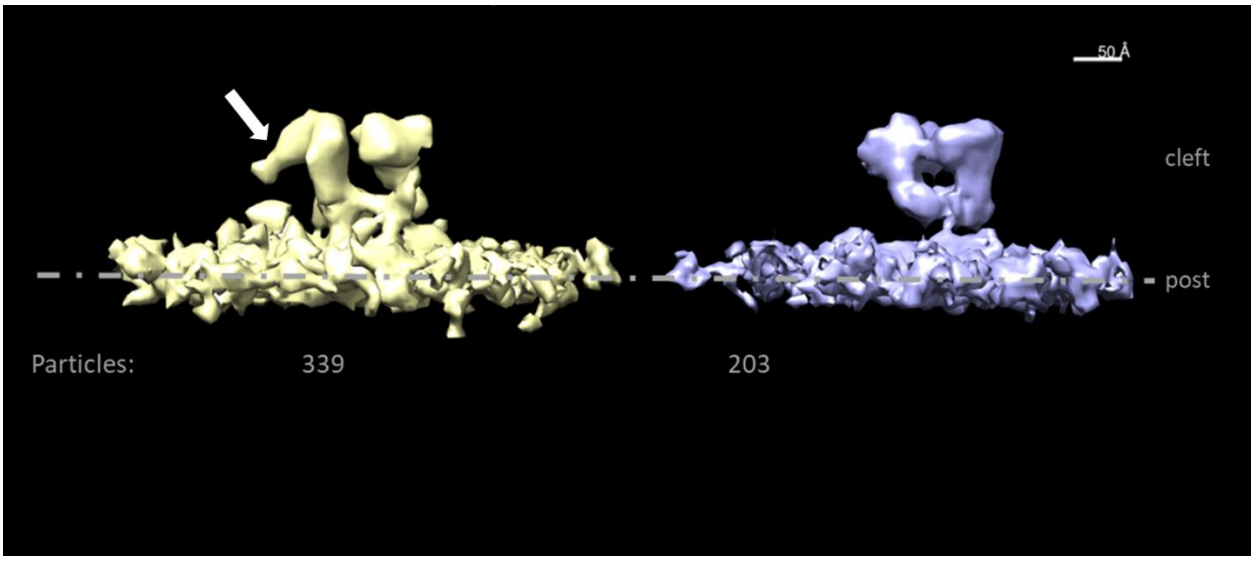

Figure 36: 2 classes of postsynaptic complexes yielded from this project. We can observe some protrusions at the class on the left (white arrow), that haven't been shown in previous experiments. We hypothesize that these protrusions depict the part of the antibodies that binds on the GluA2 subunit of the AMPAr.

5. Discussion

5.1 RIM brings the SVs at the proximal zone

Technical difficulties involved in cryo-ET of synapses isolated from dissociated neuronal cultures severely limited the number of synaptosomes recorded and analyzed in this study. Nevertheless, our data showed that the lack of all RIM isoforms alters the SV distribution at the presynaptic terminal. The proximal SV concentration peak in WT synapses cannot be observed in the absence of RIM. The work from our group has previously shown that lack of RIM1α can also alter the SV distribution. Based on this distribution, RIM1α KO synapses were separated into two classes, the altered (severe disruption in SV distribution and tethering formation) and the aligned one (no disruption in SV distribution). It was, then, hypothesized that in the aligned class, other isoforms of RIM take over and act in place of RIM1α. It was speculated that these are RIM1α independent synapses (Fernández-Busnadiego et al., 2013). The present study clearly verifies this hypothesis because lack of all RIM isoforms causes disruptions in this distribution similar to the altered class of the RIM1α KO synapses.

We cannot say which isoforms specifically take over in RIM1α independent synapses. However, it has been shown that the Zn^{2+} finger domain of RIM binds to the C2A domain of Munc13, disrupting its homodimerization and, thus, leading to SV priming (Deng et al., 2011). Besides RIM1α, only RIM1β and RIM2α have Zn^{2+} finger domain, so they are the main candidates of replacing RIM1α in the aligned class of RIM1α-independent synapses.

The decrease of the number of tethers in RIM TKO synapses paralleled the decrease of the number of SVs. However, the properties of the RIM-independent tethers were indistinguishable from those of the WT. Because the number of synaptosomes that we could analyze was small, and we could not make further conclusions concerning the tethering organization of RIM TKO synapses, our data argues that RIM isoforms are to a large extent

required for the localization of SVs in the proximal zone, but that tethers are composed of proteins other than RIMs.

5.2 Munc13 and SNAP25 localize precisely the SVs

Contrary to RIM, the overall distribution and number of SVs is not affected by Munc13 or SNAP25. However, our data showed that these proteins are required for the precise localization of SVs within the proximal zone. More specifically, based on the results of this project, Munc13 is necessary for localization of SVs up to 10nm from the AZ. It is, also, required for the formation of tethers shorter than 10nm. The absence of these tethers is probably the main reason why SVs are located further than 10nm from the AZ when Munc13 is not present. SNAP25 is important for the localization of SVs up to 5nm from the AZ. The results of this project appear consistent with the previous research claiming that proximal SVs in Munc13 DKO synapses were accumulating at distances of 8 – 10nm from the AZ and in SNAP25 KO synapses they were found at 4–8 nm from the AZ (Imig et al., 2014). The discrepancy in the precise SV localization is likely caused by dehydration and the use of aldehyde fixatives in the previous research. Our study shows, for the first time, the effects of Munc13 and SNAP25 on tethering organization.

Munc13 affects the RRP, and this has been shown before (Varoqueaux et al., 2002; Jockusch et al., 2007; Imig et al., 2014). In our study though, we showed this effect through the multiply tethered SVs aspect. Because this was not as strong in SNAP25 KO synapses, we argue that SNAP25 affects the RRP as well, but to a lesser extent.

5.3 Effects of PDBu on Munc13 and SNAP25

Our data shows that the number of SVs closer than 5nm to the AZ are increased upon PDBu treatment. This effect requires Munc13, consistent with a previous study from our group

(Laugks, 2018) and also with the finding that PDBu activates Munc13 (Parfitt & Madison, 1993). Differences in sample preparation might be responsible for the inconsistency between our and the previous data regarding the number of tethers per SV in PDBu treated synapses. We found, however, that PDBu treated SNAP25 KO synaptosomes had significantly more tethers per SV than the untreated SNAP25 KO ones, and that this number reached the WT level. This phenomenon can be explained by proposing that PDBu constitutively increases the number of tethers per SV. Because SNAP25 is required for the fusion of the SVs with the membrane, multiply tethered SVs are not removed by fusion in SNAP25 KO, leading to an increase in the number of tethers per SV.

5.4 Correlation between connectivity and tethering in proximal SVs

It was previously shown by our group that the number of connectors on proximal SVs was increased in RIM1α KO synapses (Fernández-Busnadiego et al., 2013). Here, we found that the two conditions that increase the number of tethers shorter than 5 nm, PDBu treatment and the presence of SNAP25, decrease both the fraction of proximal SVs that are connected and the number of connectors per proximal SV. This is surprising, because both PDBu and SNAP25 are expected to exert their function close to the plasma membrane, while connectors are bound only to SVs. All together, these findings led us to the hypothesis that SVs lose connectors during their progression towards release. Furthermore, it suggests that proteins involved in the tethering and neurotransmitter release, also regulate SV connectors.

5.5 Increased SV radius in synapses with blocked transmission

The observation that Munc13 DKO and SNAP25 KO SVs are larger than the WT ones has been made before (Imig et al., 2014). Also, our group has previously shown that SVs from RIM1α KO synapses are larger compared to WT. The fact that SV fusion occurs in RIM1α KO synapses

means that the increased SV size is not correlated with a complete block of synaptic transmission. Instead, we suggest that the SV size is only inversely correlated with a probability of release.

5.6 Model of proximal SV tethering

Based on the results of these projects and also from previous projects in our group, we suggest the following model concerning the proximal SV organization and tether formation (figure 38): before entering the proximal zone, the SVs are either untethered, or have a small number of long tethers. RIM is the main factor that brings the SVs to the proximal zone, and it may be responsible for the formation of the long tethers (>20nm). Then, Munc13 brings the SVs closer than 10nm to the AZ, possibly by increasing the number of tethers shorter than 10nm. The SVs are coming closer than 5nm to the AZ with the help of SNAP25, which is also necessary for the formation of shorter than 5nm tethers. SNAP25 (or the formation of the SNARE complex in general) also reduces the number of connectors from the proximal SVs. The activation of Munc13 by PDBu increases the number of SVs closer than 5nm. With the arrival of an action potential, there is Ca^{2+} influx at the presynaptic terminal, which facilitates the full zippering of the SNARE complex, the fusion of the SV and the plasma membrane and the release of the neurotransmitter to the synaptic cleft. At this point, we cannot determine whether the connectors from the SVs that fuse are completely removed, or become tethers themselves.

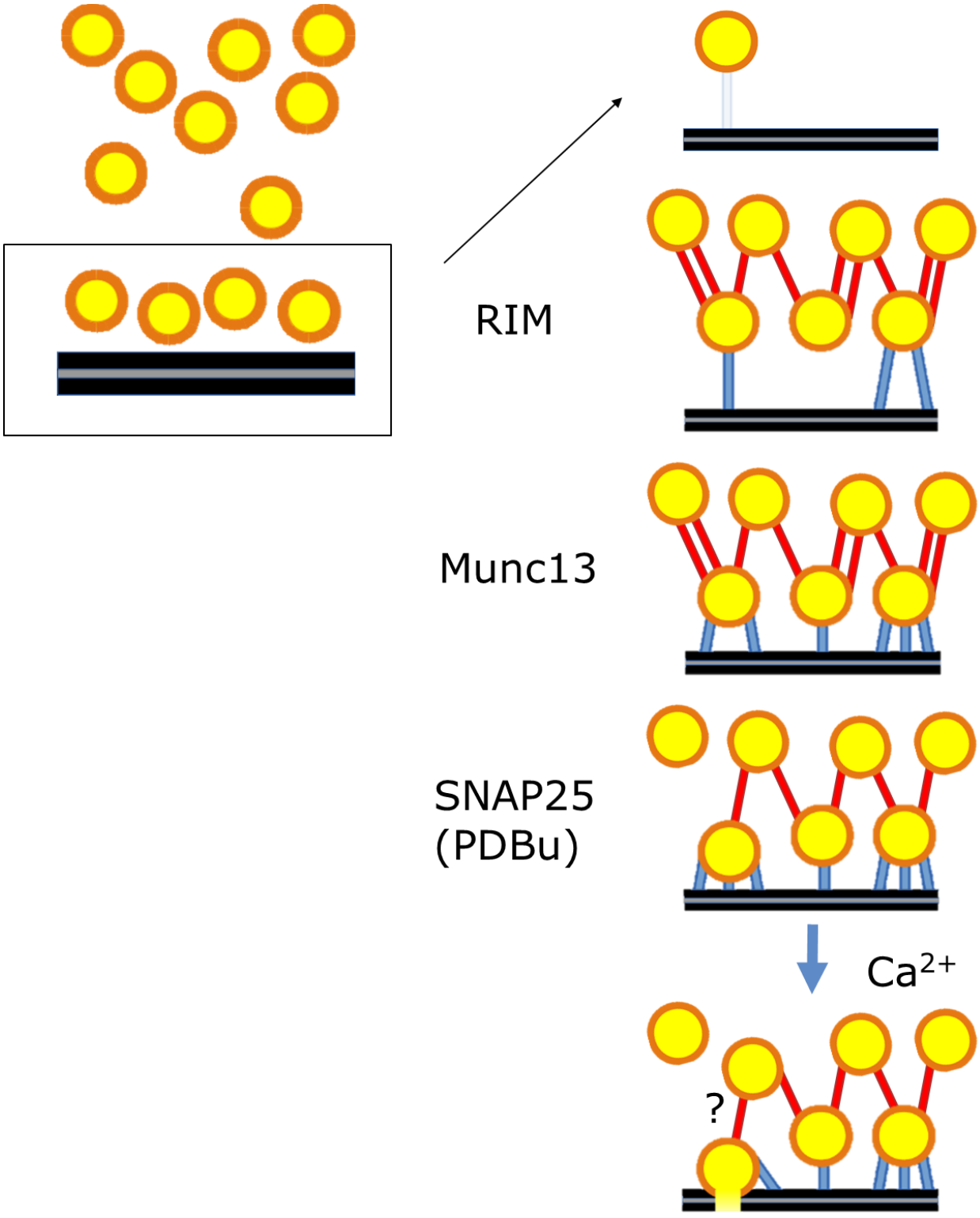

Figure 37: Suggested model of tethering of proximal SVs. AZ membrane: black, SVs: yellow, connectors: red, tethers: blue

As mentioned in the introduction, there are two different models that describe the formation of the pre-fusion complex: the partially zippered model (currently most prevalent) and the non-zippered model (alternative). Our results show that the SVs are brought to the proximal level by RIM and are tethered to the AZ membrane irrespective of the SNARE complex formation (mainly through the effects of Munc13). We also hypothesize that Munc13 is not only regulating tether formation, but is structurally part of – at least some of – them. This seems to be closer to the non-zippered model, which suggests that initially, Munc13 precisely positions proximal SVs close to the plasma membrane, in the vicinity of activated SNARE acceptor complexes. However, we cannot conclude whether the partially zippered SNARE complex exists as a stable state before the SV fusion or not.

5.7 Future work

Primary cultured neurons from RIM TKO animals are usually viable no longer than 16 DIV, from which only a small amount of synaptosomes can be isolated. The approach of crossing two different knockout mice to get RIM 1/2 DKO embryos and proceed with isolating synaptosomes from organotypic hippocampal slices (similar to the Munc13 and SNAP25 projects) was considered. However, deletion of RIM 1α and RIM 1β severely impairs mouse survival (Kaeser et al., 2011), which means that no such mice can be used for breeding. Our collaborators in Bonn tried combining the two techniques: RIM 2 KO mice were used to create organotypic hippocampal slices and the cre/loxp system was used to remove RIM 1 from them. Unfortunately, preliminary trials failed to reduce the levels of RIM 1 in the slices. We suggest, however, that a more carefully planned design of this experiment might give satisfactory results. On the other hand, inability to remove RIM 1 from all the synapses of the hippocampal slices would mean that a very big number of synaptosomes would have to be recorded, to ensure that the vast majority of them would be RIM 1/2 DKO ones and not just RIM 2 KO.

Generally, the isolation of synaptosomes from dissociated neuronal cultures proved to be challenging. Our inability to find synapses on grids prepared from neuronal cultures of WT neurons further supports the idea that synaptosomal preparation from dissociated cultures is the problem, rather than the mouse genetics. However, we only checked a very small number of grids and we suggest that more experiments need to be performed before making any conclusive remarks. We think that the protocol we used for synaptosomal isolation from dissociated neuronal cultures (see Materials and Methods section for more information) can still be of use for this purpose.

We clearly showed that Munc13 is required for the formation of tethers shorter that 10nm. What we still don't know is if Munc13 is also structurally part of them. A first step that will lead us on that direction is to use the, already known, structure of Munc13 and check if it can fit to the structure of shorter than 10nm tethers in WT synaptosomes.

The SNARE complex is the most important machinery for SV fusion. However, researchers have still not found how exactly it structurally fits between the SV and the presynaptic membrane. We had hypothesized that at least some of the shorter than 5nm tethers contain the SNARE complex. Indeed, based on the results of this project, SNAP25 is necessary for the formation of such tethers. Fitting of the SNARE structure on these short tethers will further support our hypothesis.

Distinction between the AMPARs and the NMDARs *in situ* will be essential to give us more information about their structure and functionality, without removing them from their natural environment. The preliminary results from the use of an anti-GluA2 antibody to identify the AMPARs were encouraging and we believe that more data should be recorded for this project. As mentioned at the Results section, there are substances that stabilize AMPARs' and NMDARs' conformation to their most upright state, and, thus, making it easier to distinguish them from each other. We strongly suggest that synaptosome preparations are made using these reagents, to see if AMPARs and NMDARs can be more easily distinguished.

With the technological advances in tomogram acquisition and image processing, subtomogram averaging will only get more streamlined. Structures will be identified more easily and better resolutions will be reached. With the currently used number of particles and pixel size,

subtomogram averaging of tethers is unlikely to give conclusive results. However, we believe that increasing the number of particles (by recording more tomograms) and using a smaller pixel size (by recording in higher magnification) will make classification of tethers and identification of their structures *in situ* successful and will provide more conclusive answers regarding their structure and their functionality.

6. Abbreviations

AMPAr	α-amino-3-hydroxy-5-methyl-4-isoxazole propionic acid receptor
ATP	Adenosine Triphosphate
AZ	Active Zone
CAZ	Cytomatrix of the Active Zone
CCD	Charge Coupled Device
Cryo-EM	Cryo electron microscopy
Cryo-ET	Cryo Electron Tomography
CTF	Contrast-Transfer-Function
DDD	Direct electron Detector Device
DHET	Double Heterozygous
DIV	Days *in vitro*
DKO	Double Knock-Out
DPBS	Dulbecco Phosphate Buffer Saline
DQE	Detective Quantum Efficiency
EM	Electron Microscope (or Electron Microscopy)
FBS	Fetal Bovine Serum
FEG	Field Emission Gun
FS	Freeze Substitution
FuDR	Fluorodeoxyuridine
GIF	Gatan Imaging Filter
HBM	Hepes-Buffered Medium
HBSS	Hank's Balanced Salt Solution
HPF	High Pressure Freezing
IMOD	Image processing, Modeling and Display program
KO	Knock-Out

LBD	Ligand-Binding Domain
LM	Light Microscope (or Light Microscopy)
LN_2	Liquid Nitrogen
LTP	Long Term Potentiation
NMDAr	N-methyl-d aspartate receptor
NOW	(S)-5-Nitrowillardiine
NPM	Neuronal Plating Medium
NSF	N-ethylmaleimide (NEM)-Sensitive Fusion protein
NTD	Aminoterminal Domain
PBS	Phosphate Buffer Saline
PDBu	4-b-phorbol-12,13-dibutyrat
PI	Protease Inhibitor
PLL	Poly-L-Lysine
PSD	Post Synaptic Density
PSF	Point Spread Function
RIM	Rab3-Interacting Molecule
RIM-BP	RIM Binding Protein
RRP	Readily Releasable Pool
SEM	Scanning Electron Microscope (or Scanning Electron Microscopy)
SNAP	Soluble N-ethylmaleimide sensitive factor Attachment protein
SNAP25	Synaptosomal-Associated Protein, 25kDa
SNARE	Soluble N-ethylmaleimide sensitive factor Attachment protein Receptor
SNR	Signal to Noise Ratio
SPA	Single Particle Analysis
SV	Synaptic Vesicle
TEM	Transmission Electron Microscope (or Transmission Electron Microscopy)
TKO	Total Knock-Out
TM	Transmembrane
TMD	Transmembrane Domain

6. Abbreviations

VAMP	Vesicle-Associated Membrane Protein (Synaptobrevin)
VPP	Volta Phase Plate
WT	Wild Type

7. Bibliography

Aebi, U., & Pollard, T. D. (1987). A glow discharge unit to render electron microscope grids and other surfaces hydrophilic. *Journal of Electron Microscopy Technique*, *7*(1), 29–33. https://doi.org/10.1002/jemt.1060070104

Albert, S., Schaffer, M., Beck, F., Mosalaganti, S., Asano, S., Thomas, H. F., Plitzko, J.M, Beck, M., Baumeister, W., Engel, B. D. (2017). Proteasomes tether to two distinct sites at the nuclear pore complex. *Proceedings of the National Academy of Sciences of the United States of America*, *114*(52), 13726–13731. https://doi.org/10.1073/pnas.1716305114

Antonin, W., Fasshauer, D., Becker, S., Jahn, R., & Schneider, T. R. (2002). Crystal structure of the endosomal snare complex reveals common structural principles of all snares. *Nature Structural Biology*, *9*(2), 107–111. https://doi.org/10.1038/nsb746

Asano, S., Fukuda, Y., Beck, F., Aufderheide, A., Förster, F., Danev, R., & Baumeister, W. (2015). A molecular census of 26S proteasomes in intact neurons. *Science*, *347*(6220), 439–443.

Ashton, A. C., & Ushkaryov, Y. A. (2005). Properties of synaptic vesicle pools in mature central nerve terminals. *Journal of Biological Chemistry*, *280*(44), 37278–37288. https://doi.org/10.1074/jbc.M504137200

Augustin, I., Rosenmund, C., Südhof, T. C., & Brose, N. (1999). Munc13-1 is essential for fusion competence of glutamatergic synaptic vesicles. *Nature*, *400*(6743), 457–461. https://doi.org/10.1038/22768

Bai, X. C., Fernandez, I. S., McMullan, G., & Scheres, S. H. W. (2013). Ribosome structures to near-atomic resolution from thirty thousand cryo-EM particles. *ELife*, *2013*(2), 2–13. https://doi.org/10.7554/eLife.00461

Balázs, R., Hajós, F., Johnson, A. L., Reynierse, G. L. A., Tapia, R., & Wilkin, G. P. (1975). *Subcellular fractionation of rat cerebellum: An electron microscopic and biochemical investigation. III. Isolation of large fragments of the cerebellar glomeruli*. *86*(1), 17–30.

Bammes, B. E., Jakana, J., Schmid, M. F., & Chiu, W. (2010). Radiation damage effects at four specimen temperatures from 4 to 100 K. *Journal of Structural Biology*, *169*(3), 331–341. https://doi.org/10.1016/j.jsb.2009.11.001

Basu, J., Shen, N., Dulubova, I., Lu, J., Guan, R., Guryev, O., Grishin, N. V., Rosenmund, C., Rizo, J. (2005). A minimal domain responsible for Munc13 activity. *Nature Structural and Molecular Biology*, *12*(11), 1017–1018. https://doi.org/10.1038/nsmb1001

Bäuerlein, F. J. B., Saha, I., Mishra, A., Kalemanov, M., Martínez-Sánchez, A., Klein, R., Dudanova, I., Hipp, M. S., Hartl, F. U., Baumeister, W., Fernández-Busnadiego, R. (2017). In

Situ Architecture and Cellular Interactions of PolyQ Inclusions. *Cell*, *171*(1), 179-187.e10. https://doi.org/10.1016/j.cell.2017.08.009

Baumeister, W. (2005). A voyage to the inner space of cells. *Protein Science*, *14*(1), 257–269. https://doi.org/10.1110/ps.041148605.took

Blundell, J., Kaeser, P. S., Südhof, T. C., & Powell, C. M. (2010). RIM1α and interacting proteins involved in presynaptic plasticity mediate prepulse inhibition and additional behaviors linked to schizophrenia. *Journal of Neuroscience*, *30*(15), 5326–5333. https://doi.org/10.1523/JNEUROSCI.0328-10.2010

Booth, C., & Mooney, P. (2013). Applications of electron-counting direct-detection cameras in high- resolution cryo-electron microscopy. *Microscopy and Analysis*, *27*(6), 13–21.

Brandt, F., Carlson, L. A., Hartl, F. U., Baumeister, W., & Grünewald, K. (2010). The Three-Dimensional Organization of Polyribosomes in Intact Human Cells. *Molecular Cell*, *39*(4), 560–569. https://doi.org/10.1016/j.molcel.2010.08.003

Broadie, K., Prokop, A., Bellen, H. J., O'Kane, C. J., Schulze, K. L., & Sweeney, S. T. (1995). Syntaxin and synaptohrevin function downstream of vesicle docking in drosophila. *Neuron*, *15*(3), 663–673. https://doi.org/10.1016/0896-6273(95)90154-X

Brodin, L., & Shupliakov, O. (2006). Giant reticulospinal synapse in lamprey: Molecular links between active and periactive zones. *Cell and Tissue Research*, *326*(2), 301–310. https://doi.org/10.1007/s00441-006-0216-2

Brose, N., Hofmann, K., Hata, Y., & Sudhof, T. C. (1995). Mammalian homologues of Caenorhabditis elegans unc-13 gene define novel family of C2-domain proteins. *Journal of Biological Chemistry*, *270*(42), 25273–25280. https://doi.org/10.1074/jbc.270.42.25273

Brunger, A. T., Choi, U. B., Lai, Y., Leitz, J., White, K. I., & Zhou, Q. (2019). The pre-synaptic fusion machinery. *Current Opinion in Structural Biology*. https://doi.org/10.1016/j.sbi.2019.03.007

Brunger, A. T., Leitz, J., Zhou, Q., Choi, U. B., & Lai, Y. (2018). Ca 2+ -Triggered Synaptic Vesicle Fusion Initiated by Release of Inhibition. *Trends in Cell Biology*, *28*(8), 631–645. https://doi.org/10.1016/j.tcb.2018.03.004

Burkhardt, P., Hattendorf, D. A., Weis, W. I., & Fasshauer, D. (2008). Munc18a controls SNARE assembly through its interaction with the syntaxin N-peptide. *EMBO Journal*, *27*(7), 923–933. https://doi.org/10.1038/emboj.2008.37

Castillo, P.E., Schoch, S., Schmitz, F., Sudhof, T. C., & Malenka, R. C. (2002). RIM1α is required for presynaptic longterm potentiation. *Nature*, *415*, 327–330.

Castillo, Pablo E., Janz, R., Südhof, T. C., Tzounopoulos, T., Malenka, R. C., & Nicoll, R. A. (1997). Rab3A is essential for mossy fibre long-term potentiation in the hippocampus. *Nature*, *388*(6642), 590–593. https://doi.org/10.1038/41574

Chang, J. W., Arnold, M. M., Rozenbaum, A., Caputo, A., Schweizer, F. E., Huynh, M., Mathern,

G. W., Sarafian, T. A., Watson, J. B. (2012). Synaptoneurosome micromethod for fractionation of mouse and human brain, and primary neuronal cultures. *Journal of Neuroscience Methods*, *211*(2), 289–295. https://doi.org/10.1016/j.jneumeth.2012.09.005

Clinton, J., Blackman, S. E., Royston, M. C., & Roberts, G. W. (1994). Differential synaptic loss in the cortex in Alzheimer's disease: a study using archival material. *Neuroreport*, *5*(4), 497–500. https://doi.org/10.1097/00001756-199401120-00032

Cogliati, S., Enriquez, J. A., & Scorrano, L. (2016). Mitochondrial Cristae: Where Beauty Meets Functionality. *Trends in Biochemical Sciences*, *41*(3), 261–273. https://doi.org/10.1016/j.tibs.2016.01.001

Couteaux, R., & Pécot-Dechavassine, M. (1970). [Synaptic vesicles and pouches at the level of "active zones" of the neuromuscular junction]. *Comptes Rendus Hebdomadaires Des Seances de l'Academie Des Sciences. Serie D: Sciences Naturelles*, *271*(25), 2346–2349. Retrieved from http://www.ncbi.nlm.nih.gov/pubmed/4995202

Crowther, R. A., DeRosier, D. J., & Klug, A. (1970). The reconstruction of a three-dimensional structure from projections and its application to electron microscopy. *Royal Society*, *317*(1530), 319–340.

Danev, R., Buijsse, B., Khoshouei, M., Plitzko, J. M., & Baumeister, W. (2014). Volta potential phase plate for in-focus phase contrast transmission electron microscopy. *Proceedings of the National Academy of Sciences of the United States of America*, *111*(44), 15635–15640. https://doi.org/10.1073/pnas.1418377111

De Robertis, E., Pellegrino De Iraldi, A., Rodriguez De Lores Garnaiz, G., & Salganicoff, L. (1962). Cholinergic and Non-Cholinergic Nerve Endings in Rat Brain. I. Isolation and Subcellular Distribution of Acetylcholine and Acetylcholinesterase. *J Neurochem*, (9), 23–35. https://doi.org/10.1111/j.1471-4159.1962.tb07489.x

De Rosier, D. J., & Klug, A. (1968). Reconstruction of three dimensional fiber structures from orthogonal projections. *Nature*, *217*, 130–134.

Delgado-Martínez, I., Nehring, R. B., & Sørensen, J. B. (2007). Differential abilities of SNAP-25 homologs to support neuronal function. *Journal of Neuroscience*, *27*(35), 9380–9391. https://doi.org/10.1523/JNEUROSCI.5092-06.2007

Deng, L., Kaeser, P. S., Xu, W., & Südhof, T. C. (2011). RIM proteins activate vesicle priming by reversing autoinhibitory homodimerization of munc13. *Neuron*. https://doi.org/10.1016/j.neuron.2011.01.005

Dierksen, K., Typke, D., Hegerl, R., Koster, A. J., & Baumeister, W. (1992). Towards automatic electron tomography. *Ultramicroscopy*, *40*(1), 71–87. https://doi.org/10.1016/0304-3991(92)90235-C

Dubochet, J., Adrian, M., Chang, J. J., Homo, J. C., Lepault, J., McDowall, A. W., & Schultz, P. (1988). Cryo-electron Microscopy of Vitrified Specimens. *Q Rev Biophys*, *21*(2), 129–228.

Dubochet, J., & McDowall, A. W. (1981). Vitrification of Pure Water for Electron Microscopy. *Journal of Microscopy*, *124*, 3–4.

Dulubova, I., Lou, X., Lu, J., Huryeva, I., Alam, A., Schneggenburger, R., Südhof, T. C., Rizo, J. (2005). A Munc13/RIM/Rab3 tripartite complex: From priming to plasticity? *EMBO Journal*, *24*(16), 2839–2850. https://doi.org/10.1038/sj.emboj.7600753

Dunkley, P. R., Jarvie, P. E., & Rostas, J. A. P. (1988). Distribution of Calmodulin- and Cyclic AMP-Stimulated Protein Kinases in Synaptosomes. *Journal of Neurochemistry*, *51*(1), 57–68. https://doi.org/10.1111/j.1471-4159.1988.tb04835.x

Dunkley, P., Rostas, J. A. P., Heath, J., & Powis, D. A. (1987). *The preparation and use of synaptosomes for studying secretion of catecholamines*. (January).

Dunkley, Peter R., Jarvie, P. E., & Robinson, P. J. (2008). A rapid percoll gradient procedure for preparation of synaptosomes. *Nature Protocols*, *3*(11), 1718–1728. https://doi.org/10.1038/nprot.2008.171

Dunkley, Peter R., & Robinson, P. J. (1986). Depolarization-dependent protein phosphorylation in synaptosomes: Mechanisms and significance. *Progress in Brain Research*, *69*(C), 273–293. https://doi.org/10.1016/S0079-6123(08)61065-1

Dürr, K. L., Chen, L., Stein, R. A., De Zorzi, R., Folea, I. M., Walz, T., McHaourab, H. S., Gouaux, E. (2014). Structure and dynamics of AMPA receptor GluA2 in resting, pre-open, and desensitized states. *Cell*, *158*(4), 778–792. https://doi.org/10.1016/j.cell.2014.07.023

Eakle, K. A., Bernstein, M., & Emr, S. D. (1988). Characterization of a component of the yeast secretion machinery: identification of the SEC18 gene product. *Molecular and Cellular Biology*, *8*(10), 4098–4109. https://doi.org/10.1128/mcb.8.10.4098

Eltsov, M., MacLellan, K. M., Maeshima, K., Frangakis, A. S., & Dubochet, J. (2008). Analysis of cryo-electron microscopy images does not support the existence of 30-nm chromatin fibers in mitotic chromosomes in situ. *Proceedings of the National Academy of Sciences of the United States of America*, *105*(50), 19732–19737. https://doi.org/10.1073/pnas.0810057105

Engelhardt, H. (2018). Electron Microscopy. In F. Lottspeich & J. Engels (Eds.), *Bioanalytics* (pp. 485–517). Wiley.

Fasshauer, D., Sutton, R. B., Brunger, A. T., & Jahn, R. (1998). Conserved structural features of the synaptic fusion complex: SNARE proteins reclassified as Q-and R-SNAREs (membrane fusionneurotransmissionclostridial neurotoxins). *Neurobiology Communicated by Peter B. Moore*, *95*(December), 15781–15786.

Fenster, S. D., Chung, W. J., Zhai, R., Cases-Langhoff, C., Voss, B., Garner, A. M., Kaempf, U., Kindler, S., Gundelfinger, E. D., Garner, C. C. (2000). Piccolo, a presynaptic zinc finger protein structurally related to Bassoon. *Neuron*, *25*(1), 203–214. https://doi.org/10.1016/S0896-6273(00)80883-1

Fernández-Busnadiego, R., Asano, S., Oprisoreanu, A. M., Sakata, E., Doengi, M., Kochovski, Z., … Lučić, V. (2013). Cryo-electron tomography reveals a critical role of RIM1 α in synaptic vesicle tethering. *Journal of Cell Biology*, *201*(5), 725–740. https://doi.org/10.1083/jcb.201206063

Fernández-Busnadiego, R., & Lucic, V. (2012). The Cell at Molecular Resolution: Principles and Applications of Cryo-Electron Tomography. In *Cellular Imaging Techniques for Neuroscience and Beyond* (First Edit, pp. 141–184). https://doi.org/10.1016/B978-0-12-385872-6.00007-6

Fernández-Busnadiego, R., Zuber, B., Maurer, U. E., Cyrklaff, M., Baumeister, W., & Lučić, V. (2010). Quantitative analysis of the native presynaptic cytomatrix by cryoelectron tomography. *Journal of Cell Biology*, *188*(1), 145–156. https://doi.org/10.1083/jcb.200908082

Fernández-Chacón, R., Königstorfer, A., Gerber, S. H., García, J., Matos, M. F., Stevens, C. F., Brose, N., Rizo, J., Rosenmund, C., Südhof, T. C. (2001). Synaptotagmin I functions as a calcium regulator of release probability. *Nature*, *410*(6824), 41–49. https://doi.org/10.1038/35065004

Fernández, J. J., Li, S., & Crowther, R. A. (2006). CTF determination and correction in electron cryotomography. *Ultramicroscopy*, *106*(7), 587–596. https://doi.org/10.1016/j.ultramic.2006.02.004

Geppert, M., Goda, Y., Hammer, R. E., Li, C., Rosahl, T. W., Stevens, C. F., & Südhof, T. C. (1994). Synaptotagmin I: A major Ca2+ sensor for transmitter release at a central synapse. *Cell*, *79*(4), 717–727. https://doi.org/10.1016/0092-8674(94)90556-8

Glaeser, R. M., & Taylor, K. A. (1978). Radiation damage relative to transmission electron microscopy of biological specimens at low temperature: a review. *Journal of Microscopy*, *112*(1), 127–138. https://doi.org/10.1111/j.1365-2818.1978.tb01160.x

Grabrucker, A., Vaida, B., Bockmann, J., & Boeckers, T. M. (2009). Synaptogenesis of hippocampal neurons in primary cell culture. *Cell and Tissue Research*, *338*(3), 333–341. https://doi.org/10.1007/s00441-009-0881-z

Gray, E. G. (1963). Electron microscopy of presynaptic organelles of the spinal cord. *Journal of Anatomy*, *97*, 101–106. Retrieved from http://www.ncbi.nlm.nih.gov/pubmed/13949972%0Ahttp://www.pubmedcentral.nih.gov/articlerender.fcgi?artid=PMC1244260

Gray, E. G., & Whittaker, V. P. (1962). The isolation of nerve endings from brain: an electron-microscopic study of cell fragments derived by homogenization and centrifugation. *Journal of Anatomy*, *96*(June 1960), 79–88. Retrieved from http://www.ncbi.nlm.nih.gov/pubmed/13901297%0Ahttp://www.pubmedcentral.nih.gov/articlerender.fcgi?artid=PMC1244174

Greber-Platzera, S., Fleischmanna, C., Nussbaumerb, C., Cairnsc, N., & Lubeca, G. (2003).

Increased RNA levels of the 25 kDa synaptosomal associated protein in brain samples of adult patients with Down Syndrome. *Neuroscience Letters*, *336*(2), 77–80. https://doi.org/https://doi.org/10.1016/S0304-3940(02)01150-3

Greger, I. H., Watson, J. F., & Cull-Candy, S. G. (2017). Structural and Functional Architecture of AMPA-Type Glutamate Receptors and Their Auxiliary Proteins. *Neuron*, *94*(4), 713–730. https://doi.org/10.1016/j.neuron.2017.04.009

Grimm, R., Koster, A. J., Ziese, U., Typke, D., & Baumeister, W. (1996). Zero-loss energy filtering under low-dose conditions using a post-column energy filter. *Journal of Microscopy*, *183*(1), 60–68. https://doi.org/10.1046/j.1365-2818.1996.77441.x

Grimm, Rudo, Bärmann, M., Häckl, W., Typke, D., Sackmann, E., & Baumeister, W. (1997). Energy filtered electron tomography of ice-embedded actin and vesicles. *Biophysical Journal*, *72*(1), 482–489. https://doi.org/10.1016/S0006-3495(97)78689-2

Gustafsson, M. G. L. (2000). Surpassing the lateral resolution limit by a factor of two using structured illumination microscopy. *Journal of Microscopy*, *198*(2), 82–87. https://doi.org/10.1046/j.1365-2818.2000.00710.x

Hagen, W. J. H., Wan, W., & Briggs, J. A. G. (2017). Implementation of a cryo-electron tomography tilt-scheme optimized for high resolution subtomogram averaging. *Journal of Structural Biology*, *197*(2), 191–198. https://doi.org/10.1016/j.jsb.2016.06.007

Hanson, P. I., Roth, R., Morisaki, H., Jahn, R., & Heuser, J. E. (1997). Structure and conformational changes in NSF and its membrane receptor complexes visualized by quick-freeze/deep-etch electron microscopy. *Cell*, *90*(3), 523–535. https://doi.org/10.1016/S0092-8674(00)80512-7

Henderson, R. (2013). Avoiding the pitfalls of single particle cryo-electron microscopy: Einstein from noise. *Proceedings of the National Academy of Sciences*, *110*(45), 18037–18041. https://doi.org/10.1073/PNAS.1314449110

Herguedas, B., García-Nafría, J., Cais, O., Fernández-Leiro, R., Krieger, J., Ho, H., & Greger, I. H. (2016). Structure and organization of heteromeric AMPA-type glutamate receptors. *Science*, *352*(6285), 1–23. https://doi.org/10.1126/science.aad3873

Hirokawa, N., Sobue, K., Kanda, K., Harada, A., & Yorifuji, H. (1989). The cytoskeletal architecture of the presynaptic terminal and molecular structure of synapsin 1. *Journal of Cell Biology*, *108*(1), 111–126. https://doi.org/10.1083/jcb.108.1.111

Hoppe, W., & Hegerl, R. (1980). Three-Dimensional Structure Determination by Electron Microscopy (Nonperiodic Specimens). In P. W. Hawkes (Ed.), *Computer Processing of Electron Microscope Images* (pp. 127–185). https://doi.org/10.1007/978-3-642-81381-8_4

Huang, Y. Y., Zakharenko, S. S., Schoch, S., Kaeser, P. S., Janz, R., Südhof, T. C., Siegelbaum, S. A., Kandel, E. R. (2005). Genetic evidence for a protein-kinase-A-mediated presynaptic component in NMDA-receptor-dependent forms of long-term synaptic potentiation. *Proceedings of the National Academy of Sciences of the United States of America*, *102*(26),

9365–9370. https://doi.org/10.1073/pnas.0503777102

Hunter, J.D. Hunter, B. J. . (2011). Matplotlib : A 2D Graphics Environment. *Sci. Program. 90*, 90–95.

Imig, C., Min, S. W., Krinner, S., Arancillo, M., Rosenmund, C., Südhof, T. C., Rhee, J. S., Brose, N., Cooper, B. H. (2014). The Morphological and Molecular Nature of Synaptic Vesicle Priming at Presynaptic Active Zones. *Neuron*, *84*(2), 416–431. https://doi.org/10.1016/j.neuron.2014.10.009

Jahn, R., & Fasshauer, D. (2012). Molecular machines governing exocytosis of synaptic vesicles. *Nature*, *490*(7419), 201–207. https://doi.org/10.1038/nature11320

Jahn, R., & Scheller, R. H. (2006). SNAREs - Engines for membrane fusion. *Nature Reviews Molecular Cell Biology*, *7*(9), 631–643. https://doi.org/10.1038/nrm2002

Jeans, A. F., Oliver, P. L., Johnson, R., Capogna, M., Vikman, J., Molnár, Z., Babbs, A., Partridge, C. J., Salehi, A., Bengtsson, M., Eliasson, L., Rorsman, P., Davies, K. E. (2007). A dominant mutation in Snap25 causes impaired vesicle trafficking, sensorimotor gating, and ataxia in the blind-drunk mouse. *Proceedings of the National Academy of Sciences of the United States of America*, *104*(7), 2431–2436. https://doi.org/10.1073/pnas.0610222104

Jockusch, W. J., Speidel, D., Sigler, A., Sørensen, J. B., Varoqueaux, F., Rhee, J. S., & Brose, N. (2007). CAPS-1 and CAPS-2 Are Essential Synaptic Vesicle Priming Proteins. *Cell*, *131*(4), 796–808. https://doi.org/10.1016/j.cell.2007.11.002

Junge, H. J., Rhee, J. S., Jahn, O., Varoqueaux, F., Spiess, J., Waxham, M. N., Rosenmund, C., Brose, N. (2004). Calmodulin and Munc13 form a Ca2+ sensor/effector complex that controls short-term synaptic plasticity. *Cell*, *118*(3), 389–401. https://doi.org/10.1016/j.cell.2004.06.029

Kaeser, P. S., Deng, L., Wang, Y., Dulubova, I., Liu, X., Rizo, J., & Südhof, T. C. (2011). RIM proteins tether Ca2+ channels to presynaptic active zones via a direct PDZ-domain interaction. *Cell*, *144*(2), 282–295. https://doi.org/10.1016/j.cell.2010.12.029

Kaeser, P. S., Kwon, H.-B., Chiu, C. Q., Deng, L., Castillo, P. E., & Südhof, T. C. (2008). RIM1alpha and RIM1beta are synthesized from distinct promoters of the RIM1 gene to mediate differential but overlapping synaptic functions. *The Journal of Neuroscience : The Official Journal of the Society for Neuroscience*, *28*(50), 13435–13447. https://doi.org/10.1523/JNEUROSCI.3235-08.2008

Karakas, E., Simorowski, N., & Furukawa, H. (2011). Subunit arrangement and phenylethanolamine binding in GluN1/GluN2B NMDA receptors. *Nature*, *475*(7355), 249–253. https://doi.org/10.1038/nature10180

Karuppasamy, M., Karimi Nejadasl, F., Vulovic, M., Koster, A. J., & Ravelli, R. B. G. (2011). Radiation damage in single-particle cryo-electron microscopy: Effects of dose and dose rate. *Journal of Synchrotron Radiation*, *18*(3), 398–412. https://doi.org/10.1107/S090904951100820X

Kirkland, A. I., Chang, S. L.-Y., & Hutchison, J. L. (2007). Atomic Resolution Transmission Electron Microscopy. In P. W. Hawkes & J. C. H. Spence (Eds.), *Science of Microscopy* (pp. 3–64). Springer Science+Business Media, LLC.

Klar, T. A., & Hell, S. W. (1999). Subdiffraction resolution in far-field fluorescence microscopy. *Optics Letters*, *24*(14), 954–956. https://doi.org/10.1364/ol.24.000954

Koch, H., Hofmann, K., & Brose, N. (2000). Definition of Munc13-homology-domains and characterization of a novel ubiquitously expressed Munc13 isoform. *Biochemical Journal*, *349*(1), 247–253. https://doi.org/10.1042/0264-6021:3490247

Kochovski, Z. (2014). Image analysis of molecular complexes present in cryo-tomograms of neuronal synapses. PhD dissertation, *Technische Universität München*, http://d-nb.info/1054753075

Koning, R. I., Koster, A. J., & Sharp, T. H. (2018). Advances in cryo-electron tomography for biology and medicine. *Annals of Anatomy*, *217*, 82–96. https://doi.org/10.1016/j.aanat.2018.02.004

Koster, A. J., Chen, H., Sedat, J. W., & Agard, D. A. (1992). Automated microscopy for electron tomography. *Ultramicroscopy*, *46*(1–4), 207–227. https://doi.org/10.1016/0304-3991(92)90016-D

Koster, Abraham J., Grimm, R., Typke, D., Hegerl, R., Stoschek, A., Walz, J., & Baumeister, W. (1997). Perspectives of molecular and cellular electron tomography. *Journal of Structural Biology*, *120*(3), 276–308. https://doi.org/10.1006/jsbi.1997.3933

Kremer, J. R., Mastronarde, D. N., & McIntosh, J. R. (1996). Computer visualization of three-dimensional image data using IMOD. *Journal of Structural Biology*, *116*(1), 71–76. https://doi.org/10.1006/jsbi.1996.0013

Krivanek, O. L., Friedman, S. L., Gubbens, A. J., & Kraus, B. (1995). An imaging filter for biological applications. *Ultramicroscopy*, *59*(1–4), 267–282. https://doi.org/10.1016/0304-3991(95)00034-X

Krivanek, O. L., & Mooney, P. E. (1993). Applications of slow-scan CCD cameras in transmission electron microscopy. *Ultramicroscopy*, *49*(1–4), 95–108. https://doi.org/10.1016/0304-3991(93)90216-K

Lai, Y., Choi, U. B., Leitz, J., Rhee, H. J., Lee, C., Altas, B., Zhao, M., Pfuetzner, R. A., Wang, A. L., Brose, N., Rhee, J. S., Brunger, A. T. (2017). Molecular Mechanisms of Synaptic Vesicle Priming by Munc13 and Munc18. *Neuron*, *95*(3), 591-607.e10. https://doi.org/10.1016/j.neuron.2017.07.004

Laugks, U. (2018). Structural analysis of short-term release faciliation in synaptosomes and synapses. PhD dissertation, *Technische Universität München*, http://d-nb.info/1200547527

Li, X., Mooney, P., Zheng, S., Booth, C. R., Braunfeld, M. B., Gubbens, S., Agard, D. A., Cheng, Y. (2013). Electron counting and beam-induced motion correction enable near-atomic-

resolution single-particle cryo-EM. *Nature Methods*, *10*(6), 584–590. https://doi.org/10.1038/nmeth.2472

Limbach, C., Laue, M. M., Wang, X., Hu, B., Thiede, N., Hultqvist, G., & Kilimann, M. W. (2011). Molecular in situ topology of Aczonin/Piccolo and associated proteins at the mammalian neurotransmitter release site. *Proceedings of the National Academy of Sciences of the United States of America*, *108*(31). https://doi.org/10.1073/pnas.1101707108

Lipstein, N., Schaks, S., Dimova, K., Kalkhof, S., Ihling, C., Kolbel, K., Ashery, U., Rhee, J., Brose, N., Sinz, A., Jahn, O. (2012). Nonconserved Ca2+/Calmodulin Binding Sites in Munc13s Differentially Control Synaptic Short-Term Plasticity. *Molecular and Cellular Biology*, *32*(22), 4628–4641. https://doi.org/10.1128/mcb.00933-12

Liu, X., Seven, A. B., Camacho, M., Esser, V., Xu, J., Trimbuch, T., Quade, B., Su, L., Ma, C., Rosenmund, C., Rizo, J. (2016). Functional synergy between the Munc13 C-terminal C1 and C2 domains. *ELife*, *5*(MAY2016), 1–27. https://doi.org/10.7554/eLife.13696

Lučić, V., Fernández-Busnadiego, R., Laugks, U., & Baumeister, W. (2016). Hierarchical detection and analysis of macromolecular complexes in cryo-electron tomograms using Pyto software. *Journal of Structural Biology*, *196*(3), 503–514. https://doi.org/10.1016/j.jsb.2016.10.004

Lučić, V., Förster, F., & Baumeister, W. (2005). STRUCTURAL STUDIES BY ELECTRON TOMOGRAPHY: From Cells to Molecules. *Annual Review of Biochemistry*, *74*(1), 833–865. https://doi.org/10.1146/annurev.biochem.73.011303.074112

Lučić, V., Rigort, A., & Baumeister, W. (2013). Cryo-electron tomography: The challenge of doing structural biology in situ. *Journal of Cell Biology*, *202*(3), 407–419. https://doi.org/10.1083/jcb.201304193

Ma, C., Liging, S., Seven, A. B., Xu, Y., & Rizo, J. (2013). Reconstitution of the vital functions of Munc18 and Munc13 in neurotransmitter release. *Science*, *339*(January), 421–426.

Man, K. N. M., Imig, C., Walter, A. M., Pinheiro, P. S., Stevens, D. R., Rettig, J., Sørensen, J. B., Cooper, B. H., Brose, N., Wojcik, S. M. (2015). Identification of a Munc13-sensitive step in chromaffin cell large dense-core vesicle exocytosis. *ELife*, *4*(NOVEMBER2015), 1–28. https://doi.org/10.7554/elife.10635

Marsh, B. J., Mastronarde, D. N., Buttle, K. F., Howell, K. E., & Mcintosh, J. R. (2001). Organellar relationships in the Golgi region of the pancreatic beta cell line, HIT-T15, visualized by high resolution electron tomography. *Proc Natl Acad Sci USA*, *98*(5), 2399–2406. https://doi.org/10.1073/pnas.051631998.

Martinez-Sanchez, A., Kochovski, Z., Laugks, U., Meyer zum Alten Borgloh, J., Chakraborty, S., Pfeffer, S., Baumeister, W., Lučić, V. (2020). Template-free detection and classification of membrane-bound complexes in cryo-electron tomograms. *Nature Methods*, *17*(February). https://doi.org/10.1038/s41592-019-0675-5

Martinez-Sanchez, A., Laugks, U., Kochovski, Z., Papantoniou, C., Zinzula, L., Baumeister, W., &

Lucic, V. (2020). Trans-synaptic assemblies link synaptic vesicles and neuroreceptors. *BioRxiv*. https://doi.org/10.1101/2020.07.17.208173

Maruyama, I. N., & Brenner, S. (1991). A phorbol ester/diacylglycerol-binding protein encoded by the unc-13 gene of Caenorhabditis elegans. *Proceedings of the National Academy of Sciences of the United States of America*, *88*(13), 5729–5733. https://doi.org/10.1073/pnas.88.13.5729

Mastronarde, D. N. (2005). Automated electron microscope tomography using robust prediction of specimen movements. *Journal of Structural Biology*, *152*(1), 36–51. https://doi.org/10.1016/j.jsb.2005.07.007

Maus, L., Lee, C. K., Altas, B., Sertel, S. M., Weyand, K., Rizzoli, S. O., Rhee, J. S., Brose, N., Imig, C., Cooper, B. H. (2020). Ultrastructural Correlates of Presynaptic Functional Heterogeneity in Hippocampal Synapses. *Cell Reports*, *30*(11), 3632-3643.e8. https://doi.org/10.1016/j.celrep.2020.02.083

Mayer, A., Wickner, W., & Haas, A. (1996). Sec18p (NSF)-driven release of Sec17p (α-SNAP) can precede docking and fusion of yeast vacuoles. *Cell*, *85*(1), 83–94. https://doi.org/10.1016/S0092-8674(00)81084-3

McMullan, G., Faruqi, A. R., Clare, D., & Henderson, R. (2014). Comparison of optimal performance at 300keV of three direct electron detectors for use in low dose electron microscopy. *Ultramicroscopy*, *147*, 156–163. https://doi.org/10.1016/j.ultramic.2014.08.002

Medalia, O., Weber, I., Frangakis, A. S., Nicastro, D., Gerisch, G., & Baumeister, W. (2002). Macromolecular architecture in eukaryotic cells visualized by cryoelectron tomography. *Science*, *298*(5596), 1209–1213. https://doi.org/10.1126/science.1076184

Meents, A., Gutmann, S., Wagner, A., & Schulze-Briese, C. (2010). Origin and temperature dependence of radiation damage in biological samples at cryogenic temperatures. *Proceedings of the National Academy of Sciences of the United States of America*, *107*(3), 1094–1099. https://doi.org/10.1073/pnas.0905481107

Misura, K. M. S., Scheller, R. H., & Weis, W. I. (2000). Three-dimensional structure of the neuronal-Sec1-syntaxin 1a complex. *Nature*, *404*(6776), 355–362. https://doi.org/10.1038/35006120

Mittelstaedt, T., Alvaréz-Baron, E., & Schoch, S. (2010). RIM proteins and their role in synapse function. *Biological Chemistry*, *391*(6), 599–606. https://doi.org/10.1515/bc.2010.064

Morgan, I. G. (1976). Synaptosomes and cell separation. *Neuroscience*, *1*(3), 159–165. https://doi.org/10.1016/0306-4522(76)90072-5

Mori, N., Oikawa, T., Katoh, T., Miyahara, J., & Harada, Y. (1988). Application of the “imaging plate” to TEM image recording. *Ultramicroscopy*, *25*(3), 195–201. https://doi.org/10.1016/0304-3991(88)90014-9

Müller, M., Meister, N., & Moor, H. (1980). Freezing in a propane jet and its application in freeze-fracturing. *Mikroskopie*, *36*(5–6), 129–140.

Nicoll, R. A. (2017). A Brief History of Long-Term Potentiation. *Neuron*, *93*(2), 281–290. https://doi.org/10.1016/j.neuron.2016.12.015

Novick, P., Field, C., & Schekman, R. (1980). Identification of 23 complementation groups required for post-translational events in the yeast secretory pathway. *Cell*, *21*(1), 205–215. https://doi.org/https://doi.org/10.1016/0092-8674(80)90128-2

Oorschot, D. E. (1989). Effect of fluorodeoxyuridine on neurons and non-neuronal cells in cerebral explants. *Experimental Brain Research*, *78*(1), 132–138. https://doi.org/10.1007/bf00230692

Parfitt, B. Y. K. D., & Madison, D. V. (1993). Phorbol esters enhance synaptic transmission by a presynaptic, calcium-dependent mechanism in rat hippocampus. *J Physiol*, (471), 245–268.

Patterson, G., Davidson, M., Manley, S., & Lippincott-Schwartz, J. (2010). Superresolution Imaging using Single-Molecule Localization. *Annual Review of Physical Chemistry*, *61*(1), 345–367. https://doi.org/10.1146/annurev.physchem.012809.103444

Phillips, G. R., Huang, J. K., Wang, Y., Tanaka, H., Shapiro, L., Zhang, W., Shan, W. S., Arndt, K., Frank, M., Gordon, R. E., Gawinowicz, M. A., Zhao, Y., Colman, D. R. (2001). The presynaptic particle web: Ultrastructure, composition, dissolution, and reconstitution. *Neuron*, *32*(1), 63–77. https://doi.org/10.1016/S0896-6273(01)00450-0

Pitsch, J., Opitz, T., Borm, V., Woitecki, A., Staniek, M., Beck, H., Becker, A. J., Schoch, S. (2012). The presynaptic active zone protein rim α controls epileptogenesis following status epilepticus. *Journal of Neuroscience*, *32*(36), 12384–12395. https://doi.org/10.1523/JNEUROSCI.0223-12.2012

Poirier, M. A., Xiao, W., Macosko, J. C., Chan, C., Shin, Y.-K., & Bennett, M. K. (1998). The synaptic SNARE complex is a parallel four- stranded helical bundle. *Nat Struct Biol*, *5*(9), 765–769. https://doi.org/10.1038/1799

Powell, C. M., Schoch, S., Monteggia, L., Barrot, M., Matos, M. F., Feldmann, N., Südhof, T. C., Nestler, E. J. (2004). The presynaptic active zone protein RIM1α is critical for normal learning and memory. *Neuron*. https://doi.org/10.1016/S0896-6273(04)00146-1

Reimer, L., & Kohl, H. (2008). *Transmission Electron Microscopy* (5th ed.). Springer-Verlag New York.

Rizo, J., & Südhof, T. C. (2012). The Membrane Fusion Enigma: SNAREs, Sec1/Munc18 Proteins, and Their Accomplices—Guilty as Charged? In *Annual Review of Cell and Developmental Biology* (Vol. 28). https://doi.org/10.1146/annurev-cellbio-101011-155818

Ruskin, R. S., Yu, Z., & Grigorieff, N. (2013). Quantitative characterization of electron detectors for transmission electron microscopy. *Journal of Structural Biology*, *184*(3), 385–393. https://doi.org/10.1016/j.jsb.2013.10.016

Sauer, B. (1987). Functional expression of the cre-lox site-specific recombination system in the yeast Saccharomyces cerevisiae. *Molecular and Cellular Biology*, *7*(6), 2087–2096. https://doi.org/10.1128/mcb.7.6.2087

Saxton, W. O., Baumeister, W., & Hahn, M. (1984). Three-dimensional reconstruction of imperfect two-dimensional crystals. *Ultramicroscopy*, *13*(1–2), 57–70.

Schoch, S., Deák, F., Königstorfer, A., Mozhayeva, M., Sara, Y., Südhof, T. C., & Kavalali, E. T. (2001). SNARE function analyzed in synaptobrevin/VAMP knockout mice. *Science*, *294*(5544), 1117–1122. https://doi.org/10.1126/science.1064335

Schrod, N., Vanhecke, D., Laugks, U., Stein, V., Fukuda, Y., Schaffer, M., Baumeister, W., Lucic, V. (2018). Pleomorphic linkers as ubiquitous structural organizers of vesicles in axons. *PLoS ONE*, *13*(6), 1–24. https://doi.org/10.1371/journal.pone.0197886

Shi, L., Shen, Q. T., Kiel, A., Wang, J., Wang, H. W., Melia, T. J., Rothman, J. E., Pincet, F. (2012). SNARE proteins: One to fuse and three to keep the nascent fusion pore open. *Science*, *335*(6074), 1355–1359. https://doi.org/10.1126/science.1214984

Siksou, L., Rostaing, P., Lechaire, J. P., Boudier, T., Ohtsuka, T., Fejtová, A., Kao, H. T., Greengard, P., Gundelfinger, E. D., Triller, A., Marty, S. (2007). Three-dimensional architecture of presynaptic terminal cytomatrix. *Journal of Neuroscience*, *27*(26), 6868–6877. https://doi.org/10.1523/JNEUROSCI.1773-07.2007

Siksou, L., Varoqueaux, F., Pascual, O., Triller, A., Brose, N., & Marty, S. (2009). A common molecular basis for membrane docking and functional priming of synaptic vesicles. *European Journal of Neuroscience*, *30*(1), 49–56. https://doi.org/10.1111/j.1460-9568.2009.06811.x

Sinha, R., Ahmed, S., Jahn, R., & Klingauf, J. (2011). Two synaptobrevin molecules are sufficient for vesicle fusion in central nervous system synapses. *Proceedings of the National Academy of Sciences of the United States of America*, *108*(34), 14318–14323. https://doi.org/10.1073/pnas.1101818108

Sobolevsky, A. I., Rosconi, M. P., & Gouaux, E. (2009). X-ray structure, symmetry and mechanism of an AMPA-subtype glutamate receptor. *Nature*, *462*(7274), 745–756. https://doi.org/10.1038/nature08624

Söllner, T. H., Bennett, M. K., Whiteheart, S. W., Scheller, R. H., & Rothman, J. E. (1993). A protein assembly-disassembly pathway in vitro that may correspond to sequential steps of synaptic vesicle docking, activation, and fusion. *Cell*, *75*(3), 409–418. Retrieved from http://eutils.ncbi.nlm.nih.gov/entrez/eutils/elink.fcgi?dbfrom=pubmed&id=8221884&retmode=ref&cmd=prlinks%0Afile:///Files/91/918F253E-D90A-4BB2-A150-F3C0C4CFF846.pdf

Song, Y., Ailenberg, M., & Silverman, M. (1998). Cloning of a novel gene in the human kidney homologous to rat munc13s: Its potential role in diabetic nephropathy. *Kidney International*, *53*(6), 1689–1695. https://doi.org/10.1046/j.1523-1755.1998.00942.x

Sousbie, T. (2011). The persistent cosmic web and its filamentary structure - I. Theory and

implementation. *Monthly Notices of the Royal Astronomical Society*, *414*(1), 350–383. https://doi.org/10.1111/j.1365-2966.2011.18394.x

Stevens, D. R., Wu, Z. X., Matti, U., Junge, H. J., Schirra, C., Becherer, U., Wojcik, S. M., Brose, N., Rettig, J. (2005). Identification of the minimal protein domain required for priming activity of munc13-1. *Current Biology*, *15*(24), 2243–2248. https://doi.org/10.1016/j.cub.2005.10.055

Südhof, T. (2012). The Presynaptic Active Zone. *Neuron*, *75*(1), 11–25. https://doi.org/10.1016/j.neuron.2012.06.012.The

Südhof, T. C., & Rizo, J. (2011). Synaptic Vesicle Exocytosis. *Cold Spring Harb Perspect Biol.*, *3*(12). https://doi.org/10.1101/cshperspect.a005637

Südhof, T. C., & Rothman, J. E. (2009). Membrane fusion: Grappling with SNARE and SM proteins. *Science*, *323*(5913), 474–477. https://doi.org/10.1126/science.1161748

Sutton, R. B., Fasshauer, D., Jahn, R., & Brunger, A. T. (1998). Crystal structure of a SNARE complex involved in synaptic exocytosis at 2.4 Å resolution. *Nature*, *395*(6700), 347–353. https://doi.org/10.1038/26412

Tang, A. H., Chen, H., Li, T. P., Metzbower, S. R., MacGillavry, H. D., & Blanpied, T. A. (2016). A trans-synaptic nanocolumn aligns neurotransmitter release to receptors. *Nature*, *536*(7615), 210–214. https://doi.org/10.1038/nature19058

Tao, C. L., Liu, Y. T., Sun, R., Zhang, B., Qi, L., Shivakoti, S., Tian, C. L., Zhang, P., Lau, P. M., Hong Zhou, Z., Bi, G. Q. (2018). Differentiation and characterization of excitatory and inhibitory synapses by cryo-electron tomography and correlative microscopy. *Journal of Neuroscience*, *38*(6), 1493–1510. https://doi.org/10.1523/JNEUROSCI.1548-17.2017

Taylor, K. A., & Glaeser, R. M. (1976). Electron Microscopy of Frozen Hydrated Biological Specimens at the level of atomic resolution is a major. *Journal of Ultrastructure Research*, *55*, 448–456.

Thompson, P. M., Sower, A. C., & Perrone-Bizzozero, N. I. (1998). Altered levels of the synaptosomal associated protein SNAP-25 in schizophrenia. *Biological Psychiatry*, *43*(4), 239–243. https://doi.org/10.1016/S0006-3223(97)00204-7

Tom Dieck, S., Sanmartí-Vila, L., Langnaese, K., Richter, K., Kindler, S., Soyke, A., Wex, H., Smalla, K. H., Kämpf, U., Fränzer, J. T., Stumm, M., Garner, C. C., Gundelfinger, E. D. (1998). Bassoon, a novel zinc-finger CAG/glutamine-repeat protein selectively localized at the active zone of presynaptic nerve terminals. *Journal of Cell Biology*, *142*(2), 499–509. https://doi.org/10.1083/jcb.142.2.499

Varoqueaux, F., Sigler, A., Rhee, J. S., Brose, N., Enk, C., Reim, K., & Rosenmund, C. (2002). Total arrest of spontaneous and evoked synaptic transmission but normal synaptogenesis in the absence of Munc13-mediated vesicle priming. *Proceedings of the National Academy of Sciences of the United States of America*, *99*(13), 9037–9042. https://doi.org/10.1073/pnas.122623799

Wan, W., Kolesnikova, L., Clarke, M., Koehler, A., Noda, T., Becker, S., & Briggs, J. A. G. (2017). Structure and assembly of the Ebola virus nucleocapsid. *Nature*, *551*(7680), 394–397. https://doi.org/10.1038/nature24490

Wang, X., Kibschull, M., Laue, M. M., Lichte, B., Petrasch-Parwez, E., & Kilimann, M. W. (1999). Aczonin, a 550-kD putative scaffolding protein of presynaptic active zones, shares homology regions with Rim and Bassoon and binds profilin. *Journal of Cell Biology*, *147*(1), 151–162. https://doi.org/10.1083/jcb.147.1.151

Wang, Y., Mukherjee, K., Castillo, P. E., Jo, T., Schoch, S., Malenka, R. C., Schmitz, F., Südhof, T. C., Geppert, M. (2002). RIM1alpha forms a protein scaffold for regulating neurotransmitter release at the active zone. *Nature*, *415*(6869), 321–326. Retrieved from http://eutils.ncbi.nlm.nih.gov/entrez/eutils/elink.fcgi?dbfrom=pubmed&id=11797009&retmode=ref&cmd=prlinks%0Afile:///Files/6C/6C26FE26-4B09-4E37-87C8-CE89607ECDC4.pdf%0Apapers3://publication/doi/10.1038/415321a

Wang, Y., Okamoto, M., Schmitz, F., Hofmann, K., & Südhof, T. C. (1997). Rim is a putative rab3 effector in regulating synaptic-vesicle fusion. *Nature*, *388*(6642), 593–598. https://doi.org/10.1038/41580

Wang, Y., & Südhof, T. C. (2003). Genomic definition of RIM proteins: evolutionary amplification of a family of synaptic regulatory proteins. *Genomics*, *81*(2), 126–137. https://doi.org/10.1016/s0888-7543(02)00024-1

Wang, Y., Sugita, S., & Südhof, T. C. (2000). The RIM/NIM family of neuronal C2 domain proteins: Interactions with Rab3 and a new class of Src homology 3 domain proteins. *Journal of Biological Chemistry*, *275*(26), 20033–20044. https://doi.org/10.1074/jbc.M909008199

Washbourne, P., Thompson, P. M., Carta, M., Costa, E. T., Mathews, J. R., Lopez-Benditó, G., Molnár, Z., Becher, M. W., Valenzuela, C. F., Partridge, L. D., Wilson, M. C. (2002). Genetic ablation of the t-SNARE SNAP-25 distinguishes mechanisms of neuroexocytosis. *Nature Neuroscience*, *5*(1), 19–26. https://doi.org/10.1038/nn783

Weber, T., Zemelman, B. V., McNew, J. A., Westermann, B., Gmachl, M., Parlati, F., Söllner, T. H., Rothman, J. E. (1998). SNAREpins: Minimal machinery for membrane fusion. *Cell*, *92*(6), 759–772. https://doi.org/10.1016/S0092-8674(00)81404-X

Weimer, R. M., Gracheva, E. O., Meyrignac, O., Miller, K. G., Richmond, J. E., & Bessereau, J. L. (2006). UNC-13 and UNC-10/Rim localize synaptic vesicles to specific membrane domains. *Journal of Neuroscience*, *26*(31), 8040–8047. https://doi.org/10.1523/JNEUROSCI.2350-06.2006

White, K. I., Zhao, M., Choi, U. B., Pfuetzner, R. A., & Brunger, A. T. (2018). Structural principles of SNARE complex recognition by the AAA+ protein NSF. *ELife*, *7*, 1–26. https://doi.org/10.7554/eLife.38888

Whittaker, V. P. (1993). Thirty years of synaptosome research. *Journal of Neurocytology*, *22*(9),

735–742. https://doi.org/10.1007/BF01181319

Whittaker, V. P., Michaelson, I. A., & Kirkland, R. J. A. (1964). The separation of synaptic vesicles from nerve-ending particles ('synaptosomes'). *Biochemical Journal*, *90*(2), 293–303. https://doi.org/10.1042/bj0900293

Williams, D. B., & Carter, C. B. (2009). The Transmission Electron Microscope. In *Transmission Electron Microscopy* (pp. 3–22). https://doi.org/https://doi.org/10.1007/978-0-387-76501-3

Xue, R., Ruhl, D. A., Briguglio, J. S., Figueroa, A. G., Pearce, R. A., & Chapman, E. R. (2018). Doc2-mediated superpriming supports synaptic augmentation. *Proceedings of the National Academy of Sciences of the United States of America*, *115*(24), E5605–E5613. https://doi.org/10.1073/pnas.1802104115

Yang, X., Wang, S., Sheng, Y., Zhang, M., Zou, W., Wu, L., Kang, L., Rizo, J., Zhang, R., Xu, T., Ma, C. (2015). Syntaxin opening by the MUN domain underlies the function of Munc13 in synaptic-vesicle priming. *Nature Structural and Molecular Biology*, *22*(7), 547–554. https://doi.org/10.1038/nsmb.3038

Yelshanskaya, M. V., Saotome, K., Singh, A. K., & Sobolevsky, A. I. (2016). Probing Intersubunit Interfaces in AMPA-subtype Ionotropic Glutamate Receptors. *Scientific Reports*, *6*, 1–8. https://doi.org/10.1038/srep19082

Yonekura, K., Braunfeld, M. B., Maki-Yonekura, S., & Agard, D. A. (2006). Electron energy filtering significantly improves amplitude contrast of frozen-hydrated protein at 300 kV. *Journal of Structural Biology*, *156*(3), 524–536. https://doi.org/10.1016/j.jsb.2006.07.016

Zampighi, G. A., Zampighi, L. M., Fain, N., Lanzavecchia, S., Simon, S. A., & Wright, E. M. (2006). Conical electron tomography of a chemical synapse: Vesicles docked to the active zone are hemi-fused. *Biophysical Journal*, *91*(8), 2910–2918. https://doi.org/10.1529/biophysj.106.084814

Zandbergen, H. W. (1997). Electron Microscopy Techniques. In D. L. Dorset, S. Hovmöller, & X. Zou (Eds.), *Electron Crystallography* (pp. 41–54). https://doi.org/10.1007/978-94-015-8971-0_4

Zheng, X., & Bobich, J. A. (1998). A sequential view of neurotransmitter release. *Brain Research Bulletin*, *47*(2), 117–128. https://doi.org/10.1016/S0361-9230(98)00040-9

Zhou, Q., Lai, Y., Bacaj, T., Zhao, M., Lyubimov, A. Y., Uervirojnangkoorn, M., Zeldin, Oliver B., Brewster, A. S., Sauter, N. K., Cohen, A. E., Soltis, S. M., Alonso-Mori, R., Chollet, M., Lemke, H. T., Pfuetzner, R. A., Choi, U. B., Weis, W. I., Diao, J., Südhof, T. C., Brunger, A. T. (2015). Architecture of the synaptotagmin-SNARE machinery for neuronal exocytosis. *Nature*, *525*(7567), 62–67. https://doi.org/10.1038/nature14975

Zhou, Q., Zhou, P., Wang, A. L., Wu, D., Zhao, M., Südhof, T. C., & Brunger, A. T. (2017). The primed SNARE-complexin-synaptotagmin complex for neuronal exocytosis. *Nature*, *548*(7668), 420–425. https://doi.org/10.1038/nature23484

Zuber, B., & Lučić, V. (2019). Molecular architecture of the presynaptic terminal. *Current Opinion in Structural Biology*, *54*, 129–138. https://doi.org/10.1016/j.sbi.2019.01.008

8. Acknowledgements

The present thesis has been written during the COVID-19 pandemic. As we are currently going through the second wave of the pandemic, it becomes more and more apparent that a disturbingly increased number of people do not trust the guidelines of the scientific community, but rather turn their heads towards conspiracy theories and pseudo-scientific data. Although the spread of those false information has been facilitated a lot by the widespread use of social media, scientists are also to be blamed for this situation. We need to reach out to people more often and find the time and the patience to explain what we are doing and why we are doing it, no matter how complicated it is. I really hope that, first of all, the pandemic situation will be handled as soon as possible, and, most importantly for the future, people will regain their faith in science!

When I came for an interview to this department, Prof. Baumeuster asked me why I wanted to become a structural biologist. Back then, I had no idea if I even wanted to be one. After five years in this department, even though I still consider myself a neuroscientist, I definitely know that, doing this PhD, I received some invaluable scientific knowledge, learned new and fascinating techniques and that the combination of structural biology with neuroscience will help me pursue my dream of excelling in the field of Neurobiology.

It is Prof. Baumeister that I would like to thank, first and foremost, for giving me the opportunity to work in this amazing department and use its cutting-edge technology.

Secondly, I would like to thank Dr. Vladan Lučić for hiring me and believing in me at a time that I had stopped believing in myself. He has been an amazing supervisor! His door was always open and he replied to my emails almost immediately (even late at night). His relaxing behavior and confidence in me, as well as his patience made my PhD experience a really amazing one.

All members of the group Vladan were amazing. Antonio was very helpful with all the computational issues that I encountered. Uli has been my great teacher and a good friend. Almost everything I learned during my PhD years, I learned from her. I would like to thank her for being there for me even after she has left the Department. Cristina was a member of group Vladan for

only a few months, but she has been very helpful and I'm happy to see her thrive at her work as a PhD student.

Prof. Jürgen Plitzko has made sure that we always have the latest and most state-of-the-art microscopes and, along with Günter Pfeiffer, ensured that they were working flawlessly and that we would have whatever we need to make the most out of these very expensive and very delicate instruments. Whenever there was a technical computer issue, Inga Wolf and Florian Beck were always there to provide assistance to the problems. Our secretaries, Birgit Book, Eva Sartorius and formerly Nathalie Leclerq were extremely helpful with any administrative and bureaucratic issue that would come up.

The people from the workshop were willing to help with any technical problem that would appear. I want to thank especially Herr Gatz, and later Johannes, for all their aid in bike fixing, and the former workshop member Tim, for helping me organize my trips to our collaborators and for the nice talks we had about geeky stuff.

The work of this thesis would not be possible without the help of our collaborators. From Uniklinikum Bonn, I would like to thank Prof. Susanne Schoch-McGovern and Julia Betzin. Also, from the Cesar Institute in Bonn, I would like to thank Christoph Klatt. We have collaborated for the RIM project. From MPI of Experimental Medicine, I would like to thank Prof. Nils Brose as well as Dr. Cordelia Imig and Dr. Benjamin Cooper for our collaboration for the Munc13 and SNAP25 projects.

I have come to consider the whole Baumeister department as my second family. I would like to thank every member (current and former) for all the amazing time we had over lunch, for the beer sessions every Friday, even via Zoom during the lockdown, the BBQs and the great parties. I will always remember fondly my time here and it is because of you, beautiful people!

Thankfully, my time as a PhD student was not only filled with science. With the Pokémon group, we had lots of walks and many raids in our cause to be the very best. The volleyball group gave me the chance to exercise and have fun. Although we didn't manage to win a Summerfest tournament, there were definitely a lot of exciting games and I got to know some awesome people!

One of them has become a central part of my life for the last year. I would like to thank my girlfriend Martina for her love and support and for making my life brighter! I would not be able to come through the quarantine time if it wasn't for her. Grazie amore, ti amo tanto!

Last, but not least, I want to thank my family and friends from Greece. I wouldn't be where I am now, if I didn't know that they are always there for me. Special thanks to my parents, George and Maria, and my sister Natasa for believing in me and supporting me in any way! Σας αγαπώ και σας ευχαριστώ για όλα!